

# Impact of initial mass function on the chemical evolution of high-redshift galaxies

Boyuan Liu<sup>1,\*</sup>, Michela Mapelli<sup>1,2,3,4</sup>, Volker Bromm<sup>5,6</sup>, Ralf S. Klessen<sup>1,2,7,8</sup>, Lumen Boco<sup>1</sup>,  
Tilman Hartwig<sup>9</sup>, Simon C. O. Glover<sup>1</sup>, Veronika Lipatova<sup>1</sup>, Guglielmo Costa<sup>4,10</sup>,  
Marco Dall’Amico<sup>1,3,4</sup>, Giuliano Iorio<sup>11</sup>, Kendall Shepherd<sup>10,12</sup>, and Alessandro Bressan<sup>12</sup>

- <sup>1</sup> Universität Heidelberg, Zentrum für Astronomie, Institut für Theoretische Astrophysik, Albert Ueberle Str. 2, D-69120 Heidelberg, Germany  
<sup>2</sup> Universität Heidelberg, Interdisziplinäres Zentrum für Wissenschaftliches Rechnen, D-69120 Heidelberg, Germany  
<sup>3</sup> INFN-Padova, Via Marzolo 8, I-35131 Padova, Italy  
<sup>4</sup> Dipartimento di Fisica e Astronomia Galileo Galilei, Università di Padova, Vicolo dell’Osservatorio 3, I-35122 Padova, Italy  
<sup>5</sup> Department of Astronomy, University of Texas, Austin, TX 78712, USA  
<sup>6</sup> Weinberg Institute for Theoretical Physics, University of Texas, Austin, TX 78712, USA  
<sup>7</sup> Harvard-Smithsonian Center for Astrophysics, 60 Garden Street, Cambridge, MA 02138, USA  
<sup>8</sup> Elizabeth S. and Richard M. Cashin Fellow at the Radcliffe Institute for Advanced Studies at Harvard University, 10 Garden Street, Cambridge, MA 02138, USA  
<sup>9</sup> Application Lab for AI and Big Data, German Environment Agency, Alte Messe 6, 04103 Leipzig, Germany  
<sup>10</sup> INAF - Osservatorio Astronomico di Padova, Vicolo dell’Osservatorio 5, Padova, Italy  
<sup>11</sup> Departament de Física Quàntica i Astrofísica, Institut de Ciències del Cosmos, Universitat de Barcelona, Martí i Franquès 1, E-08028 Barcelona, Spain  
<sup>12</sup> SISSA, via Bonomea 365, I-34136 Trieste, Italy

Received xxx; accepted xxx

## ABSTRACT

**Context.** Star formation and metal enrichment in galaxies are regulated by supernova (SN) explosions and metal yields from massive stars, which are sensitive to the high-mass end of the initial mass function (IMF). Recent JWST observations found evidence for an invariant relation between stellar mass, metallicity, and star formation rate up to  $z \sim 8$  and its breakdown at higher redshifts. It is crucial to understand the underlying physics, especially the role played by the IMF.

**Aims.** We explore the impact of IMF on the chemical evolution of high-redshift galaxies and the interplay between IMF and galactic outflow parameters. The ultimate goal is to constrain the high-mass end of the IMF by the cosmic star formation history and stellar mass-metallicity-star formation rate relation (MZSFR) inferred from observations at  $z \sim 4 - 10$ .

**Methods.** Using the semi-analytical galaxy evolution code A-SLOTH, we follow galactic baryon cycles along merger trees built from a high-resolution cosmological simulation. Stellar feedback is modeled with up-to-date stellar evolution tracks covering the full metallicity range ( $Z \sim 10^{-11} - 0.03$ ) and a broad stellar mass range ( $m_{\star} \sim 2 - 600 M_{\odot}$ ), including the metal yields from stellar winds, core-collapse SNe, (pulsational) pair-instability SNe, and Type Ia SNe.

**Results.** Assuming a Kroupa-like shape of the IMF with a varying upper mass limit  $m_{\max}$ , we find that  $m_{\max} \gtrsim 200 M_{\odot}$  is required to reproduce the observed MZSFR with enhanced metal yields from pair-instability SNe. Observational data at  $z \gtrsim 6$  favor a galactic outflow model where the outflow rate is proportional to the supernova energy injection rate divided by the halo binding energy.

**Conclusions.** Very massive ( $\gtrsim 200 M_{\odot}$ ) stars can play important roles in the star formation and chemical enrichment histories of high- $z$  galaxies. They also have profound implications for transient sources of both electromagnetic waves and gravitational waves.

**Key words.** galaxies: evolution – galaxies: high-redshift – stars: massive – stars: luminosity function, mass function – supernovae: general – ISM: abundances

## 1. Introduction

The initial mass function (IMF) plays a pivotal role in astrophysics. It serves as a key connection between star formation and stellar evolution at small scales and galactic dynamics and baryon cycles at large scales, which makes it one of the most widely used functions in both theoretical and observational studies (Kroupa & Jerabkova 2021; Kroupa et al. 2024). The high-mass end of the IMF is particularly important in galaxy evolution, since star formation and metal enrichment is strongly regulated by the feedback from massive ( $\gtrsim 10 M_{\odot}$ ) stars via their ra-

diation, winds, supernova (SN) explosions, and metal yields (see reviews by, e.g., Eldridge & Stanway 2022; Ekström 2025). Besides, such massive stars, commonly formed in binary/multiple systems (e.g., Sana et al. 2012, 2014; Moe & Di Stefano 2017), are crucial for establishing a multi-messenger view of the Universe since they are the progenitors of various high-energy astrophysical processes/objects including energetic SN events, X-ray binaries, gamma-ray bursts, (binary) black holes and neutron stars and their mergers as gravitational wave sources (see, e.g., Mapelli 2021; Tauris & van den Heuvel 2023; Chen et al. 2024; Marchant & Bodensteiner 2024, for recent reviews).

\* e-mail: boyuan.liu@uni-heidelberg.de

Since the initial introduction of IMF by Salpeter (1955) as an invariant probability density distribution function, our understanding of IMF has evolved significantly. Recent advancements in theoretical calculations (e.g., Klessen et al. 2012; Schneider et al. 2012; Dopcke et al. 2013; Chon et al. 2021, 2024; Mathew & Federrath 2021; Mathew et al. 2023, 2025; Guszejnov et al. 2022; Hennebelle et al. 2022; Hix et al. 2023; Liu et al. 2024a; Tanvir & Krumholz 2024) and observations (e.g., Gunawardhana et al. 2011; Marks et al. 2012; Fraser et al. 2017; Ishigaki et al. 2018; Jeřábková et al. 2018; Rossi et al. 2021; Dib 2023; Rusakov et al. 2023; Yan et al. 2023) provide abundant hints for the environmental dependence of IMF regarding metallicity, turbulence, cloud/cluster mass, star formation rate, gas (surface) density and temperature, radiation and magnetic fields (reviewed by, e.g., Klessen & Glover 2023; Hennebelle & Grudić 2024). This points out the need to go beyond the assumption of a universal IMF in the mass range of  $0.01 - 100 M_{\odot}$  emerging from local Galaxy-scale observations (e.g., Kroupa 2001; Chabrier 2003), especially for studying distant, unresolved stellar systems formed in diverse conditions across cosmic history.

In fact, one explanation to the ‘excess’ of UV-luminous galaxies at  $z \gtrsim 10$  (including those with extremely blue UV spectra) recently discovered by the James Webb Space Telescope (JWST, e.g., Donnan et al. 2023a, 2024; Finkelstein et al. 2023, 2024; Harikane et al. 2023; Labbé et al. 2023; Pérez-González et al. 2023, 2025; Adams et al. 2024; Naidu et al. 2025)<sup>1</sup> involves enhanced abundances of massive stars through top-heavier IMFs (e.g., Inayoshi et al. 2022; Cueto et al. 2024; Trinca et al. 2024; Ventura et al. 2024; Jeong et al. 2025), which can be natural outcomes of the dense, metal-poor star-forming clouds at high  $z$  (e.g., Marks et al. 2012; Jeřábková et al. 2018; Chon et al. 2021). Besides, recent JWST observations find the peculiar chemical signatures of metal enrichment from very massive ( $\gtrsim 100 M_{\odot}$ ) stars such as enhanced N and C abundances in several high- $z$  galaxies (e.g., Charbonnel et al. 2023; Nagele & Umeda 2023; Vink 2023; Cameron et al. 2024; Nandal et al. 2024b,a; Watanabe et al. 2024; Gieles et al. 2025; Nandal et al. 2025; Schaerer et al. 2025; Naidu et al. 2025), which further highlights the important role of (very) massive stars in galaxy chemical evolution. Low- $z$  observations and chemical evolution models also favor (top-heavy) IMFs extending to the regime of very massive stars. For instance, Goswami et al. (2021) find that the abundance ratios between  $\alpha$  elements, O, and Fe in the thick disk of the MW can only be explained if the IMF extends beyond  $100 M_{\odot}$  up to  $350 M_{\odot}$ . Goswami et al. (2022). It is shown by Goswami et al. (2022) that a bi-modal, top-heavy IMF involving very massive stars is required to reproduce the Fe/O and N/O abundance ratios in nearby ( $z \lesssim 0.03$ ) metal-poor, low-mass, starburst galaxies.

In light of this, we explore the impact of IMF, in particular its high-mass end, on the (chemical) evolution of high- $z$  galaxies using the public semi-analytical galaxy evolution code A-SLOTH (Hartwig et al. 2022, 2024; Magg et al. 2022a). In order to better capture bursty star formation in high- $z$  galaxies (e.g., Naidu et al. 2025, Tacchella et al. in prep.) and the effects of very massive stars, we update the prescriptions for star formation and stellar feedback in A-SLOTH, which are coupled to a comprehensive

set of stellar evolution models (covering the metallicity range  $Z \sim 10^{-11} - 0.03$  and stellar mass range  $m_{\star} \sim 2 - 600 M_{\odot}$ ) (Costa et al. 2025, citation to be added). As an initial step, we focus on the general trends of high- $z$  galaxy chemical evolution reflected in the scaling relation between stellar mass, (gas-phase) metallicity, and star formation rate (SFR). In particular, recent JWST observations have reached a consensus on an invariant stellar mass-metallicity-star formation rate relation (MZSFR, Nakajima et al. 2023; Curti et al. 2024; Sarkar et al. 2025) up to  $z \sim 8$  and its breakdown at higher redshifts. Our goal is to jointly constrain the IMF and galactic outflow properties of high- $z$  galaxies using this MZSFR combined with the cosmic star formation history (CSFH, Bouwens et al. 2016; Donnan et al. 2023a,b; Harikane et al. 2023) and galaxy-halo connection (Tacchella et al. 2018) inferred from observations at  $z \sim 4 - 10$ . To do so, we run A-SLOTH on the merger trees constructed from a high-resolution cosmological simulation (Ishiyama et al. 2016) that resolves the smallest star-forming structures (with halo masses  $\sim 10^6 M_{\odot}$ ) in the standard  $\Lambda$ CDM universe. Therefore, while reproducing current observations biased by luminous objects at high  $z$ , our simulations self-consistently produce a large population of faint, low-mass, metal-poor galaxies (down to  $\sim 1000 M_{\odot}$  of stellar mass), which can provide guidance for future surveys.

The structure of our paper is as follows. In Section 2, we describe our galaxy evolution model with special focuses on the updates of star formation (Sec. 2.2) and stellar evolution (Sec. 2.4) models. In Section 3, we explain the simulation setup and the parameter space explored. In Section 4, we outline the observational constraints and define the corresponding likelihoods that quantify the agreement between observations and theoretical predictions. In Section 5, we show our main results. These include the likelihoods as functions of model parameters, through which we discuss the interplay between IMF and galactic outflows in galaxy chemical evolution (Sec. 5.1) and search for the best-fit model with the highest overall likelihood. The population of simulated galaxies in this model is then compared with the observed population in detail (Sec. 5.2). In Section 6, we discuss the implications of our results on high- $z$  transient sources (Sec. 6.1) and the uncertainties/caveats in our simulations (Sec. 6.2). Finally, our main findings are summarized in Section 7.

## 2. Galaxy evolution model

We use the public semi-analytical code A-SLOTH (Hartwig et al. 2022, 2024) to model galaxy evolution through dark matter merger trees<sup>2</sup>. In this Section, we first explain the basic model elements (Sec 2.1). Then we highlight the improvements made in this work with respect to Hartwig et al. (2022) on the prescription of galaxy size in star formation (Sec. 2.2) and the input stellar evolution data (Sec. 2.4) used to model stellar feedback (Sec. 2.3). We refer the reader to the code release and calibration papers (Magg et al. 2022a; Hartwig et al. 2022, 2024) for full details.

<sup>1</sup> There are alternative explanations with enhancements of the star formation efficiency (e.g., Inayoshi et al. 2022; Dekel et al. 2023; Somerville et al. 2025; Yung et al. 2025), variability of UV-emission/star formation (e.g., Shen et al. 2023), and stellar light-to-mass ratio (by tweaking stellar evolution rather than the IMF, e.g., Donnan et al. 2025; Liu et al. 2025a,b), reduction of dust attenuation (e.g., Ferrara 2024), and even modifications of the underlying cosmic structure formation (e.g., Liu & Bromm 2022; Shen et al. 2024).

<sup>2</sup> A merger tree describes the merger history of dark matter halos that leads to the formation of a certain target halo. Such merger trees are the primary input to A-SLOTH. They can be generated using the Extended Press-Schechter formalism or extracted from cosmological simulations, as detailed in Hartwig et al. (2022).

## 2.1. Galactic baryon cycle

The baryon mass budget in each halo is divided into four components: cold gas ( $M_{\text{cold}}$ ), hot gas ( $M_{\text{hot}}$ ), stars ( $M_{\star}$ )<sup>3</sup>, and outflows ( $M_{\text{out}}$ ). Here, cold gas refers to star-forming gas in a central region, while hot gas denotes all gas bound to the halo that is not cold including the warm and hot phases of the interstellar medium (ISM) and circumgalactic medium (CGM). The outflow mass is the cumulative mass of gas unbound from the halo by stellar feedback that is never reaccreted.

In each global timestep  $\Delta t_j$  when the merger tree<sup>4</sup> goes from level  $j + 1$  to  $j$ , every (post-merger) parent halo at redshift  $z_j$  inherits the mass of each baryonic component from its (progenitor) child halo(s) at  $z_{j+1} > z_j$ , which sets the initial condition ( $M_{\text{cold}}^0$ ,  $M_{\text{hot}}^0$ ,  $M_{\star}^0$ , and  $M_{\text{out}}^0$ ) at  $z_{j+1}$ . If the initial total mass of baryons is smaller than  $M_{\text{h}}\Omega_{\text{b}}/\Omega_{\text{m}}$  in the parent halo, additional hot gas with a total mass of  $\Delta M_{\text{acc,hot}} = M_{\text{h}}\Omega_{\text{b}}/\Omega_{\text{m}} - (M_{\text{cold}}^0 + M_{\text{hot}}^0 + M_{\star}^0 + M_{\text{out}}^0)$  is added to the halo, corresponding to smooth accretion from the intergalactic medium (IGM). Here,  $M_{\text{h}}$  is the halo (virial) mass,  $\Omega_{\text{m}}$  and  $\Omega_{\text{b}}$  are the cosmic average matter and baryon fractions. The IGM accretion is turned off for satellite galaxies and for any halos in ionized regions of the IGM, whose maximum child halo has a virial temperature  $T_{\text{vir}} < 10^4$  K (see sec. 2.5.2 in Hartwig et al. 2022). For simplicity, we do not include additional effects of galaxy mergers (i.e., enhanced star formation efficiency) beyond gas mass supplies and also ignore any additional loss of gas from tides or ram pressure in satellite galaxies other than shutting down the IGM accretion.

To accurately follow star formation and stellar feedback, sub-cycling is introduced within  $\Delta t_j$  using adaptive sub-timesteps (see sec. 2.4 in Hartwig et al. 2022). In each sub-timestep  $\delta t_i$ , the baryon masses are updated by

$$\begin{aligned} M_{\text{hot}}^{i+1} &= M_{\text{hot}}^i - \frac{\delta t_i M_{\text{hot}}^i}{t_{\text{con}}^i} - \delta M_{\text{out,hot}}^i + \delta M_{\text{heat}}^i \\ &\quad + \delta M_{\text{acc,hot}}^i + \delta M_{\text{loss},\star}^i, \\ M_{\text{cold}}^{i+1} &= M_{\text{cold}}^i + \frac{\delta t_i M_{\text{hot}}^i}{t_{\text{con}}^i} - \delta M_{\text{out,cold}}^i - \delta M_{\text{heat}}^i - \delta M_{\star}^i, \\ M_{\text{out}}^{i+1} &= M_{\text{out}}^i + \delta M_{\text{out,cold}}^i + \delta M_{\text{out,hot}}^i, \\ M_{\star}^{i+1} &= M_{\star}^i + \delta M_{\star}^i \simeq M_{\star}^i + \eta M_{\text{cold}}^i \frac{\delta t_i}{t_{\text{cold,ff}}^i}. \end{aligned} \quad (1)$$

Here,  $\delta t_i M_{\text{hot}}^i / t_{\text{con}}^i$  is the mass of hot gas converted to cold gas (on a timescale of  $t_{\text{con}}^i$ ),  $\delta M_{\text{heat}}^i$  is the mass of cold gas heated up by photo-ionization,  $\delta M_{\text{acc,hot}}^i$  is the mass of hot gas accreted from the IGM,  $\delta M_{\text{loss},\star}^i$  is the mass lost by stars (via winds and SNe),  $\delta M_{\star}^i$  is the mass of newly-formed stars, and  $\delta M_{\text{out,hot/cold}}^i$  is the mass of hot/cold gas blown away by galactic outflows. In the following subsections, we describe the derivations of these terms, which are classified into the inflow and outflow parts closely related to star formation (Sec. 2.2) and stellar feedback (Sec. 2.3), respectively.

<sup>3</sup> Currently, A-SLOTH records the cumulative mass of stars *ever formed* as  $M_{\star}$  which is distinct from the mass of active stars. The difference is within  $\sim 30\%$  for relatively young stellar populations with ages  $\lesssim 100$  Myr that are relevant for the observational data from JWST considered in this work.

<sup>4</sup> The root level ( $j = 1$ ) is defined by the target halo at the lowest redshift. Time goes backwards as the tree level increases.

## 2.2. Star formation

Star formation is only possible when gas can cool rapidly. In A-SLOTH, this requirement is embodied by a halo mass threshold determined by primordial thermochemistry, streaming motion between baryons and dark matter, and dissociation of  $\text{H}_2$  by Lyman-Werner radiation (Hartwig et al. 2022, see their sec. 2.3.1). The baryon cycle (Eq. 1) is only evolved for halos above this mass threshold, and each halo initially only contains hot gas  $M_{\text{hot}} = M_{\text{h}}\Omega_{\text{b}}/\Omega_{\text{m}}$ .

The terms  $\delta M_{\text{acc,hot}}^i$ ,  $\delta t_i M_{\text{hot}}^i / t_{\text{con}}^i$ , and  $\delta M_{\star}^i$  in Eq. 1 embody the inflow cascade that leads to star formation. The accretion rate of hot gas from the IGM is assumed to be constant within  $\Delta t_j$ , such that  $\delta M_{\text{acc,hot}}^i = \Delta M_{\text{acc,hot}} \delta t_i / \Delta t_j$ . For halos with  $T_{\text{vir}} > 10^4$  K where atomic cooling is efficient, the condensation of hot gas down to the central region occupied by cold gas and stars is governed by the dynamical timescale  $t_{\text{dyn}}^i$ , i.e.,  $t_{\text{con}}^i = t_{\text{dyn}}^i$ , given

$$t_{\text{dyn}}^i = \min\{R_{\star}^{3/2} / [G(M_{\star}^i + M_{\text{cold}}^i)]^{1/2}, R_{\text{vir}}^{3/2} / (GM_{\text{h}})^{1/2}\}, \quad (2)$$

where  $R_{\star}$  is the characteristic radius of the galaxy, and  $R_{\text{vir}}$  is the halo virial radius. The second term is meant to capture the initial collapse phase when the mass of cold gas and stars is very small. For minihalos with  $T_{\text{vir}} < 10^4$  K where cooling is typically driven by molecular hydrogen, the condensation is also limited by the cooling timescale  $t_{\text{cool}}^i$  as  $t_{\text{con}}^i = \max(t_{\text{dyn}}^i, t_{\text{cool}}^i)$ .

In a star-forming halo, the collapse of cold gas is governed by the mean free-fall timescale of cold gas  $t_{\text{cold,ff}}^i = (G\rho_{\text{cold}}^i)^{-1/2} \sim 2t_{\text{dyn}}^i$ , where  $\rho_{\text{cold}}^i = (M_{\text{cold}}^i + M_{\star}^i) / [(4\pi/3)R_{\star}^3]$ . Note that the original model of Hartwig et al. (2022) uses  $\rho_{\text{cold}}^i = M_{\text{cold}}^i / [(4\pi/3)R_{\star}^3]$  considering only the self-gravity of cold gas, here we further include the gravity of stars. The total mass of stars formed in this timestep is estimated as  $\delta M_{\star,\text{est}}^i = \eta M_{\text{cold}}^i \delta t_i / t_{\text{cold,ff}}^i$ , where  $\eta$  is the star formation efficiency (SFE) per mean free-fall time<sup>5</sup>, which is treated as a constant free parameter. Individual stars are then drawn from the IMF (see Sec. 2.4 below) with Poisson sampling according to  $\delta M_{\star,\text{est}}^i$ , as detailed in Sec. 2.3.2 in Hartwig et al. (2022). Their initial masses  $m_{\star}$  are summed up as  $\delta M_{\star}^i = \sum m_{\star} \simeq \delta M_{\star,\text{est}}^i$  and removed from the cold gas.

The newly formed stars are classified into two populations: extremely metal-poor/free Population III (Pop III) and metal-enriched Population II (Pop II), depending on the chemical composition of star-forming gas (see eq. 17 in Hartwig et al. 2022). The SFE and IMF of these two populations are modeled separately. Pop III stars are unimportant in this work because the observational data considered here only involve relatively massive halos with  $M_{\text{h}} \gtrsim 10^{9.5} M_{\odot}$  hosting mostly Pop II stars. Therefore, we fix the Pop III IMF and SFE ( $\eta_{\text{III}} = 8.15$ ) to the best-fit results of Hartwig et al. (2024, see their table 1) for simplicity. The Pop II SFE is also fixed to the best-fit value<sup>6</sup>  $\eta_{\text{II}} = 0.237$ ,

<sup>5</sup> Here, the mean free-fall time  $t_{\text{cold,ff}}^i$  is defined for cold gas in the central region within  $R_{\star}$  as a whole. In reality, star formation and the subsequent feedback can happen in smaller/denser clumps on a timescale much shorter than the mean free-fall time. In this case,  $\eta$  can be larger than unity. This is particularly true for first star formation on small timescales  $\sim 10^4 - 10^5$  yr in minihalos ( $M_{\text{h}} \lesssim 10^8 M_{\odot}$ ), where  $t_{\text{cold,ff}}^i \sim 10$  Myr (Hartwig et al. 2024).

<sup>6</sup> Given  $\eta = 0.237$ , the ratio of the hot gas condensation timescale  $t_{\text{con}}^i = t_{\text{dyn}}^i$  (for atomic-cooling halos) and the cold gas depletion timescale  $t_{\text{dep}}^i \equiv t_{\text{cold,ff}}^i / \eta$  is  $s = \eta t_{\text{dyn}}^i / t_{\text{cold,ff}}^i \sim 0.1$ , much smaller than the value  $s \sim 3$  found in the analytical model of Pantoni et al. (2019) for local early-type galaxies in massive halos ( $M_{\text{h}} \sim 10^{11.5} - 10^{13.5} M_{\odot}$ ). This difference may imply that the condensation of hot gas is more rapid

since its effects are mostly degenerate with those of galactic outflow parameters that will be explored in detail (see Sec. 2.3). On the other hand, the Pop II IMF is varied to evaluate its impact on high- $z$  galaxy chemical evolution (see Sec. 2.4).

The galaxy radius  $R_*$  plays an important role in the inflow cascade, as it controls the timescales of inflow/cooling and collapse. In the original model of Hartwig et al. (2022),  $R_*$  is set to the scale radius of the halo  $R_s = R_{\text{vir}}/c_{\text{DM}}$ , given the halo's concentration  $c_{\text{DM}}$ . However, given the same  $M_h$ ,  $R_s$  is much larger compared with the (stellar) half-mass/light radius  $R_{50}$  of galaxies in observations and cosmological (zoom-in) simulations. To make this comparison, we derive  $R_{50}$  as a function of  $M_h$  using the fitting formula for  $c_{\text{DM}}(M_h)$  from Correa et al. (2015, see their appendix B1). For simulation results of the (3D) half-mass radius, we consider the scaling relation  $R_{50} = 0.053[R_{\text{vir}}/(0.7 \text{ kpc})]^{0.894} \text{ kpc}$  from the FIREbox simulations (for  $z \lesssim 5$ , Rohr et al. 2022) and that from the NIHAO and VELA zoom-in simulations (for  $z \lesssim 7$ , Jiang et al. 2019)  $R_{50} = 0.02R_{\text{vir}}(c_{\text{DM}}/10)^{-0.7}(1+z)^{-0.2}$ , where the factor  $(1+z)^{-0.2}$  is introduced to reproduce the redshift evolution of median galaxy-halo size relation in (abundance matching) observations (Somerville et al. 2018).

For observational constraints on the (2D) half-light radius, we adopt the stellar-halo mass relation (SHMR) from the semi-empirical model in Tacchella et al. (2018)

$$M_{*,\text{SHMR}} = \frac{0.05[(1+z)/5]^{-0.6} M_h}{(M_h/M_c)^{-1} + (M_h/M_c)^{0.3}}, \quad (3)$$

where  $M_c = 1.6 \times 10^{11} M_\odot$ . We first derive the stellar mass as  $M_* = M_{*,\text{SHMR}}(M_h, z)$ , which is then substituted to a given galaxy mass-size relation (GMSR) from observations to estimate  $R_{50}(M_*(M_h))$ . For the latter, we consider the fitting formulae from Arca-Sedda & Capuzzo-Dolcetta (2014, for  $z \sim 0$ ), Mowla et al. (2019, for  $z \lesssim 3$ ), and (Langeroodi & Hjorth 2023, for  $z \sim 4 - 10$ ). We also consider the recent measurements of  $R_{50}/R_{\text{vir}}$  from the COSMOS-Web survey (Yang et al. 2025, for  $z \sim 2 - 7$ ). Note that these observational data may not necessarily cover the high- $z$  regime ( $z \sim 4 - 10$ ) that we are concerned with. In this case, we simply make extrapolations by assuming that the relation for the highest redshift bin applies to higher redshifts.

As illustrated in Fig. 1 for  $z = 7$ , we find that  $R_s$  is larger than  $R_{50}$  by at least a factor of 2 and up to a factor of 20 for  $M_h \sim 10^{9.5} - 10^{12} M_\odot$  at  $z \sim 4 - 10$ . This indicates that  $R_s$  may not be a good choice for  $R_*$ . In fact, as discussed in Appendix A, increasing  $R_*$  not only reduces the overall star formation rate but also suppresses the burstiness of star formation, and the old approach with  $R_* = R_s$  produces a scatter around the star-formation main sequence (SFMS) that is much smaller (by a factor of  $\sim 2 - 3$ ) than that seen in observations. Therefore, for atomic-cooling halos ( $T_{\text{vir}} > 10^4 \text{ K}$ ), we instead set  $R_*$  to  $2.5R_{50}$  as an approximation of the radius  $R_{80}$  that encloses 80% of the total stellar mass (Mowla et al. 2019). Here, we adopt the fitting formula from Jiang et al. (2019) to calculate  $R_{50}$  as a conservative estimate among the references considered above, which also

in the small ( $M_h \sim 10^{9.5} - 10^{11.5} M_\odot$ ) high- $z$  star-forming galaxies simulated here, likely due to their compact nature and strong cold accretion flows (Kiyuna et al. 2023, 2024). Besides, cold gas depletion may also be slowed down by rotational support in star-forming galaxies which are already dominated by disk-like morphologies at  $z \sim 4 - 10$  (e.g., Ferreira et al. 2023; Kartaltepe et al. 2023; Lee et al. 2024; Sun et al. 2024; Tohill et al. 2024; Wang et al. 2025b).

<sup>7</sup> For minihalos with  $T_{\text{vir}} < 10^4 \text{ K}$  ( $M_h \lesssim 10^8 M_\odot$ ) typically hosting Pop III star formation via molecular cooling, we still use the old approach  $R_* = R_s$  to avoid recalibration of Pop III parameters.

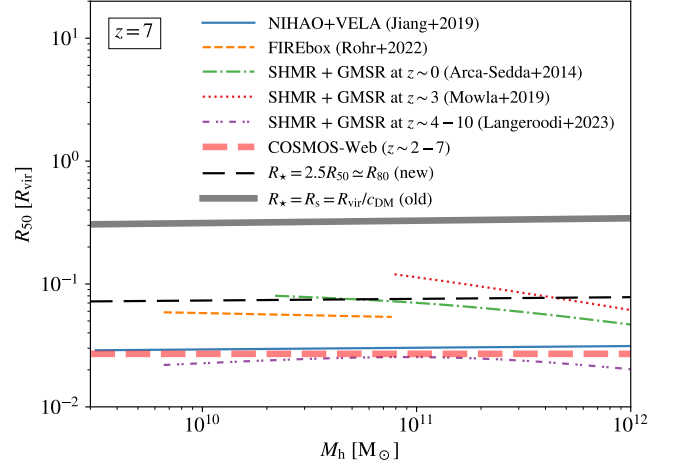


**Fig. 1.** Scaling relation between galaxy half-mass/light radius (in units of  $R_{\text{vir}}$ ) and halo mass at  $z = 7$ . The solid and dashed curves show the fitting formulae of half-mass radius from the NIHAO and VELA simulations (Jiang et al. 2019) and from the FIREbox simulations (Rohr et al. 2022), respectively. We also plot the empirical results for half-light radii based on the SHMR in Tacchella et al. (2018) at  $z = 7$  (Eq. 3) combined with the extrapolation of the GMSR from Arca-Sedda & Capuzzo-Dolcetta (2014,  $z \sim 0$ , dash-dotted), Mowla et al. (2019,  $z \sim 3$ , dotted), and Langeroodi & Hjorth (2023,  $z \sim 4 - 10$ , dot-dash-dotted). The thick dashed line shows the median ratio of the galaxy half-light radius to halo virial radius  $R_{50}/R_{\text{vir}} = 2.7\%$  at  $z \sim 2 - 7$  from the COSMOS-Web survey (Yang et al. 2025, see their fig. 10). The thick solid curve shows the old model for galaxy size  $R_* = R_s$  of Hartwig et al. (2022), while the long-dashed curve shows the new model  $R_* = 2.5R_{50}$  adopted in this work given  $R_{50}$  from Jiang et al. (2019).

covers the largest dynamical range of  $M_h$  and agrees well with the median ratio  $R_{50}/R_{\text{vir}} = 0.027$  of galaxies at  $z \sim 2 - 7$  observed in the COSMOS-Web survey (Yang et al. 2025, see their fig. 10). In the end, we have

$$R_* = 2.5R_{50} = 0.5R_{\text{vir}}(c_{\text{DM}}/10)^{-0.7}(1+z)^{-0.2}. \quad (4)$$

In this way,  $R_*$  is reduced by a factor of  $\sim 4$  compared with the old model, such that the scatter around SFMS is enhanced by a factor of  $\sim 2$ , achieving a better agreement with observations (see Appendix A).

Interestingly, our  $R_*$  values are generally consistent with the half-mass radii predicted by the THESAN-ZOOM simulations for  $z \sim 4 - 10$  (McClymont et al. 2025, see their fig. 2) and those from lower- $z$  observations (Mowla et al. 2019; Rohr et al. 2022), although they are systematically larger than the half-light radii in JWST observations at similar redshifts (Langeroodi & Hjorth 2023) by a factor of  $\sim 3$ . This shows that different theoretical predictions and definitions of galaxy size have non-negligible discrepancies partially due to observational limitations (e.g., geometry and sensitivity). We plan to improve the prescription for  $R_*$  with physically motivated definitions of galaxy size and more robust scaling relations (e.g., Arjona-Galvez et al. 2025) in future work.

### 2.3. Stellar feedback: heating, outflows, and metal enrichment

In addition to the inflow cascade discussed in the previous subsection, one has to consider the outflow cascade driven by stellar



feedback<sup>8</sup> to complete the baryon cycle, which is characterized by  $\delta M_{\text{heat}}^i$ ,  $\delta M_{\text{out,cold}}^i$ , and  $\delta M_{\text{out,hot}}^i$  in Eq. 1. Individual stars with  $m_\star > 5 M_\odot$  are tracked in A-SLOTH to compute these feedback terms. We call these stars ‘massive stars’ henceforth<sup>9</sup>. When the massive stars are alive, they power photoheating feedback, which is captured by  $\delta M_{\text{heat}}^i$ : the mass of cold gas heated up to  $\sim 10^4$  K in HII regions. It is calculated from the production rates  $\dot{q}_{\text{ion}}$  of (hydrogen) ionizing photons<sup>10</sup> of active massive stars in the current sub-timestep  $\delta t_i$  as detailed in sec. 2.3.3 in Hartwig et al. (2022). For minihalos with  $T_{\text{vir}} < 10^4$  K that are unable to bind ionized gas, we add the heated gas directly to outflows ( $\delta M_{\text{out,cold}}^i$ , see below) rather than the hot phase ( $\delta M_{\text{heat}}^i$ ).

A massive star dies within  $\delta t_i$  if the time past after its birth exceeds its lifetime  $t_\star$ . The dying stars can undergo SN explosions that drive galactic outflows, as denoted by the  $\delta M_{\text{out,k}}^i$  terms, where  $k = \text{cold, hot}$ . The *expected* outflow mass is estimated by

$$\delta \hat{M}_{\text{out,k}}^i = \frac{E_{\text{SNe}}^i f_k}{E_{\text{bind,k}} \gamma_{\text{out}}} M_k^i, \quad f_k = \frac{E_{\text{bind,k}}^i M_k^i}{E_{\text{bind,hot}}^i M_{\text{hot}}^i + E_{\text{bind,cold}}^i M_{\text{cold}}^i}. \quad (5)$$

Here,  $E_{\text{SNe}}^i = \sum e_{\text{SN}}$  is the total energy of SNe exploded within  $\delta t_i$ ,  $E_{\text{bind,k}}^i$  is the binding energy of component  $k$  given by eqs. 24 and 25 in Hartwig et al. (2022) based on Chen et al. (2022), and  $\gamma_{\text{out}}$  is the outflow efficiency. Following Chen et al. (2022), we adopt a phenomenological model for  $\gamma_{\text{out}}$  as

$$\gamma_{\text{out}} = (M_{\text{vir,peak}}/M_{\text{out0}})^{\alpha_{\text{out}}}, \quad (6)$$

where  $M_{\text{vir,peak}}$  is the peak virial halo mass, and the characteristic mass  $M_{\text{out0}}$  and power-law slope  $\alpha_{\text{out}}$  are free parameters to be constrained by observations (together with the IMF). For  $\alpha_{\text{out}} > 0$ ,  $M_{\text{out0}}$  defines the halo mass scale above (below) which galactic outflows are suppressed (enhanced) by the deeper (shallower) potential wells of larger (smaller) halos. The strength of this halo mass dependence is governed by  $\alpha_{\text{out}}$ . Given  $\alpha_{\text{out}} > 0$  fixed,  $M_{\text{out0}}$  also determines the overall outflow efficiency. Since  $M_{\text{out0}}$  becomes meaningless in Eq. 6 when  $\alpha_{\text{out}} = 0$ , we further extend this model by

$$\gamma_{\text{out}} = 10^{10} M_\odot / M_{\text{out0}} \quad \text{if} \quad \alpha_{\text{out}} = 0, \quad (7)$$

such that increasing  $M_{\text{out0}}$  always enhances galactic outflows for  $\alpha_{\text{out}} \geq 0$ , and increasing  $\alpha_{\text{out}}$  boosts (reduces) outflows in small (large) halos with  $M_{\text{vir,peak}}$  below (above)  $M_{\text{out0}}$  for  $\alpha_{\text{out}} > 0$ .

Given the expected value from Eq. 5, the true outflow mass is limited by the gas mass immediately available  $\delta M_{\text{out,k,max}}^i$  in practice, i.e.,  $\delta M_{\text{out,k}}^i = \min(\delta \hat{M}_{\text{out,k}}^i, \delta M_{\text{out,k,max}}^i)$ . For cold gas, we have  $\delta M_{\text{out,cold,max}}^i = M_{\text{cold}}^i - \delta M_{\text{heat}}^i - \delta M_\star^i$ . The excess mass

$\delta M_{\text{out,cold,exc}}^i = \max(\delta \hat{M}_{\text{out,cold}}^i - \delta M_{\text{out,cold,max}}^i, 0)$  is added to hot outflows  $\delta \hat{M}_{\text{out,hot}}^i$ , whose mass limit is  $\delta M_{\text{out,hot,max}}^i = M_{\text{hot}}^i (1 - \delta t_i / t_{\text{con}}^i) + \delta M_{\text{acc,hot}}^i + \delta M_{\text{heat}}^i$ .

In addition to radiative and mechanical feedback, we also consider chemical feedback, i.e., metal enrichment of the ISM/CGM/IGM by stellar winds and SNe from massive stars. Similar to the overall baryon mass budget, the mass of gas-phase<sup>11</sup> metals in a halo is divided into the bound ( $M_{\text{gal,metal}}^i$ ) and unbound ( $M_{\text{out,metal}}^i$ ) components, which are evolved by

$$M_{\text{gal,metal}}^{i+1} = \frac{(M_{\text{gal,metal}}^i + \delta M_{\text{metal}}^i)(M_{\text{cold}}^{i+1} + M_{\text{hot}}^{i+1})}{M_{\text{cold}}^{i+1} + M_{\text{hot}}^{i+1} + \delta M_{\text{out}}^i + \delta M_\star^i}, \quad M_{\text{out,metal}}^{i+1} = M_{\text{out,metal}}^i + \frac{(M_{\text{gal,metal}}^i + \delta M_{\text{metal}}^i)\delta M_{\text{out}}^i}{M_{\text{cold}}^{i+1} + M_{\text{hot}}^{i+1} + \delta M_{\text{out}}^i + \delta M_\star^i}, \quad (8)$$

where  $\delta M_{\text{out}}^i \equiv \delta M_{\text{out,cold}}^i + \delta M_{\text{out,hot}}^i$  is the total mass of outflows generated in  $\delta t_i$ , and  $\delta M_{\text{metal}}^i$  is the total mass of metals gained by the halo:

$$\delta M_{\text{metal}}^i = \delta M_{\text{metal},\star}^i + c_{\text{ZIGM}} \delta M_{\text{acc,hot}}^i Z_{\text{IGM}}. \quad (9)$$

Here, by metals we mean elements with atomic numbers no smaller than 6, ignoring those between Helium and Carbon that are unimportant for galaxy and stellar evolution, whose abundances are fixed to the primordial values from Big Bang Nucleosynthesis. The first term of Eq. 9 accounts for the in-situ metals ejected by massive stars,  $\delta M_{\text{metal},\star}^i = \sum m_Z$ . Similarly,  $\delta m_{\text{loss},\star}^i = \sum \delta m_{\text{loss},\star}^i$  in Eq. 1 denotes the overall mass of baryons lost by stars (with  $m_\star > 5 M_\odot$ ), which is returned to the hot phase of ISM/CGM. For simplicity, the metal/total mass return of each massive star is modeled as a single event at its death. Therefore, the summations above go over dying stars, where  $m_Z$  is the total mass of metals dispersed via winds and SN by a star throughout its lifetime. We further make the approximation  $\delta m_{\text{loss},\star}^i = m_\star$ . Note that in the high- $z$ , low-mass galaxies considered in our work, recycling of stellar baryons makes minor ( $\lesssim 10\%$ ) contributions to the total gas mass budget.

The second term of Eq. 9 accounts for the metals accreted from the IGM, where  $Z_{\text{IGM}}$  is the IGM metallicity at the location of the halo, and  $c_{\text{ZIGM}} \geq 1$  is a clumping factor. The latter is introduced by Hartwig et al. (2024) motivated by the centrally concentrated distribution of metals in SN bubbles around early protogalaxies found in 3D hydrodynamic simulations (e.g., Ritter et al. 2015; Magg et al. 2022b), and the fact that accretion flows favor denser, colder pockets of gas with higher metallicities than the IGM average. We adopt  $c_{\text{ZIGM}} = 3.32$  according to Hartwig et al. (2024), which is chosen to reproduce the metallicity distribution of metal-poor stars and the mass-metallicity relation of satellite galaxies in the Milky Way (MW)<sup>12</sup>. The assumption underlying Eq. 8 is that the metals are mixed uniformly

<sup>8</sup> Feedback from active galactic nuclei (AGN) can also regulate galaxy evolution, especially in massive galaxies. Since we focus on relatively small (dwarf) galaxies ( $M_\star \sim 10^7 - 10^{10} M_\odot$ ,  $M_h \sim 10^{9.5} - 10^{11.5} M_\odot$ ) at  $z \gtrsim 4$ , AGN feedback is ignored for simplicity. The roles played by AGN feedback in dwarf galaxies are under intense investigation (e.g., Koudmani et al. 2022, 2024; Aravindan et al. 2023; Sharma et al. 2023; Hazenfratz et al. 2025).

<sup>9</sup> Our definition of massive stars is less strict than the commonly used one for core carbon burning, which typically requires  $m_\star \gtrsim 8 M_\odot$ .

<sup>10</sup> For simplicity, we adopt a constant  $\dot{q}_{\text{ion}}$  throughout the lifetime of each massive star as the lifetime-average value calculated from detailed stellar spectra evolution (Klessen & Glover 2023).

<sup>11</sup> For simplicity, we ignore the depletion of gas-phase metals by the growth of dust grains. As shown by Rémy-Ruyer et al. (2014), the depletion by dust growth is important for galaxies observed in the local Universe with  $[\text{O}/\text{H}] \gtrsim -0.7$ , where the fraction of metals converted to dust starts to settle to a non-negligible constant value  $\sim 0.3$  corresponding to the equilibrium between dust growth and destruction. However, for the high- $z$  galaxies considered here, the fraction of metals in dust is expected to be much smaller (down to  $\sim 0.003$ ) due to their short star formation timescales ( $\lesssim 0.5$  Gyr) according to chemical evolution models (see sec. 4 of Rémy-Ruyer et al. 2014, and the references therein). Therefore, the treatment of dust should not affect our conclusions.

<sup>12</sup> We have found by numerical experiments that the clumping factor is only important for low-mass galaxies ( $M_\star \lesssim 10^{7.5} M_\odot$ ) that are mostly

into the gas reservoir currently retained by the halo and that outflows carry out metals proportionally from this reservoir.

Given  $M_{\text{gal,metal}}^i$ , we derive the average gas-phase metallicity of the galaxy as  $Z_{\text{ave}} = M_{\text{gal,metal}}^i / (M_{\text{cold}}^i + M_{\text{hot}}^i)$ . The metallicity of star-forming gas can differ from this average value significantly due to inhomogeneous enrichment (Xu et al. 2016; Ritter et al. 2016; Magg et al. 2022b). To capture this effect, we apply a shift factor  $d \log Z$  to estimate the metallicity of newly-formed stars  $\delta M_{\star}^i$  as  $Z_{\star} = Z_{\text{ave}} \times 10^{d \log Z}$ , where  $d \log Z$  is drawn randomly from a normal distribution based on Tarumi et al. (2020), as detailed in appendix A.4 in Hartwig et al. (2022). On the other hand,  $M_{\text{out,metal}}^i$  is added to the enriched region (outflow bubble) around the halo, whose expansion is modeled as a pressure-driven snowplow. The local IGM metallicity  $Z_{\text{IGM}}$  is estimated from the properties of all outflow bubbles that enclose the halo. The reader is referred to sec. 2.5.1 in Hartwig et al. (2022) for details on the calculation of bubble properties and  $Z_{\text{IGM}}$ . The same approach is used to predict the abundance of any specific element with the same shift factor  $d \log Z$  assuming element-independent metal mixing<sup>13</sup>.

## 2.4. Stellar populations

As shown in the last subsection, the stellar feedback terms in the baryon cycle are determined by the properties of massive stars, namely, the production rate of ionizing photons  $\dot{q}_{\text{ion}}$ , lifetime  $t_{\star}$ , metal yield  $m_Z$ , and SN energy ejection  $e_{\text{SN}}$ . In A-SLOTH, these quantities are calculated from the initial stellar mass  $m_{\star}$  using fitting formulae (for  $\dot{q}_{\text{ion}}$  and  $t_{\star}$ ) and nearest-neighbor interpolation over pre-computed tables (for  $m_Z$  and  $e_{\text{SN}}$ ) from single star evolution models.

During star formation events,  $m_{\star}$  is sampled from the IMF, modeled separately for Pop III and Pop II stars (Hartwig et al. 2022, see their sec. 2.1.3 and 2.3.2). Pop III stars typically form in the extremely metal-poor/free regime with  $Z \lesssim 10^{-5} Z_{\odot}$ , where  $Z_{\odot} = 0.0142$  is the bulk solar metallicity (Allende Prieto et al. 2001; Asplund et al. 2004, 2009)<sup>14</sup>. Their IMF is modeled as a power-law, whose mass bounds ( $m_{\text{min,III}}$ ,  $m_{\text{max,III}}$ ) and slope ( $\alpha_{\text{III}}$ ) are in principle free parameters considering the diverse predictions from simulations (e.g., fig. 6 in Klessen & Glover 2023). In this work, we fix these parameters to the best-fit values from Hartwig et al. (2024) for simplicity:  $m_{\text{min,III}} = 13.6$ ,  $m_{\text{max,III}} = 197$ , and  $\alpha_{\text{III}} = 1.77$ . Our focus is metal-enriched ( $Z \gtrsim 10^{-5} Z_{\odot}$ ) Pop II stars that are inferred to be the dominant population in galaxies observed by JWST at  $z \gtrsim 5$  (Riaz et al. 2022; Finkelstein et al. 2023). Unlike Hartwig et al. (2022), where the Pop II stars follow the Kroupa (2001) IMF in a fixed mass range  $m_{\star} \in [0.01, 100] M_{\odot}$ , we allow the upper mass limit

too faint to show up in high- $z$  observations, and therefore, does not change our conclusions, as long as it is not too large ( $c_{\text{ZIGM}} \lesssim 3$ ).

<sup>13</sup> In reality, different metal elements in star-forming gas can experience different degrees of inhomogeneous metal mixing due to their distinct cooling rates (Hartwig & Yoshida 2019). This effect is ignored for simplicity because we are mainly concerned with the bulk metallicity that is closely traced by one element, oxygen, in observations.

<sup>14</sup> Throughout this paper,  $Z$  denotes the bulk absolute metallicity (i.e., mass fraction of metals). The (logarithmic) abundance of an element  $X$  with respect to the solar abundance is written as  $[X/H]$ . For instance,  $\log(\text{O}/H) + 12 = 7.69$  corresponds to  $[\text{O}/H] = -1$ , which denotes an oxygen abundance lower than the solar value by a factor of 10. Here, we take the (primordial) solar oxygen abundance  $\log(\text{O}/H) + 12 = 8.69$  from Asplund et al. (2009), who also provide the solar abundances of other elements. The same terminology is used for the abundance ratio of two elements (with respect to the solar ratio).

$m_{\text{max}}$  to change between 100 and 600  $M_{\odot}$  while keeping the high-mass end slope  $\alpha_{\text{II}} = 2.3$  and the low-mass end ( $m_{\star} < 1 M_{\odot}$ ) shape unchanged. For simplicity, we assume that  $m_{\text{max}}$  is invariant within each simulation, and therefore, meant to characterize the galaxy-population-averaged IMF. We defer the investigation of more complex IMF models with environmental dependence (e.g., Gunawardhana et al. 2011; Marks et al. 2012; Jeřábková et al. 2018; Dib 2023; Rusakov et al. 2023) to future work. We note that a shift of the IMF towards a more top-heavy nature at redshifts  $\gtrsim 5$  is expected on general physical grounds, such as the elevated CMB temperature floor (e.g., Larson 1998).

In the original approach of Hartwig et al. (2022, see their sec. 2.1.3), one single model is used for each population of stars without any metallicity dependence within the population. In other words, there are effectively only two metallicity bins:  $Z \lesssim 10^{-5} Z_{\odot}$  (Pop III) and  $Z \gtrsim 10^{-5} Z_{\odot}$  (Pop II). The fitting formulae for  $\dot{q}_{\text{ion}}$  and  $t_{\star}$  are taken from Schaerer (2002) and Stahler & Palla (2008). A universal function of  $e_{\text{SN}}(m_{\star})$  is adopted for both populations of stars, where core-collapse SNe (CCSNe) explode with  $e_{\text{SN}} = 10^{51} \text{ erg s}^{-1}$  from stars with  $m_{\star} \in [10, 40] M_{\odot}$ , while stars in the mass range  $m_{\star} \in [140, 260] M_{\odot}$  produce pair-instability SNe with  $e_{\text{SN}} = 3.3 \times 10^{52} \text{ erg s}^{-1}$ . The relevant SN metal yield tables are provided by Nomoto et al. (2013) and Kobayashi et al. (2006) for Pop III and Pop II stars, respectively.

In this work, we instead adopt a denser grid of stellar evolution models<sup>15</sup> computed with the PARSEC code v2.0 (Bressan et al. 2012; Costa et al. 2019; Nguyen et al. 2022), which covers the full metallicity range  $Z \sim 10^{-11} - 0.03$  with 13 bins and a broad mass range  $m_{\star} \sim 2 - 600 M_{\odot}$  (Costa et al. 2025, see their table 1)<sup>16</sup>. The  $Z = 10^{-11}$  model is applied to metal-free ( $Z = 0$ ) Pop III stars, while the rest describe extremely metal-poor Pop III stars ( $Z \sim 10^{-8.5} - 10^{-7}$ )<sup>17</sup> and Pop II stars<sup>18</sup>. The fates of these stars as well as the corresponding metal yields are derived using the methodology in Goswami et al. (2021) and Goswami et al. (2022). Specifically, stars with zero-age main sequence (ZAMS) mass  $m_{\star} > 5 M_{\odot}$  end their life as white dwarfs, electron-capture SNe (ECSNe), CCSNe, failed SNe (FSNe), pulsational pair-instability SNe (PPISNe), pair-instability SNe (PISNe), or direct-collapse black holes (DBHs). Here, white dwarfs, FSNe and DBHs have negligible energy ejection ( $e_{\text{SN}}$ ). We adopt the typical values of  $e_{\text{SN}}$  from SN explosion simulations for the other fates:  $e_{\text{SN}} = 10^{51} \text{ erg s}^{-1}$  for ECSNe and CCSNe,  $e_{\text{SN}} = 3.3 \times 10^{51} \text{ erg s}^{-1}$  for PPISNe, and  $e_{\text{SN}} = 3.3 \times 10^{52} \text{ erg s}^{-1}$  for PISNe. Unlike the old models of Hartwig et al. (2022) that only consider metal yields from SNe,

<sup>15</sup> <https://stev.oapd.inaf.it/PARSEC/>

<sup>16</sup> Costa et al. (2025) also provide tracks of more massive stars with  $m_{\star} \sim 600 - 2000 M_{\odot}$  for the lowest three metallicity bins  $Z = 10^{-11}$ ,  $10^{-6}$ , and  $10^{-4}$ . These models are not considered, as we focus on the regime with  $m_{\text{max}} \leq 600 M_{\odot}$ . Very massive ( $\gtrsim 600 M_{\odot}$ ) stars beyond this regime can also play important roles in the (chemical) evolution of high- $z$  galaxies (e.g., Nagele & Umeda 2023; Vink 2023; Nandal et al. 2024b,a, 2025; Schaerer et al. 2025), which is a promising topic for follow-up studies.

<sup>17</sup> Pop III stars are assigned to the lowest two metallicity bins  $Z = 10^{-11}$  and  $10^{-6}$  in Costa et al. (2025) by nearest neighbor interpolation (in the  $\log Z$  space) with a middle point  $Z = 10^{-8.5}$ . This is motivated by the fact that stellar evolution converges to the metal-free mode for  $Z \lesssim 10^{-9}$  (see, e.g., fig. 1 in Larkin et al. 2023). Here, our definition of Pop III stars is based on the physics of star formation that drive the transition of IMF from the bottom-heavy Pop II regime to the top-heavy Pop III regime around a critical metallicity  $Z \sim 10^{-7}$  (Chiaki et al. 2017; Chon et al. 2021), which is broader than ‘metal-free’ stellar evolution.

<sup>18</sup> Stars with  $Z \gtrsim 0.006$  are usually called Population I (Costa et al. 2025). Here, we still classified them as Pop II for simplicity.

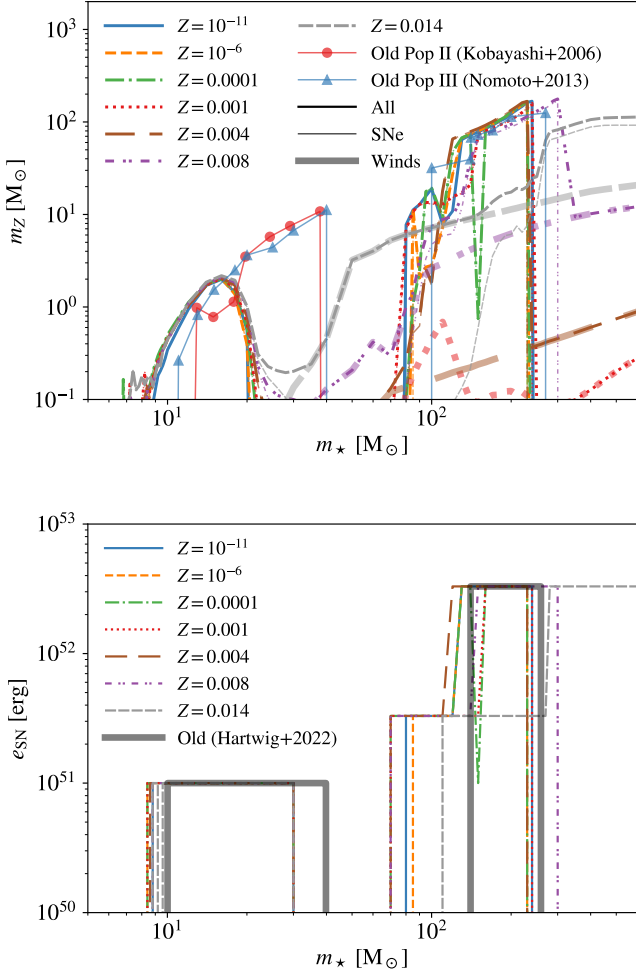


**Fig. 2.** Metal yields (top) and SN energy (bottom) as functions of initial stellar mass for  $Z = 10^{-11}$  (solid),  $10^{-6}$  (dashed),  $0.0001$  (dash-dotted),  $0.001$  (dotted),  $0.004$  (long-dashed),  $0.008$  (dot-dash-dotted), and  $0.014$  (densely-dashed). In the top panel, the yields from SNe, winds, and all combined are shown with the thin, thick, and intermediate curves. The thin curves marked by circles and triangles show the old SN yields adopted by Hartwig et al. (2022) for Pop II and Pop III stars from Kobayashi et al. (2006, for  $Z = 0.001$ ) and Nomoto et al. (2013, for  $Z = 0$ ), respectively. Here, Kobayashi et al. (2006) only consider stars in the mass range  $m_\star \sim 10 - 40 M_\odot$ , and zero yields are assumed for stars outside this range by Hartwig et al. (2022). In the bottom panel, the old SN energy model of Hartwig et al. (2022) is shown with the thick solid curve.

our new models also include the contributions of stellar winds, which can play important roles in metal enrichment (e.g., Cescutti & Chiappini 2010; Farmer et al. 2021; Liu et al. 2021; Jeena et al. 2023; Vink 2023; Higgins et al. 2023, 2025; Ma et al. 2025). Our yields are mildly different from those already published by Costa et al. (2025, see, e.g., their Fig. 7) even if they are derived from the same PARSEC evolutionary tracks. The reason is that we calculate the ejecta mass during CCSNe with the delayed formalism by Fryer et al. (2012), whereas Costa et al. (2025) adopt the explodability models from Limongi & Chieffi (2003) and Chieffi & Limongi (2004). The main difference is that at intermediate and high metallicity ( $Z \gtrsim 0.005$ ) our models predict a larger ZAMS mass range for direct collapse black holes with respect to successful CCSNe (Spera et al. 2019). This difference has negligible impact on the results presented here.

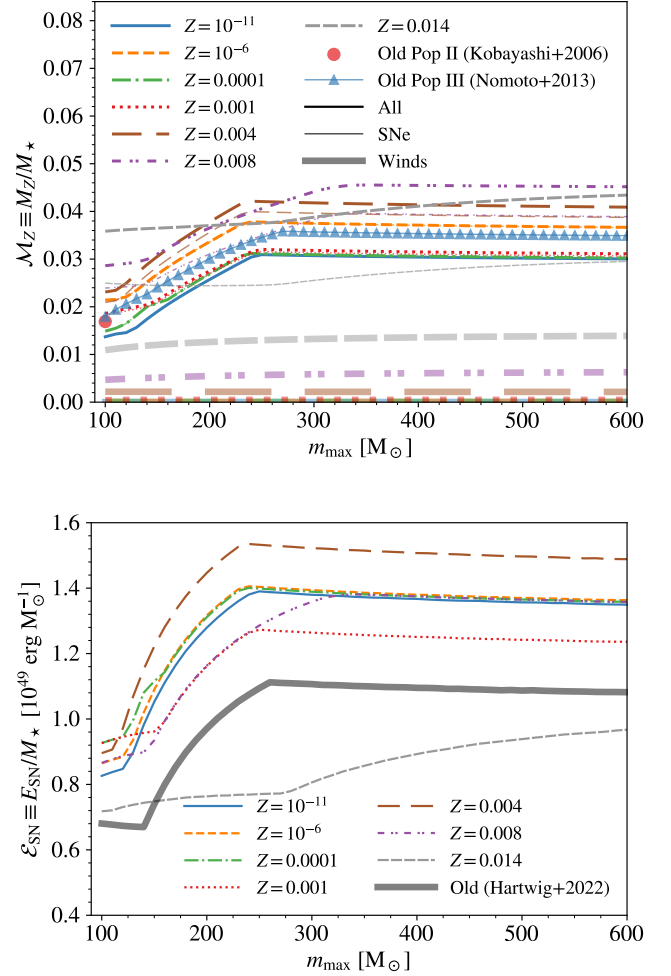


**Fig. 3.** Total metal yield (top) and SN energy output (bottom) per unit stellar mass as functions of IMF upper mass limit for  $Z = 10^{-11}$  (solid),  $10^{-6}$  (dashed),  $0.0001$  (dash-dotted),  $0.001$  (dotted),  $0.004$  (long-dashed),  $0.008$  (dot-dash-dotted), and  $0.014$  (densely-dashed). Here, the IMF shape is assumed to follow Kroupa (2001) with the high-mass end described by a power-law  $dN/dm_\star \propto m_\star^{-2.3}$ . In the top panel, the yields from SNe, winds, and all combined are shown with the thin, thick, and intermediate curves. The big circle shows the result for the old Pop II model of Hartwig et al. (2022) at  $m_{\text{max}} = 100 M_\odot$  based on the SN yields from Kobayashi et al. (2006, for  $Z = 0.001$ ). The thin curve marked by triangles shows the results for the old Pop III model of Hartwig et al. (2022) based on the SN yields from Nomoto et al. (2013, for  $Z = 0$ ). In the bottom panel, the results for the old SN energy model of Hartwig et al. (2022) are shown with the thick solid line.

In Fig. 2, we compare our new models for  $m_Z(m_\star)$  (top panel) and  $e_{\text{SN}}(m_\star)$  (bottom panel) at seven select metallicities with the old models of Hartwig et al. (2022). Clearly, both  $m_Z$  and  $e_{\text{SN}}$  show non-negligible metallicity dependence in our new models. Besides, the variations with  $Z$  are complex and non-monotonic in the metal-poor regime relevant for Pop III and Pop II stars with  $Z \lesssim 0.004$ . For more metal-rich stars, the effects of stellar winds become important, shifting the curves to the right (larger  $m_\star$ ) due to reduced pre-SN masses. The main difference between the new and old models is that in our case, the metal yields from CCSNe are significantly reduced by fall-back at  $m_\star \sim 20 - 70 M_\odot$ , while this fall-back dominated regime occurs at  $m_\star \sim 40 - 100 M_\odot$  in Hartwig et al. (2022). Besides, our models consider ECSNe from  $m_\star \sim 8 - 10 M_\odot$  and PPISNe

from  $m_\star \sim 70 - 120 M_\odot$  that are absent in the old models. To better demonstrate the difference, In Fig. 3, we show the corresponding IMF-integrated total metal yield (top panel) and SN energy output (bottom panel) per unit stellar mass as functions of  $m_{\max}$ . By allowing  $m_{\max}$  to increase beyond  $100 M_\odot$  and taking into account stellar winds, the IMF-averaged metal yield is enhanced by up to a factor of  $\approx 2.7$  compared with the old model for  $m_{\max} = 100 M_\odot$ . Here, winds contribute  $\sim 5 - 35\%$  of the total metal yield for  $Z \sim 0.004 - 0.014$ . The total energy output from SNe is generally higher in our models by  $\sim 20 - 80\%$  due to the contributions of ECSNe and PPISNe.

Beyond the aforementioned improvements of the metallicity and mass grids, SN types, and wind metal yields from single star evolution, we further implement a phenomenological model for Type Ia SNe following Deng et al. (2024), as detailed in Appendix C. Following Hartwig et al. (2024), the fitting formulae for  $\dot{q}_{\text{ion}}$  and  $t_\star$  are also updated based on Klessen & Glover (2023) to consider more detailed metallicity dependence. The new models are similar to the old ones adopted in Hartwig et al. (2022, see their sec. 2.1.3) in most cases. We have verified by numerical experiments that the updates in  $\dot{q}_{\text{ion}}$  and  $t_\star$  have minor effects on our results, but we plan to improve the treatment of these parameters in future work, based on the results of Lecroq et al. (2024).

### 3. Simulation setup

We apply A-SLOTH to the merger trees constructed from the cosmological simulation by Ishiyama et al. (2016) in a co-moving volume of  $V_{\text{com}} \simeq (8 h^{-1} \text{cMpc})^3 \simeq 1750 \text{cMpc}^3$  with a dark matter mass resolution of  $5000 h^{-1} M_\odot$ . The merger trees span the redshift range  $z \sim 4.5 - 30$  in which the box is marginally large enough to be cosmologically representative. We are particularly interested in the regime  $z \sim 4 - 10$  probed by recent JWST observations. In our simulations, this redshift range is covered by 30 snapshots with global timesteps  $\Delta t_j \sim 17 - 46 \text{ Myr}$ . Our simulation box is rather small as a tradeoff for the high resolution required to capture the first star forming halos ( $M_h \sim 10^6 M_\odot$ ), such that the statistics of the most massive/luminous objects that favor over-dense regions is poor. Therefore, we focus on the scaling relations between galaxy properties and cosmic integrated quantities (e.g., star formation rate density) rather than the distributions of specific galaxy properties (e.g., UV luminosity function and stellar mass function), as discussed in detail below.

**Table 1.** Summary of key free parameters in A-SLOTH. The first section shows the parameters fixed throughout this work based on the best-fit values from Hartwig et al. (2024, see their table 1). The second shows the parameters explored in plausible ranges to reproduce observations of high- $z$  galaxies.

Parameter	Description	Value(s)/range
$m_{\max, \text{III}} [M_\odot]$	Max. mass of Pop III stars	197
$m_{\min, \text{III}} [M_\odot]$	Min. mass of Pop III stars	13.6
$\alpha_{\text{III}}$	Pop III IMF slope	1.77
$\eta_{\text{III}}$	Pop III SFE	8.15
$\eta_{\text{II}}$	Pop II SFE	0.237
$v_{\text{sv}}/\sigma_{\text{sv}}$	Baryon streaming velocity	0.8
$c_{\text{ZIGM}}$	IGM Z clumping factor	3.32
$\alpha_{\text{out}}$	Slope of outflow efficiency	0, 0.5, 1
$M_{\text{out0}} [M_\odot]$	Norm. of outflow efficiency	$[1, 5] \times 10^9$
$m_{\max}$	Max. mass of Pop II stars	$[100, 600]$

Throughout this work, we adopt the cosmological parameters from Planck Collaboration et al. (2016)<sup>19</sup>. The streaming velocity between baryons and dark matter  $v_{\text{sv}}$  is set to the most probable value  $0.8\sigma_{\text{sv}}$ , where  $\sigma_{\text{sv}}$  is the root-mean-square velocity (Schauer et al. 2019). The key free parameters for star formation and feedback are summarized in Table 1. Here, we focus on three parameters that directly regulate metal enrichment of high- $z$  galaxies:  $\alpha_{\text{out}}$ ,  $M_{\text{out0}}$ , and  $m_{\max}$ , while keeping the other parameters fixed to the best-fit values from Hartwig et al. (2024) which are calibrated to reproduce various observations (see their sec. 2.2). We run  $3 \times 5 \times 11 = 165$  simulations in total on the grid defined by  $\alpha_{\text{out}} = 0, 0.5$ , and  $1$ ,  $M_{\text{out0}} \in [1, 5] \times 10^9 M_\odot$  with linear spacing  $\Delta M_{\text{out0}} = 10^9 M_\odot$ , and  $m_{\max} \in [100, 600] M_\odot$  with  $\Delta m_{\max} = 50 M_\odot$ . The values of  $\alpha_{\text{out}}$  and  $M_{\text{out0}}$  considered here differ significantly from those ( $\alpha_{\text{out}} \sim 1.8 - 4$ ,  $M_{\text{out0}} \sim 6 - 11 \times 10^9 M_\odot$ ) preferred by observational constraints found by Hartwig et al. (2024). This is partially due to the updates of star formation and stellar feedback schemes in our work (see Sec. 2.2 and 2.3). With these updates, in principle, a new systematic calibration of all parameters is required, which is beyond the scope of this paper. The main reason for the different choices of  $\alpha_{\text{out}}$  and  $M_{\text{out0}}$  is that our work focuses on observables of galaxies/halos at  $z \gtrsim 4$  (see below), while most (6 out of 9) observables considered by Hartwig et al. (2024) come from the Milky Way at  $z = 0$ . We have found by numerical experiments that the favored values of  $\alpha_{\text{out}}$  and  $M_{\text{out0}}$  in Hartwig et al. (2024) cannot reproduce the high- $z$  observations considered here, even for the old star formation model given maximum metal yields (with  $m_{\max} \sim 250 M_\odot$ ). They generally fail to form enough stars and produce enough metals. This implies that galactic outflow parameters can evolve significantly from  $z \gtrsim 4$  to  $z \sim 0$ , as high- $z$  dwarf galaxies (at least those detected by JWST) are less vulnerable to stellar feedback than their local counterparts due to their compact nature. In fact, it is implied by our simulation results (see Sec. 5.2 and Appendix B) that redshift evolution of outflow parameters at  $z \lesssim 6$  is required to fully reproduce the cosmic star formation history inferred from observations, which favor decreasing outflow efficiency at lower redshifts in relatively massive halos ( $M_h \gtrsim M_{\text{out0}}$ ).

### 4. Observational constraints

We consider observational constraints from three aspects: cosmic star formation history (Sec. 4.1), galaxy chemical evolution (Sec. 4.2), and galaxy-halo connection (Sec. 4.3). Each aspect includes one or two observables, characterized by their likelihoods  $\mathcal{L}_j$ . We define the geometric mean of the likelihoods of individual observables as the likelihood of the aspect. Each observable  $j$  includes several observations (for individual galaxies or redshift bins). Their likelihoods  $\mathcal{L}_i$  are combined with weights  $w_i$  (to be discussed in detail below) to estimate  $\mathcal{L}_j$  as:

$$\log \mathcal{L}_j = \frac{\sum_i w_i \log \mathcal{L}_i}{\sum_i w_i}. \quad (10)$$

Following Hartwig et al. (2024), the likelihood of an observation  $i$  is given by

$$\mathcal{L}_i(x_{\text{obs},i}, \sigma_i, x_{\text{sim},i}) = \frac{1}{\sqrt{2\pi\sigma_i^2}} \exp \left[ -\frac{(x_{\text{obs},i} - x_{\text{sim},i})^2}{2\sigma_i^2} \right], \quad (11)$$

<sup>19</sup>  $\Omega_m = 0.3089$ ,  $\Omega_b = 0.0486$ , and  $H_0 = 100h \text{ km s}^{-1} \text{ Mpc}^{-1}$  with  $h = 0.6774$



where  $x_{\text{obs},i}$  is the observed value,  $x_{\text{sim},i}$  is the simulated value, and  $\sigma_i$  is the uncertainty, assuming that the error  $\Delta x_i \equiv x_{\text{obs},i} - x_{\text{sim},i}$  follows a normal distribution.

The overall likelihood  $\mathcal{L}_{\text{all}}$  is defined as the geometric mean of the likelihoods of individual aspects:

$$\mathcal{L}_{\text{all}} = (\mathcal{L}_{\text{CSFH}} \mathcal{L}_{\text{MZSFR}} \mathcal{L}_{\text{SHMR}})^{1/3}. \quad (12)$$

In the following subsections, we will explain the observables underlying the three terms in this formula and how we derive  $x_{\text{sim},i}$  from simulations and obtain  $x_{\text{obs},i}$  and  $\sigma_i$  from the observational literature. Once  $\mathcal{L}_{\text{all}}$  is known, we search for the ‘best-fit’ model(s) on the grid of  $\alpha_{\text{out}} - M_{\text{out}} - m_{\text{max}}$  that achieve the highest value(s) of  $\mathcal{L}_{\text{all}}$ , as discussed in Sec. 5. This process is analogous to the least-squares method of fitting, as  $-\log \mathcal{L}_{\text{all}}$  is proportional to a weighted sum of the squares of residuals  $(x_{\text{obs},i} - x_{\text{sim},i})^2$  of individual observations thanks to the exponential form of their likelihoods (Eq. 11) and the usage of geometric mean to combine them.

#### 4.1. Cosmic star formation history

The first aspect, cosmic star formation history (CSFH), is described by two observables: star formation rate density (SFRD) and cosmic stellar mass density (CSMD)  $\rho_*$ , such that  $\mathcal{L}_{\text{CSFH}} = \sqrt{\mathcal{L}_{\text{SFRD}} \mathcal{L}_{\text{CSMD}}}$ .

For SFRD, we collect the measurements at 12 redshifts in the range  $z \sim 5 - 16$  based on integration of UV luminosity functions down to magnitude  $M_{\text{UV}} = -17$  (Bouwens et al. 2016; Donnan et al. 2023a,b; Harikane et al. 2023), as listed in Table 2. This is of course not a complete collection of existing SFRD measurements (see also, e.g., Madau & Dickinson 2014; Finkelstein et al. 2015; McLeod et al. 2016; Oesch et al. 2018; Bhatawdekar et al. 2019; Bouwens et al. 2021, 2023; D’Silva et al. 2025). The adopted ones are selected such that they have consistent definitions and delineate a smooth increase of SFRD with decreasing redshift at  $z \gtrsim 5$ . As shown by Donnan et al. (2023a), the evolution at  $z \sim 7.5 - 15$  is well captured by a linear relation between log SFRD and  $z$ :

$$\log(\text{SFRD} [\text{M}_{\odot} \text{yr}^{-1}]) = (-0.231 \pm 0.037)z - 0.439 \pm 0.3, \quad (13)$$

given the canonical conversion factor between SFR and UV luminosity  $L_{\text{UV}}$  from Madau & Dickinson (2014):  $\kappa_{\text{UV}} \equiv \text{SFR}/(\text{M}_{\odot} \text{yr}^{-1})/[L_{\text{UV}}/(\text{erg s}^{-1} \text{Hz}^{-1})] = 1.15 \times 10^{-28}$ . To be consistent with the definition of SFRD in observations, we only consider galaxies with  $\text{SFR} > 10^{-0.5} \text{M}_{\odot} \text{yr}^{-1}$  corresponding to  $M_{\text{UV}} < -17$  according to  $\kappa_{\text{UV}}$ , where the SFR is measured on a timescale of  $t_{\text{SF}} = 10$  Myr. The SFRs of these galaxies are summed up and divided by  $V_{\text{com}}$  to give the ‘instantaneous’ SFRD. Since the UV luminosity of a galaxy typically probes the SFR in a longer timescale  $t_{\text{SF}} \sim 100$  Myr, we further convolve this ‘instantaneous’ SFRD with a time window of 100 Myr to obtain the final simulated SFRD to be compared with observations<sup>20</sup>. We evaluate the likelihood (Eq. 11) in terms of  $x_i \equiv \log(\text{SFRD} [\text{M}_{\odot} \text{yr}^{-1}])$  and interpolate the simulation results linearly to the redshifts of observations. The uncertainty  $\sigma_i$  is set to the observational uncertainty (see Table 2).

To reduce the effects of small-sample statistics, we only consider the redshift bins in which there are at least 3 galaxies with  $\text{SFR} > 10^{-0.5} \text{M}_{\odot} \text{yr}^{-1}$  in the simulation box, and the corresponding likelihoods  $\mathcal{L}_i$  are weighted evenly ( $w_i = 1$ ) to calculate  $\mathcal{L}_{\text{SFRD}}$  by Eq. 10.

**Table 2.** Compilation of SFRD measurements at  $z \sim 5 - 16$ . The first section shows the pre-launch results from HST and ALMA. The second section shows the results from JWST.

$z$	$\log(\text{SFRD} [\text{M}_{\odot} \text{yr}^{-1}])$	Reference
4.9	$-1.387 \pm 0.124$	Bouwens et al. (2016)
5.9	$-1.640 \pm 0.130$	Bouwens et al. (2016)
6.8	$-1.883 \pm 0.076$	Bouwens et al. (2016)
7.9	$-2.213 \pm 0.065$	Bouwens et al. (2016)
8	$-2.31 \pm 0.06$	Donnan et al. (2023a,b)
9	$-2.52^{+0.08}_{-0.10}$	Donnan et al. (2023a,b)
10.5	$-2.80^{+0.13}_{-0.20}$	Donnan et al. (2023a,b)
11.2	$-2.95^{+0.20}_{-0.36}$	Donnan et al. (2023b)
13.25	$-3.62^{+0.16}_{-0.25}$	Donnan et al. (2023a,b)
9	$-2.61^{+0.18}_{-0.16}$	Harikane et al. (2023)
12	$-3.23^{+0.29}_{-0.27}$	Harikane et al. (2023)
16	$-3.59^{+0.33}_{-2.83}$	Harikane et al. (2023)

For CSMD, we adopt the results at  $z \sim 6 - 12$  from the empirical model in Donnan et al. (2025, see their fig. 7 and the references therein), derived by integrating the galaxy stellar mass function over the mass range  $10^8 - 10^{13} \text{M}_{\odot}$ . This model captures the median value among various literature results (see also fig. 4 in Bosi et al. 2025) and can be described by the fit:

$$\log(\rho_* [\text{M}_{\odot} \text{cMpc}^{-3}]) = -0.195z - 0.022z^2 + 8.728. \quad (14)$$

The discrepancy between different CSMD measurements and their largest uncertainty are around 0.5 dex. Therefore, we define the CSMD likelihood with  $x_i \equiv \log(\rho_* [\text{M}_{\odot} \text{cMpc}^{-3}])$  and adopt a constant uncertainty  $\sigma_i = 0.5$  dex. To be consistent with the observed galaxy sample, we only consider galaxies with  $M_* > 10^8 \text{M}_{\odot}$  to derive the simulated CSMD for comparison. Similar to the case of SFRD, we combine the likelihoods of simulation redshift bins within  $z \in [6, 12]$  that have at least 3 galaxies with  $M_* > 10^8 \text{M}_{\odot}$  using equal weights in Eq. 10 for  $\mathcal{L}_{\text{CSMD}}$ .

#### 4.2. Galaxy chemical evolution

High- $z$  galaxies are unresolved point sources in our approach, their overall chemical evolution is captured by the relation between stellar mass  $M_*$ , SFR, and metallicity  $Z$ . Recent observations by JWST have measured these properties of a few hundred galaxies at  $z \sim 4 - 10$  (Langeroodi et al. 2023; Heintz et al. 2023; Nakajima et al. 2023; Chakraborty et al. 2024; Curti et al. 2024; Li et al. 2025; Rowland et al. 2025; Sarkar et al. 2025). In particular, the results from spectroscopy programs of ERO, GLASS, CEERS, JADES, and the JWST-PRIMAL Legacy Survey (Nakajima et al. 2023; Curti et al. 2024; Sarkar et al. 2025) have reached a consensus that there is a universal  $M_*$ - $Z$ -SFR relation (MZSFR) at  $z \sim 4 - 8$  consistent with that observed at  $z \lesssim 3$  (Andrews & Martini 2013). This relation is also found to hold at  $z \sim 6 - 8$  by the REBELS ALMA large program (Rowland et al. 2025). On the other hand, the relation tends to break down at higher redshifts where galaxies are systematically more metal-poor (by  $\sim 0.27$  dex, Sarkar et al. 2025). Considering that the samples of both observed and simulated galaxies are small at  $z \gtrsim 8$ , we focus on the JWST-concordance (invariant) relation

<sup>20</sup> These considerations highlight the importance of proper comparison between simulations and observations. The SFRD in simulations is usually measured in simulation timesteps and includes the contributions of all galaxies, like in Hartwig et al. (2024). However, this is often not directly comparable to the SFRD inferred from observations with SFR tracers at different timescales and incomplete samples of faint objects.

at  $z \sim 4 - 8$  to search for the best-fit model. The systematic decrease of metallicity at  $z \sim 8 - 10$  is used for cross-validation. The underlying galaxy sample of Nakajima et al. (2023), Curti et al. (2024), and Sarkar et al. (2025) is referred to as the JWST galaxies henceforth.

In these observations, the SFR is typically derived from the  $H\beta$  line luminosity (except for JADES, which uses spectral fitting) as a good indicator for ongoing ( $\sim 10$  Myr) star formation. Note that the SFR of simulated galaxies is calculated on a short timescale of  $t_{\text{SF}} = 10$  Myr consistent with that of the SFR indicator in observations, which ensures fair comparison. Besides, our analysis only includes simulated galaxies with  $\text{SFR} \gtrsim 10^{-0.5} M_{\odot} \text{ yr}^{-1}$  to be consistent with the observed sample. Note that high- $z$  observations tend to be biased by luminous objects, especially when compared with simulations in a much smaller volume. One could apply a more complicated treatment for incompleteness and cosmic variance. As an exploratory approach, we instead apply a simple SFR cut and make corrections for observational biases when necessary by comparing the median values of SFR from the simulated and observed galaxies (see below). The observed (gas-phase) metallicity of a galaxy is characterized by the absolute oxygen abundance,  $\log(\text{O}/\text{H}) + 12$ , measured via nebular emission lines from star-forming regions. Considering that these lines are mostly powered by young massive stars, we define the metallicity of a simulated galaxy as the mass-weighted average oxygen abundance of massive stars ( $m_{\star} > 5 M_{\odot}$ ) with ages less than 10 Myr. We further normalize the metallicity by the solar value and thus consider  $[\text{O}/\text{H}] \equiv \log(\text{O}/\text{H}) + 12 - 8.69$ , which turns out to be a good tracer of the bulk metallicity<sup>21</sup>, i.e.,  $[\text{O}/\text{H}] \simeq \log(Z/Z_{\odot})$ .

To fully extract information from observations, we look into the observed invariant MZSFR in two ways: the fundamental metallicity relation (FMR) and stellar mass-metallicity relation (MZR), such that  $\mathcal{L}_{\text{MZSFR}} = \sqrt{\mathcal{L}_{\text{FMR}} \mathcal{L}_{\text{MZR}}}$ . The former, originally based on  $z \lesssim 3$  observations (Andrews & Martini 2013), can be written as:

$$[\text{O}/\text{H}]_{\text{FMR}}(\mu_{\alpha}) = 0.43\mu_{\alpha} - 4.11, \quad \alpha = 0.66, \quad (15)$$

where  $\mu_{\alpha} \equiv \log(M_{\star} [M_{\odot}]) - \alpha \log(\text{SFR} [M_{\odot} \text{ yr}^{-1}])$ , and  $\alpha = 0.66$  is chosen to minimize the scatter in  $[\text{O}/\text{H}]$  at a given  $\mu_{\alpha}$  down to  $\sigma_{\text{FMR}} = 0.013$  dex. To derive the likelihood  $\mathcal{L}_{\text{FMR}}$ , we apply Eq. 10 to all galaxies with  $\text{SFR} > 10^{-0.5} M_{\odot} \text{ yr}^{-1}$  from the redshift bins within  $z \sim 4 - 8$ . All galaxies from a redshift bin  $j$  are assigned with the same weight as the co-moving volume of the corresponding shell in the lightcone for an observer at  $z = 0$ , i.e.,  $w_i = 4\pi \int_{z_j}^{z_{j+1}} D_C^2(z) |dD_C/dz| dz$ , where  $D_C(z)$  is the co-moving distance. For each simulated galaxy, the likelihood (Eq. 11) is calculated from the predicted metallicity  $x_{\text{sim},i} = [\text{O}/\text{H}]_{\text{sim}}$  and that expected from the FMR  $x_{\text{obs},i} = [\text{O}/\text{H}]_{\text{FMR}}(\mu_{0.66,\text{sim}})$  given  $\sigma_i = \sigma_{\text{FMR}} = 0.013$  dex, where  $\mu_{0.66,\text{sim}}$  is derived from the simulated SFR and  $M_{\star}$ . Here, we adopt  $\sigma_i = \sigma_{\text{FMR}} = 0.013$  dex as an optimistic assumption for the tightness of FMR. In fact, we estimate the scatter of JWST galaxies at  $z \sim 4 - 10$  (Sarkar et al. 2025, see their fig. 6) around the invariant FMR (Eq. 15) as  $\sigma_{\text{FMR,JWST}} \simeq 0.27$  dex, much larger than the value at  $z \lesssim 3$ . Considering potentially large uncertainties in the measurements of SFR,  $M_{\star}$ , and  $[\text{O}/\text{H}]$  in high- $z$  observations, the intrinsic scatter will be smaller and closer to the low- $z$  value.

For MZR, we consider the results from Sarkar et al. (2025, see their table 1) for two observational redshift bins:

$$[\text{O}/\text{H}]_{\text{MZR}} = \begin{cases} 0.28 \log(M_{\star} [M_{\odot}]) - 3.12, & z \sim 4 - 6, \\ 0.23 \log(M_{\star} [M_{\odot}]) - 2.70, & z \sim 6 - 8, \end{cases} \quad (16)$$

which are consistent with the earlier results of Nakajima et al. (2023) and Curti et al. (2024). We take the uncertainty/scatter in  $[\text{O}/\text{H}]$  from Nakajima et al. (2023) as  $\sigma_{\text{MZR}} = 0.28$  and  $0.23$  dex for  $z \sim 4 - 6$  and  $z \sim 6 - 8$ , respectively. Individual simulated galaxies (with  $\text{SFR} > 10^{-0.5} M_{\odot} \text{ yr}^{-1}$ ) are weighted in the same manner as for FMR to first calculate the likelihood  $\mathcal{L}_{\text{MZR},[z_{\text{low}},z_{\text{up}}]}$  of each observational redshift bin  $[z_{\text{low}}, z_{\text{up}}]$  by Eq. 10. The final likelihood is given by  $\log \mathcal{L}_{\text{MZR}} = (W_{[4,6]} \log \mathcal{L}_{\text{MZR},[4,6]} + W_{[6,8]} \log \mathcal{L}_{\text{MZR},[6,8]}) / (W_{[4,6]} + W_{[6,8]})$ , where  $W_{[z_{\text{low}},z_{\text{up}}]} = \sum_i w_i$  is the sum of weights for galaxies within  $z_i \in [z_{\text{low}}, z_{\text{up}}]$ .

We further apply a correction to the original observed MZR in Eq. 16, considering the fact that observations (of metal lines) are biased by luminous galaxies with systematically higher SFR (and therefore more metal-poor) than the simulated galaxies in our small simulation volume. The median log SFR of observed galaxies at a given stellar mass is typically larger than that of our simulated galaxies by  $\Delta \log \text{SFR} \sim 0.6$  dex, as shown in Appendix A. Assuming that the FMR (Eq. 15) holds, reducing the median SFR by  $\Delta \log \text{SFR}$  will cause an increase of metallicity in MZR by  $\Delta[\text{O}/\text{H}]_{\text{MZR}} = 0.43 \times 0.66 \times \Delta \log \text{SFR} \sim 0.16$  dex. In light of this, we define  $x_{\text{obs},i} = [\text{O}/\text{H}]_{\text{MZR}}(M_{\star,\text{sim}}) + \Delta[\text{O}/\text{H}]_{\text{MZR}}$  to calculate the likelihood (Eq. 11) of a simulated galaxy using  $\sigma_i = \sigma_{\text{MZR}}$ , given the simulated stellar mass  $M_{\star,\text{sim}}$  and metallicity  $x_{\text{sim},i} = [\text{O}/\text{H}]_{\text{sim}}$ . In this way, we find that the constraints from FMR and MZR are generally consistent with each other.

Whether the invariant FMR (Eq. 15) better describes the galaxy chemical evolution than MZR beyond the local Universe ( $z \sim 0$ ) is still in debate. For instance, it is shown by Korhonen Cuestas et al. (2025) that for galaxies from the Keck Baryonic Structure Survey at  $z \sim 2.3$ , introducing SFR to the metal scaling relation via  $\mu_{\alpha}$  hardly reduces the scatter in  $[\text{O}/\text{H}]$ , and the anticorrelation between SFR and the residual of  $[\text{O}/\text{H}]$  from MZR is very weak (weaker than that implied by the invariant FMR). This is consistent with the large scatter of JWST galaxies at  $z \sim 4 - 10$  around the invariant FMR  $\sigma_{\text{FMR,JWST}} \simeq 0.27$  dex, which is comparable to the scatter in MZR  $\sigma_{\text{MZR}} \sim 0.23 - 0.28$  dex. We also notice that there is a small systematic offset  $\Delta[\text{O}/\text{H}]_{\text{FMR}} \sim -0.07$  dex between the JWST galaxies of Sarkar et al. (2025) and the invariant FMR (see also fig. 11 in Korhonen Cuestas et al. 2025). We can approximately incorporate these effects into our analysis by applying a correction of  $\Delta[\text{O}/\text{H}]_{\text{FMR}} \sim -0.07$  dex to the FMR at  $z \sim 4 - 8$ , a larger FMR scatter of  $\sigma_{\text{FMR,JWST}} \sim 0.27$  dex, and a smaller correction for MZR of  $\Delta[\text{O}/\text{H}]_{\text{MZR}} \sim 0.1$  dex. Doing so does not change our conclusions according to numerical experiments.

### 4.3. Galaxy-halo connection

The last aspect, i.e., the galaxy-halo connection, is relatively more difficult to probe in observations and, therefore, is expected to have weaker constraining power compared with the two aspects above. Since it is directly related to the underlying halo merger trees – backbones of our simulations, we still take it into account for completeness, focusing on the stellar-halo mass relation (SMHR). This relation is normally derived from semi-empirical models based on abundance matching (e.g., Tacchella et al. 2018; Behroozi et al. 2019; Stefanon et al. 2021; Zaritsky & Behroozi 2023) whose results still show large discrepancies

<sup>21</sup> In our simulations, the difference between  $\log(Z/Z_{\odot})$  and  $[\text{O}/\text{H}]$  is typically  $\sim 0.03 - 0.07$  dex and remains below  $0.15$  dex for galaxies with  $M_{\star} \gtrsim 10^7 M_{\odot}$  and  $\text{SFR} \gtrsim 0.03 M_{\odot} \text{ yr}^{-1}$  at  $z \gtrsim 4$  that are covered by existing JWST spectroscopy surveys.

up to  $\sim 1$  dex at  $z \sim 4 - 10$  (see Sec. 5.2). Here, we choose the results of Tacchella et al. (2018) as our target since they appear to be the ‘median’ case, which can be described by the fit formula for  $M_{\star, \text{SHMR}}(M_h, z)$  in Eq. 3. The scatter around this relation is found to be around 0.14 – 0.18 dex by Tacchella et al. (2018). Considering the large discrepancies among different models, we instead use a larger uncertainty in  $\log M_{\star}$  as  $\sigma_{\text{SHMR}} = 0.31$  based on observations of local dwarf galaxies (Zaritsky & Behroozi 2023).

Similar to the case of MZR, we focus on galaxies with  $\text{SFR} > 10^{-0.5} M_{\odot} \text{ yr}^{-1}$  which are divided into two redshift bins for  $z \sim 4 - 6$  and  $z \sim 6 - 8$  where the likelihoods are calculated separately and then combined to give  $\log \mathcal{L}_{\text{SHMR}} = (W_{[4,6]} \log \mathcal{L}_{\text{SHMR}, [4,6]} + W_{[6,8]} \log \mathcal{L}_{\text{SHMR}, [6,8]}) / (W_{[4,6]} + W_{[6,8]})$ . The likelihood of a simulated galaxy  $i$  at the simulation redshift bin  $z_j$  is derived using Eq. 11 with  $x_{\text{obs}, i} = \log(M_{\star, \text{SHMR}}(M_{\text{vir}, \text{sim}}, z_j) [M_{\odot}])$ ,  $x_{\text{sim}, i} = \log(M_{\star, \text{sim}} [M_{\odot}])$ , and  $\sigma_i = \sigma_{\text{SHMR}} = 0.31$  given its stellar mass  $M_{\star, \text{sim}}$  and halo mass  $M_{\text{vir}, \text{sim}}$ .

## 5. Results

In this section, we present our simulation results in the context of the observational constraints described in the previous section. We first show the overall likelihood  $\mathcal{L}_{\text{all}}$  as a function of model parameters  $\alpha_{\text{out}}$ ,  $M_{\text{out}0}$ , and  $m_{\text{max}}$  and evaluate the contributions of individual observational constraints to understand the interplay between IMF and galactic outflow parameters on star formation and chemical evolution of high- $z$  galaxies (Sec. 5.1). Next, we focus on the best-fit model with the highest  $\mathcal{L}_{\text{all}}$  for which we compare theoretical predictions with observed quantities/scaling relations in detail to show how well observations can be reproduced by our model and what can be learned about the underlying physics (Sec. 5.2).

### 5.1. Interplay between IMF and galactic outflow parameters

In Fig. 4, we plot  $\log \mathcal{L}_{\text{all}}$  as a function of  $m_{\text{max}}$  under different values of the galactic outflow parameters (see Eqs. 6-7):  $M_{\text{out}0}$  (with different line colors) and  $\alpha_{\text{out}}$  (in separate panels). Similar plots for the likelihoods of CSFH (Sec. 4.1), MZSFR (Sec. 4.2), and SHMR (see Eq. 3 and Sec. 4.3) are shown in Figs. 5, 6, and 7, respectively. We fix  $\alpha_{\text{out}}$  and identify the best-fit models for individual (combinations of) observational constraints considering four cases: (1) CSFH alone, where  $\mathcal{L}_{\text{CSFH}}$  is maximized, (2) MZSFR alone, where  $\mathcal{L}_{\text{MZSFR}}$  is maximized, (3) CSFH+MZSFR, where  $\sqrt{\mathcal{L}_{\text{CSFH}} \mathcal{L}_{\text{MZSFR}}}$  is maximized, and finally (4) all (CSFH+MZSFR+SHMR) combined, where  $\mathcal{L}_{\text{all}}$  is maximized, as labeled by the triangles, squares, diamonds, and crosses in Figs. 4-7. We also estimate the likelihood values corresponding to  $k\sigma$  ( $k = 1, 2$ , and  $3$ ) deviation between simulation results and observations by substituting  $\Delta x = x_{\text{sim}, i} - x_{\text{obs}, i} = k\sigma_i$  in Eq. 11.

Given an outflow efficiency slope  $\alpha_{\text{out}} = 0$ , the four best-fit models are generally consistent with each other with  $M_{\text{out}0} \sim 2 - 3 \times 10^9 M_{\odot}$ , and  $m_{\text{max}} \sim 200 - 300 M_{\odot}$ . However, this is not the case for  $\alpha_{\text{out}} = 0.5$  and 1, which shows a (mild) tension between the requirements for reproducing the observed CSFH and MZSFR. To be specific, when MZSFR is taken into account in cases (2), (3), (4),  $m_{\text{max}} \sim 200 - 450 M_{\odot}$  is favored, while for case (1), CSFH alone, the best-fit model has  $m_{\text{max}} = 100 M_{\odot}$ , and the corresponding  $M_{\text{out}0}$  is also higher. It is shown in Fig. 6 that the observed MZSFR itself is always best reproduced by  $m_{\text{max}} \sim 200 - 300 M_{\odot}$  regardless of the choices of  $M_{\text{out}0}$  and  $\alpha_{\text{out}}$ , because such IMFs provide maximum metal yields (see Fig. 3).

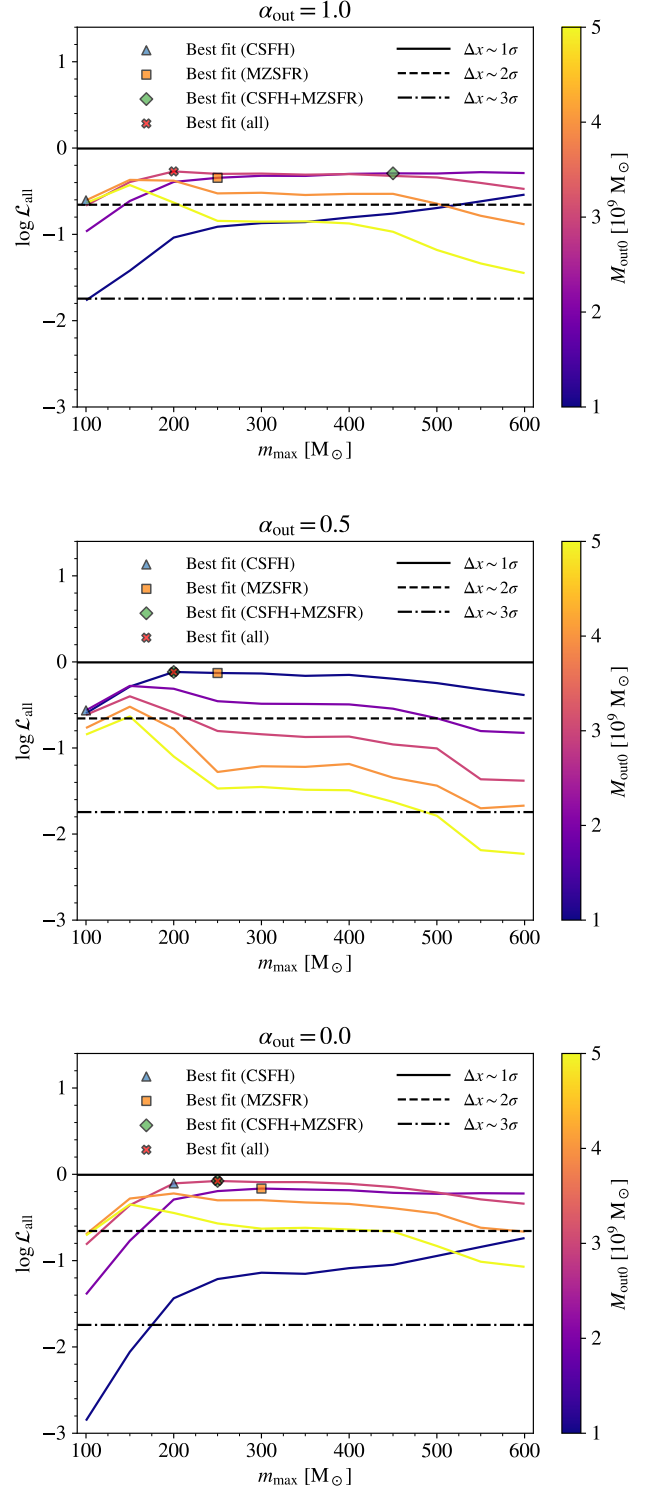


**Fig. 4.** The overall likelihood  $\mathcal{L}_{\text{all}}$  (Eq. 12) combining all observational constraints (CSFH+MZSFR+SHMR) as a function of  $m_{\text{max}}$  (x-axis) and  $M_{\text{out}0}$  (colorbar). The variation of  $\mathcal{L}_{\text{all}}$  with  $m_{\text{max}}$  is shown by lines color-coded by  $M_{\text{out}0}$  where darker colors correspond to smaller  $M_{\text{out}0}$ . The top, middle, and bottom panels show the results for  $\alpha_{\text{out}} = 1.0, 0.5$ , and  $0$ , respectively. The data points mark the best-match models considering 4 combinations of constraints: CSFH alone (triangle), MZSFR alone (square), CSFH+MZSFR (diamond), and all (cross). The solid, dashed, and dash-dotted horizontal lines show the estimated likelihood values for  $1, 2$ , and  $3\sigma$  deviations, respectively.

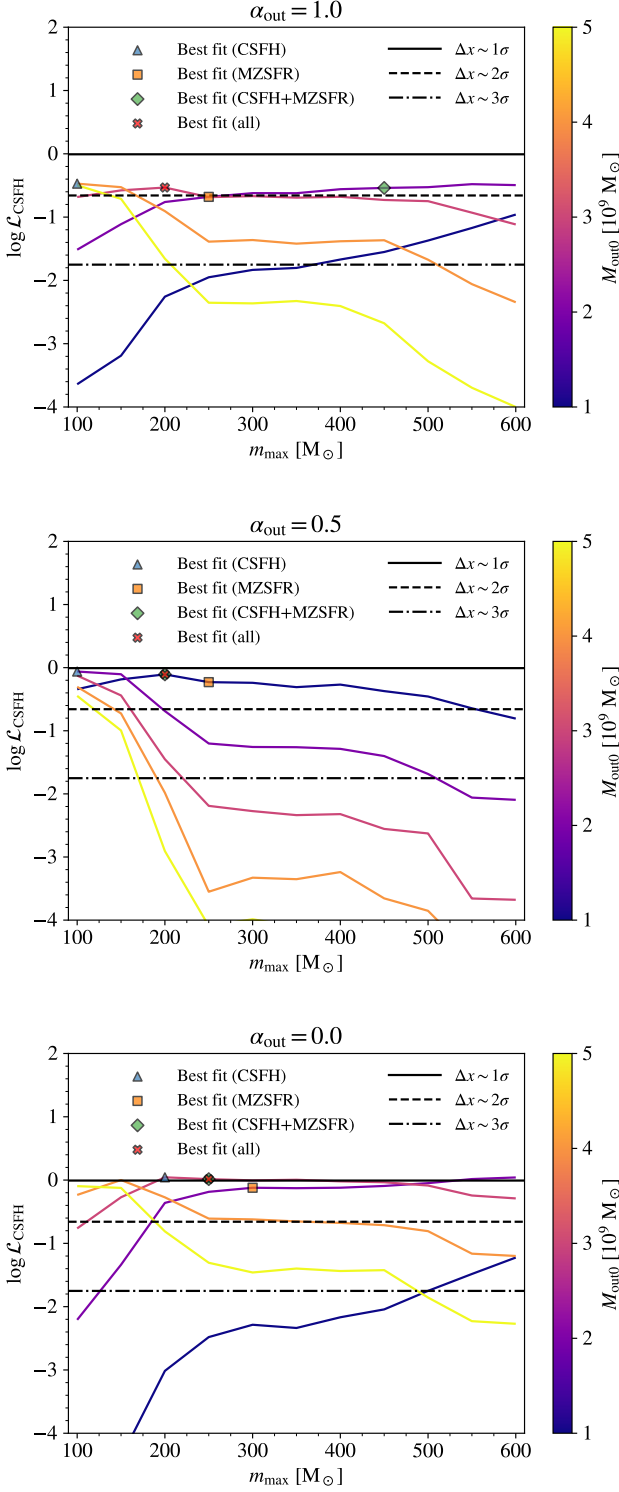


**Fig. 5.** Same as Fig. 4 but for the likelihood of CSFH alone.

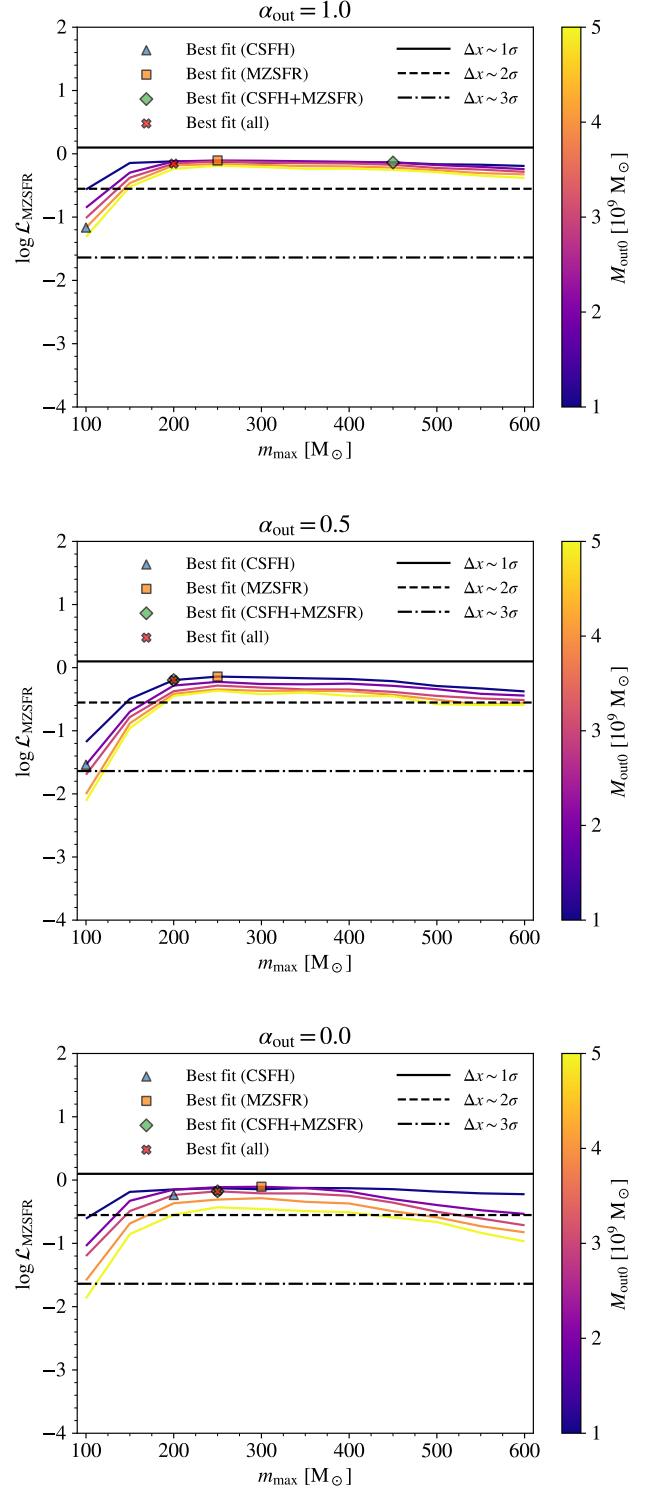


**Fig. 6.** Same as Fig. 4 but for the likelihood of MZSFR alone.

For a given  $m_{\text{max}}$ , smaller  $M_{\text{out}0}$  is generally preferred although the trend is weak/unclear at  $M_{\text{out}0} \lesssim 3 \times 10^9 M_{\odot}$  for  $\alpha_{\text{out}} = 1$  and 0. The maximum of  $\mathcal{L}_{\text{MZSFR}}$  is similar for different values of  $\alpha_{\text{out}}$ .

On the other hand,  $\mathcal{L}_{\text{CSFH}}$  shows more complex dependence on model parameters: For a given  $\alpha_{\text{out}}$ , multiple combinations of  $m_{\text{max}}$  and  $M_{\text{out}0}$  can achieve the highest values of  $\mathcal{L}_{\text{CSFH}}$ . The reason is that the strength of galactic outflows is boosted by in-

creasing either  $m_{\text{max}}$  (for  $m_{\text{max}} \sim 100 - 250 M_{\odot}$ ) or  $M_{\text{out}0}$  (see Fig. 3 and Eq. 6). Meanwhile, it is reduced by decreasing  $\alpha$  for relatively massive halos with  $M_{\text{h}} \gtrsim M_{\text{out}0}$ , which dominate cosmic star formation at  $z \lesssim 8$  in our simulations. Stronger outflows suppress star formation and also reduce the fraction of metals retained in galaxies (see Eq. 5). It turns out that the observed MZSFR requires the highest metal yields and the weakest outflows covered by our simulations. The observed CSFH instead



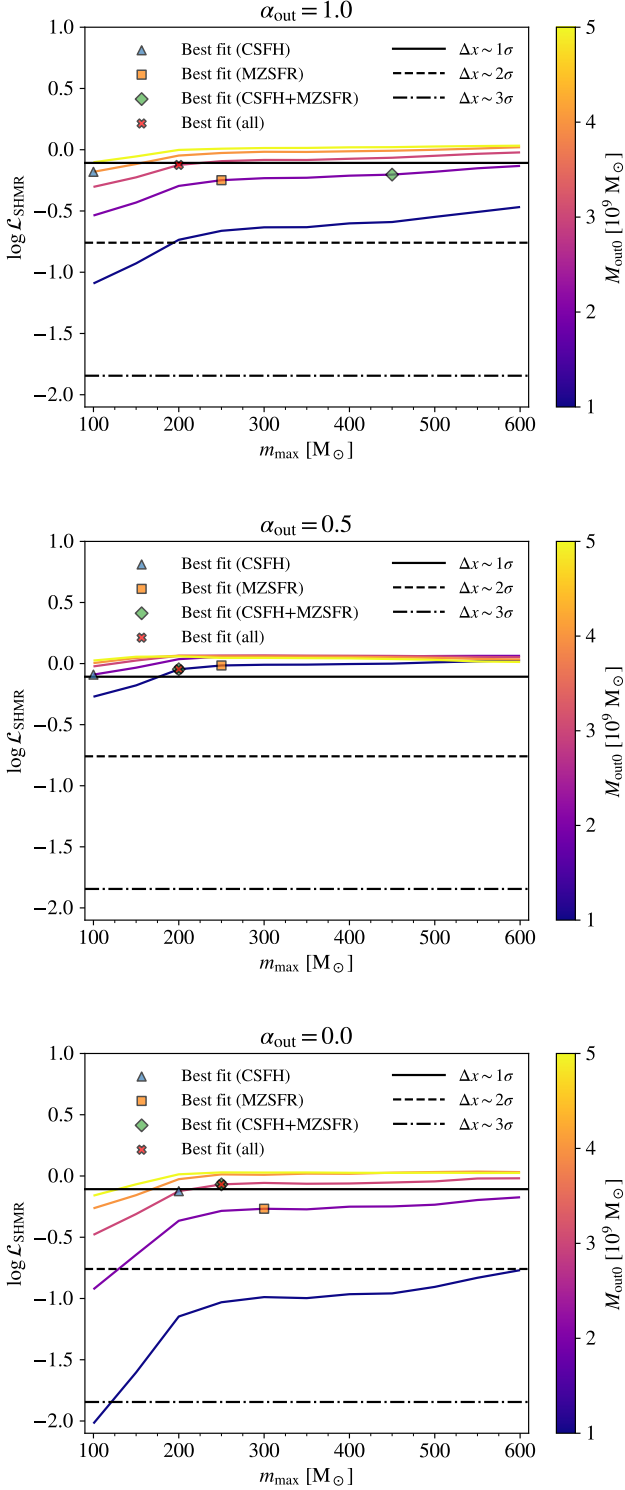


**Fig. 7.** Same as Fig. 4 but for the likelihood of SHMR alone.

prefers some intermediate outflow efficiency. Besides, the maximum of  $\mathcal{L}_{\text{CSFH}}$  is slightly (significantly) higher for  $\alpha_{\text{out}} = 0$  than for  $\alpha_{\text{out}} = 0.5$  (1). In the latter case, the minimum discrepancy between simulations and observations can be up to  $2\sigma$ . This results from the fact that the outflow efficiency is suppressed at  $M_{\text{h}} \gtrsim M_{\text{out0}}$  by Eq. 6 given  $\alpha_{\text{out}} > 0$ , such that the rise of SFRD with decreasing redshift is too rapid compared with observations at  $z \sim 6 - 13$  (see Appendix B). Therefore,  $\alpha_{\text{out}} = 0$  is favored

by the observed CSFH and all constraints are combined as well, so the best-fit model among all simulations has  $\log \mathcal{L}_{\text{all}} \simeq -0.08$  with  $\alpha_{\text{out}} = 0$ ,  $M_{\text{out0}} = 3 \times 10^9 M_{\odot}$ , and  $m_{\text{max}} = 250 M_{\odot}$ . The best-fit model for  $\alpha_{\text{out}} = 0.5$  (1) has  $\log \mathcal{L}_{\text{all}} \simeq -0.12$  ( $-0.27$ ),  $M_{\text{out0}} = 1$  ( $3$ )  $\times 10^9 M_{\odot}$ , and  $m_{\text{max}} = 200 M_{\odot}$ . All these models agree with observations within  $2\sigma$  ( $\log \mathcal{L}_{\text{all}} \sim -0.6$ ), and the best-fit model almost achieves  $1\sigma$  agreement ( $\log \mathcal{L}_{\text{all}} \sim 0$ ).

The constraints from SHMR have minor impact on  $\mathcal{L}_{\text{all}}$ , as the best-fit models for CSFH+MZSFR and all (CSFH+MZSFR+SHMR) are identical for  $\alpha_{\text{out}} = 0$  and  $0.5$ . For  $\alpha_{\text{out}} = 1$ , the best-fit models are different but the corresponding values of  $\mathcal{L}_{\text{all}}$  are very similar. It is shown in Fig. 7 that  $\mathcal{L}_{\text{SHMR}}$  favors  $m_{\text{max}} \gtrsim 200 M_{\odot}$  like  $\mathcal{L}_{\text{MZSFR}}$ . However,  $\mathcal{L}_{\text{SHMR}}$  is generally larger for increasing  $M_{\text{out0}}$ , in contrast to the case of  $\mathcal{L}_{\text{MZSFR}}$ . Moreover, the models preferred by the target SHMR (Eq. 3) from Tacchella et al. (2018) with  $M_{\text{out0}} \sim 4 - 5 \times 10^9 M_{\odot}$  and  $m_{\text{max}} \gtrsim 200 M_{\odot}$  have already been ruled out by the observed CSFH by  $\gtrsim 3\sigma$ . As a result, our best-fit models do not achieve the maximum possible value of  $\mathcal{L}_{\text{SHMR}}$ . It will be shown below that the stellar mass predicted by our simulations at a given halo mass is larger than expected from most empirical models of SHMR in the literature. As mentioned in Sec. 4.3, the SHMR inferred from observations is highly uncertain and model-dependent. So, the seeming tension between the constraints from SHMR and CSFH(+MZSFR) does not necessarily mean a failure of our simulations.

## 5.2. Best-fit model

The likelihood analysis in the previous subsection defines the best-fit model *among all simulations* as  $\alpha_{\text{out}} = 0$ ,  $M_{\text{out0}} = 3 \times 10^9 M_{\odot}$ , and  $m_{\text{max}} = 250 M_{\odot}$ . Here, we assess the consistency of the predictions of this particular model (referred to as ‘our simulation’) with observations, and highlight its distinct features compared with the other runs. In the left panel of Fig. 8, we plot the SFRD of simulated galaxies above different SFR thresholds on top of the observational data summarized in Table 2. In particular, the solid curve shows the SFRD of *detectable* galaxies with  $\text{SFR} > 10^{-0.5} M_{\odot} \text{ yr}^{-1}$  corresponding to the UV magnitude limit  $M_{\text{UV}} \lesssim -17$  in current observations. For these galaxies, our predictions are excellently consistent with observations within  $\lesssim 1\sigma$  at  $z \sim 6 - 13$ . The SFRD measurement from Harikane et al. (2023) at  $z \sim 16$ , which is highly uncertain anyway, is not reproduced, likely due to our limited simulation volume. The SFRD at  $z \sim 5$  is underpredicted by a factor of  $\sim 2$ . It is discussed in Appendix B that this discrepancy can be avoided if we use  $\alpha_{\text{out}} \sim 0.5$  and  $M_{\text{out0}} \sim 3 \times 10^9 M_{\odot}$  at  $z \lesssim 6$ . On the other hand, the total SFRD is larger than that of such detectable galaxies, as fainter ( $M_{\text{UV}} \gtrsim -17$ ) galaxies become more important at higher redshifts. In fact, simulated galaxies with  $\text{SFR} < 10^{-0.5} M_{\odot} \text{ yr}^{-1}$  comprise  $\gtrsim 90\%$  of the total SFRD at  $z \gtrsim 12$ , whose contribution is still significant ( $\sim 30 - 50\%$ ) approaching the end of reionization ( $z \sim 5 - 7$ ). This is in line with the observational evidence for an unseen population of faint galaxies around [OIII] emitters in ionized bubbles at  $z \sim 6$  (Kakiichi et al. 2025). Such faint galaxies could be the main driver of reionization (e.g., Atek et al. 2024)<sup>22</sup> and also make significant contributions to the merger rate density of binary black

<sup>22</sup> This tends to worsen the so-called photon budget crisis in recent semi-analytical/numerical models of reionization, which find that galaxies with  $M_{\text{UV}} \lesssim -15$  can produce (more than) enough ionizing photons required to complete reionization by  $z \sim 6$ , and that observations tend to favor a late start of reionization (e.g., Simmonds et al. 2024; Muñoz et al. 2024; Cain et al. 2025; Sims et al. 2025). However,

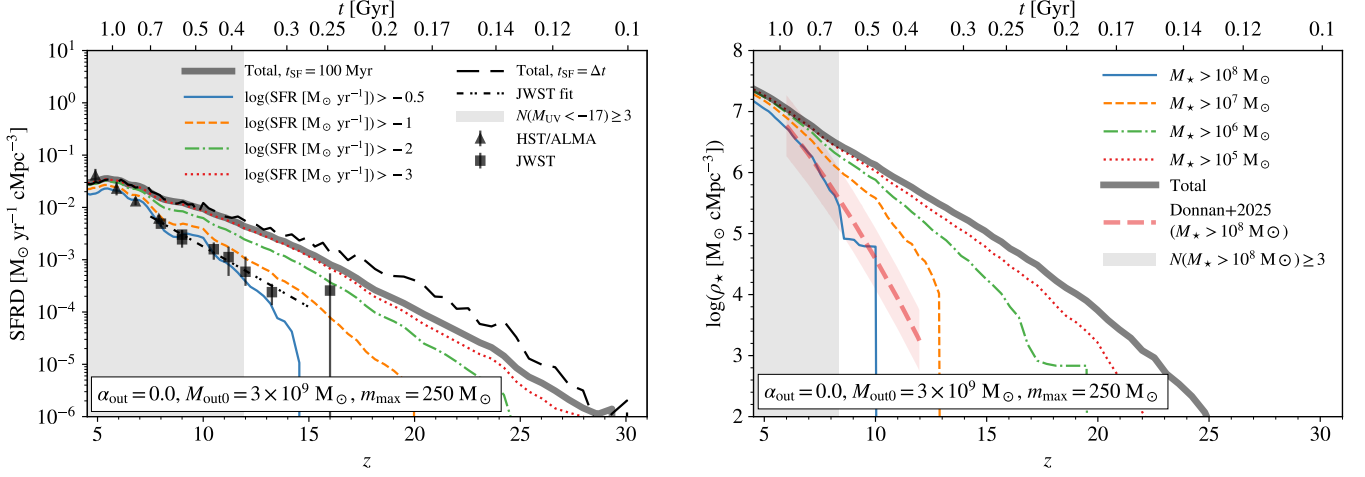


**Fig. 8.** SFRD (left) and CSMD (right) in our simulation for the best-fit model with  $\alpha_{\text{out}} = 0$ ,  $M_{\text{out}0} = 3 \times 10^9 M_{\odot}$ , and  $m_{\text{max}} = 250 M_{\odot}$ . In the left panel, the thick solid curve shows the total SFRD measured on a timescale of  $t_{\text{SF}} = 100$  Myr, while the solid, dashed, dash-dotted, and dotted curves show the contributions from galaxies with  $\log(\text{SFR} [M_{\odot} \text{ yr}^{-1}]) > -0.5$ ,  $-1$ ,  $-2$ , and  $-3$ , respectively. The curve for  $\log(\text{SFR} [M_{\odot} \text{ yr}^{-1}]) > -0.5$  should be compared with the observational results from HST/ALMA and JWST (for luminous galaxies with  $M_{\text{UV}} < -17$ ) embodied by the triangles and squares (see Table 2). The JWST results satisfy a linear relation between  $\log \text{SFR}$  and  $z$  (Eq. 13) at  $z \sim 7.5 - 15$  (dot-dash-dotted). The long dashed curve shows the total SFRD measured in simulation timesteps. In the right panel, the thick solid curve shows the total CSMD, while the solid, dashed, dash-dotted, and dotted curves show the contributions from galaxies with  $M_{\star} > 10^8$ ,  $10^7$ ,  $10^6$ , and  $10^5 M_{\odot}$ , respectively. The curve for  $M_{\star} > 10^8 M_{\odot}$  should be compared with the observational results from Donnan et al. (2025) shown as the thick dashed curve (see Eq. 14) surrounded by the rose shaded region for  $1\sigma$  scatter. The left shaded region shows the redshift range in which comparison between simulations and observations is conducted. This means that there are at least 3 galaxies in the simulation box with  $\log(\text{SFR} [M_{\odot} \text{ yr}^{-1}]) > -0.5$  for SFRD (left), and with  $M_{\star} > 10^8 M_{\odot}$  for CSMD (right).

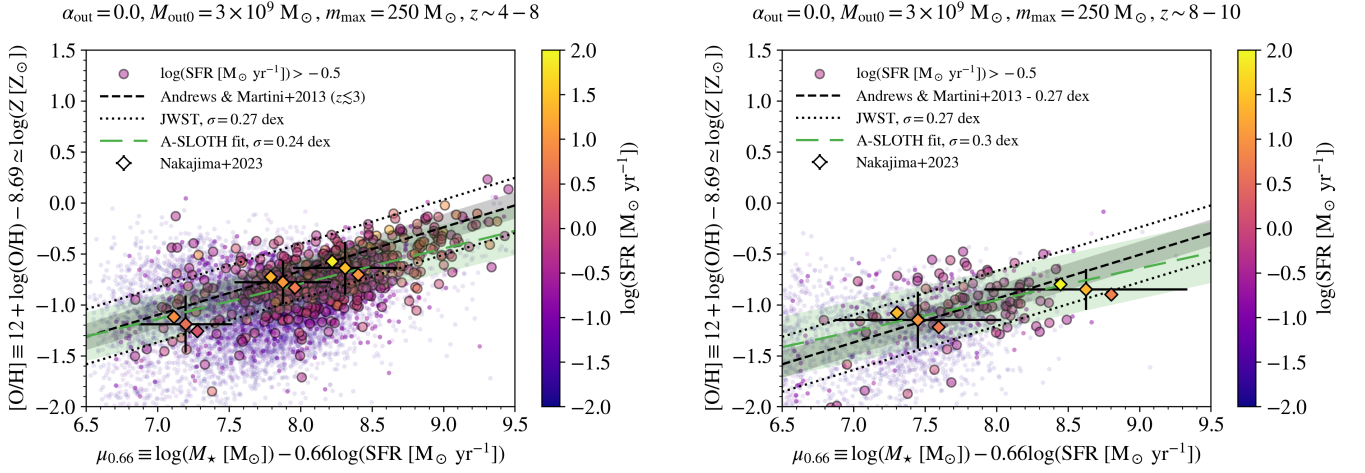


**Fig. 9.** FMR for the best-fit model with  $\alpha_{\text{out}} = 0$ ,  $M_{\text{out}0} = 3 \times 10^9 M_{\odot}$ , and  $m_{\text{max}} = 250 M_{\odot}$ . Simulated galaxies with  $\log(\text{SFR} [M_{\odot} \text{ yr}^{-1}]) > -2$  are shown as dots, color-coded by SFR. The detectable ones with  $\log(\text{SFR} [M_{\odot} \text{ yr}^{-1}]) > -0.5$  are highlighted by large circles, based on which we derive a linear fit (in log-log space) as the long dashed line and green shaded region (for  $1\sigma$  scatter). The left panel shows the results for  $z \sim 4 - 8$ , where observed galaxies follow the same FMR (Eq. 15) found at  $z \lesssim 3$  by Andrews & Martini (2013), as shown by the dashed line. The gray shaded region around it shows the ( $1\sigma$ ) scatter (0.13 dex) reported by Andrews & Martini (2013), while the dotted lines show the scatter (0.27 dex) derived from the JWST galaxies at  $z \sim 4 - 10$  compiled by Sarkar et al. (2025, see their fig. 6). The right panel shows the results for  $z \sim 8 - 10$ . Here, the normalization of FMR is shifted down by 0.27 dex compared with that at  $z \lesssim 8$  according to JWST observations (Sarkar et al. 2025). The shifted observational FMR is again shown by the dashed line. The average values of  $\mu_{0.66}$ ,  $[\text{O}/\text{H}]$ , and SFR of the JWST galaxies of Nakajima et al. (2023, see their table 2) are shown with the diamonds. Each data point involves three diamonds color-coded by the mean and  $1\sigma$  upper and lower limits of SFR. The relevant uncertainties in  $\mu_{0.66}$  and  $[\text{O}/\text{H}]$  are shown by the errorbars.

holes with their metal-poor ( $Z \lesssim 0.1 Z_{\odot}$ ) stellar populations (see

current theoretical models are sensitive to various assumptions on the production and escape of ionizing photons in high- $z$  galaxies that can be distinct from their low- $z$  counterparts (see, e.g., Madau et al. 2024; Liu et al. 2025a; Dhandha et al. 2025; Gnedin 2025). We defer the con-

sideration of observational constraints from reionization to future work (see, e.g., Chakraborty & Choudhury 2025; Ma et al. 2025).

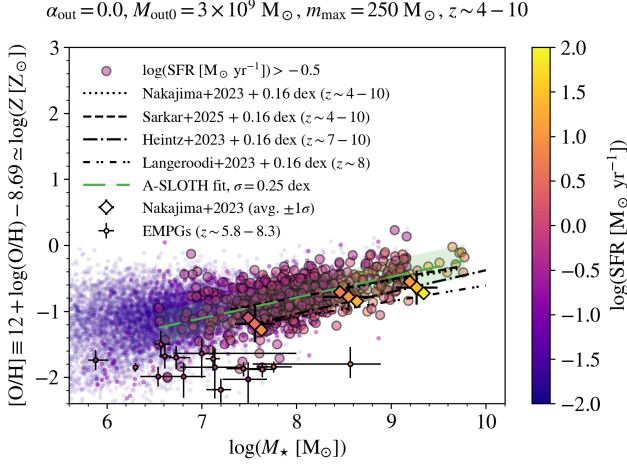


**Fig. 10.** MZR at  $z \sim 4 - 10$  for the best-fit model with  $\alpha_{\text{out}} = 0$ ,  $M_{\text{out}0} = 3 \times 10^9 M_{\odot}$ , and  $m_{\text{max}} = 250 M_{\odot}$ . Simulated galaxies with  $\log(\text{SFR} [M_{\odot} \text{ yr}^{-1}]) > -2$  are shown as dots color-coded by SFR. The detectable ones with  $\log(\text{SFR} [M_{\odot} \text{ yr}^{-1}]) > -0.5$  are highlighted by large circles, from which we derive the MZR as the long dashed line. The dotted and dashed lines show the MZR of JWST galaxies at  $z \sim 4 - 10$  from Nakajima et al. (2023) and Sarkar et al. (2025) (which almost coincide with each other and with the simulated MZR), while the dash-dotted and dot-dash-dotted lines show the fits from Heintz et al. (2023, for  $z \sim 8$ ) and Langeroodi et al. (2023, for  $z \sim 7 - 10$ ). Here, every observed MZR has been corrected for the SFR bias (see Sec. 4.2 and Appendix A). The original average values (without correction) of  $\log M_*$ ,  $[\text{O}/\text{H}]$ , and SFR of the JWST galaxies from Nakajima et al. (2023, see their table. 2) are shown with the diamonds. Each data point involves three diamonds color-coded by the mean and  $1\sigma$  upper and lower limits of SFR. The relevant scatter in  $\log M_*$  and  $[\text{O}/\text{H}]$  are shown by errorbars. The small dots with errorbars denote the EMPG candidates ( $[\text{O}/\text{H}] \lesssim -1.7$ ) observed by JWST at  $z \sim 5.8 - 8.3$  (Chemerynska et al. 2024; Mowla et al. 2024; Cullen et al. 2025; Hsiao et al. 2025) color-coded by the best-fit SFR value measured from observations.

Donnan et al. (2025, see Eq. 14). Again, the observed CSMD is well reproduced at  $z \lesssim 10$ , while the agreement breaks down at higher  $z$  due to the poor sampling of massive galaxies in our small simulation box. Low-mass ( $M_* \lesssim 10^8 M_{\odot}$ ) galaxies dominate the cumulative stellar mass budget at  $z \gtrsim 10$ .

Regarding chemical evolution of high- $z$  galaxies, we first plot individual simulated galaxies in the  $[\text{O}/\text{H}]$ - $\mu_{0.66}$  space in Fig. 9 for two redshift ranges:  $z \sim 4 - 8$  (left) and  $z \sim 8 - 10$  (right). The universal FMR from Andrews & Martini (2013), which appears to be invariant up to  $z \sim 8$ , and the observational results of JWST at  $z \sim 4 - 10$  from Nakajima et al. (2023) are shown for comparison. We derive a linear fit from the simulation data for detectable galaxies with  $\text{SFR} > 10^{-0.5} M_{\odot} \text{ yr}^{-1}$  and calculate the scatter around this fit. In general, we find good agreement between theoretical predictions and observations. The linear fit for simulated galaxies at  $z \sim 4 - 8$  gives  $[\text{O}/\text{H}] = (0.35 \pm 0.02)\mu_{0.66} - 3.56 \pm 0.19$  with a scatter of  $\sigma \sim 0.24$  dex. This is consistent with the FMR at  $z \lesssim 8$  in observations (Eq. 15) within  $1\sigma$  but has a slightly smaller slope. We find that the FMR slope increases with larger  $\alpha_{\text{out}}$  in our simulations (reaching  $\sim 0.7$  for  $\alpha_{\text{out}} = 1$ ), which reflects the enhanced (reduced) ability of metal retention under weaker (stronger) outflows in massive (low-mass) halos (see Eqs. 6 and 5). If we use  $\alpha_{\text{out}} \sim 0.5$  and  $M_{\text{out}0} \sim 3 \times 10^9 M_{\odot}$  at  $z \lesssim 6$ , as supported by the observed CSFH (see Fig. 8 and Appendix B), the FMR slope becomes larger, achieving perfect agreement with the ob-

served FMR. The scatter around the FMR in observations at  $z \lesssim 3$  is  $\sigma = 0.13$  dex (Andrews & Martini 2013), smaller than that in our simulation. However, we find a similar (total) scatter  $\sigma \sim 0.27$  dex for the JWST galaxies at  $z \sim 4 - 10$  (see fig. 6 of Sarkar et al. 2025), although the intrinsic scatter is expected to be smaller and closer to the low- $z$  value once observational uncertainties are removed. The breaking of the universal FMR at  $z \gtrsim 8$  is well reproduced by our simulation (even if we do not consider  $z > 8$  galaxies in the likelihood of MZSFR): There is a systematic offset from the universal FMR by around  $-0.27$  dex for both simulated and observed galaxies at  $z \sim 8 - 10$ . Besides, the scatter around FMR generally increases at higher  $z$  in our simulation as  $\sigma \sim 0.22, 0.26$ , and  $\sim 0.3$  dex at  $z \sim 4 - 6, z \sim 6 - 8$ , and  $z \sim 8 - 10$ , respectively. This implies that the FMR can have subtle redshift evolution even at  $z \lesssim 8$ , as shown in cosmological hydrodynamic simulations (e.g., Garcia et al. 2024, 2025). Current observations and our simulations at  $z \gtrsim 4$  are still limited by galaxy sample sizes and are therefore unable to accurately characterize such redshift evolution.

Next, we consider the MZR at  $z \sim 4 - 10$  in a similar manner, as shown in Fig. 10. Here we plot the MZR from four observational studies: Sarkar et al. (2025), Nakajima et al. (2023), Langeroodi et al. (2023, for  $z \sim 8$ ), and Heintz et al. (2023, for  $z \sim 7 - 10$ ). We shift the observed MZR upwards by  $\Delta[\text{O}/\text{H}] \simeq 0.16$  dex in each case to correct for observational biases (detailed in Sec. 4.2 and Appendix A). The first two studies consider galaxies exactly at  $z \sim 4 - 10$  and produce almost identical results that are in perfect agreement with the MZR derived from the detectable galaxies with  $\text{SFR} > 10^{-0.5} M_{\odot} \text{ yr}^{-1}$  in our simulation, namely,  $[\text{O}/\text{H}] = (0.31 \pm 0.02)\log(M_* [M_{\odot}]) - 3.3 \pm 0.14$ . The latter two studies only involve galaxies at  $z \sim 7 - 10$ , so the resulting MZR is systematically lower by  $\sim 0.2 - 0.3$  dex, consistent with the trend seen in the FMR. The scatter in  $[\text{O}/\text{H}]$  around the MZR is  $\sigma \sim 0.2 - 0.3$  dex in observations (Nakajima et al. 2023), which is consistent with the scatter  $\sigma \simeq 0.25$  dex found in the simulated galaxies. Note that the scatter reported by Nakajima et al. (2023) also includes the uncertainties in metallicity and mass measurements. Subtracting such uncertainties can result in a smaller intrinsic scatter  $\sim 0.16$  dex as estimated by Sarkar et al. (2025).

Below  $M_* \lesssim 10^8 M_{\odot}$ , the MZR of simulated galaxies starts to flatten towards smaller  $M_*$ , and meanwhile, the scatter around MZR increases. Thanks to this boosted metallicity spread, our simulation can produce extremely metal-poor galaxies (EMPGs) with  $[\text{O}/\text{H}] \lesssim -1.7$  (i.e., below  $\sim 2\%$  solar metallicity),  $\log(M_* [M_{\odot}]) \sim 6.5 - 8$ , and  $\text{SFR} \sim 0.2 - 2 M_{\odot} \text{ yr}^{-1}$ , similar to those found in recent JWST observations at  $z \sim 5.8 - 8.3$  (Chemerynska et al. 2024; Mowla et al. 2024; Cullen et al. 2025; Hsiao et al. 2025). Like in the case of FMR, the MZR slope increases with larger  $\alpha_{\text{out}}$  in our simulations, so  $\alpha_{\text{out}} \sim 0$  is also supported by the observed slope.

In Fig. 11, we compare the redshift evolution of metallicity (left) and stellar mass (right) of *detectable* galaxies ( $\text{SFR} > 10^{-0.5} M_{\odot} \text{ yr}^{-1}$ ) in our simulation with that seen in observations (Sarkar et al. 2025). Here, the observed galaxies has a median stellar mass  $M_* \sim 10^{8.3} M_{\odot}$  that hardly evolves with redshift. The simulated galaxies have a mass distribution around this median value similar to the observed one at  $z \lesssim 7$ . However, at higher  $z$ , the simulated galaxies are systematically less massive than the observed galaxies by  $\sim 0.4 - 0.8$  dex. This again reflects the fact that high- $z$  observations are biased by massive, luminous objects with respect to the galaxy sample in our small simulation box. Sarkar et al. (2025) fit the observed galaxies with a plane in



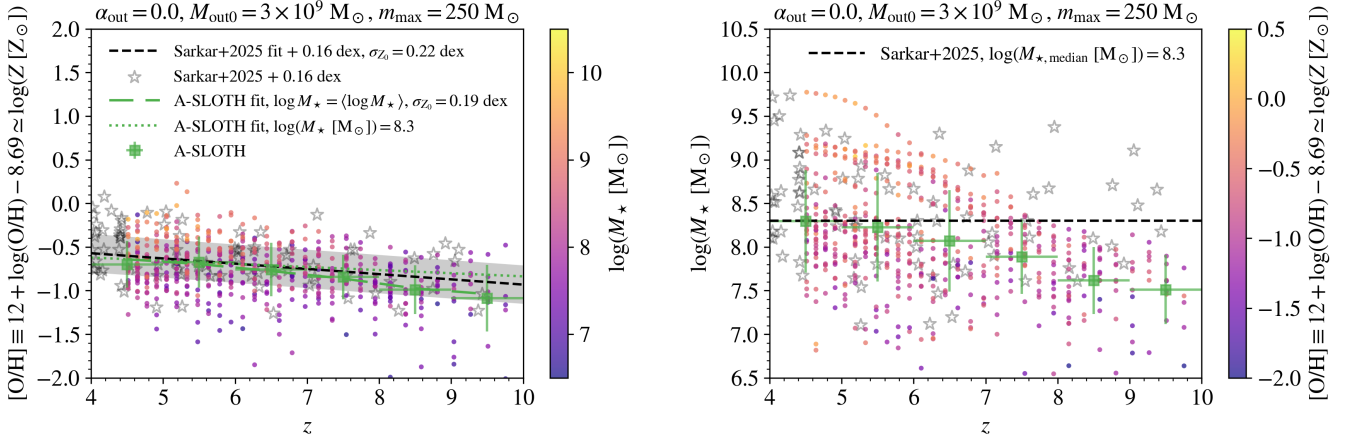


**Fig. 11.** Redshift evolution of metallicity (left) and stellar mass (right) of detectable galaxies with  $\log(\text{SFR} [M_{\odot} \text{ yr}^{-1}]) > -0.5$  in our simulation for the best-fit model with  $\alpha_{\text{out}} = 0$ ,  $M_{\text{out}0} = 3 \times 10^9 M_{\odot}$ , and  $m_{\text{max}} = 250 M_{\odot}$ . Individual observed galaxies from Sarkar et al. (2025) are shown as empty stars. Individual simulated galaxies are shown as dots, color-coded by  $\log M_{\star}$  and  $[O/H]$  on the left and right panels, respectively. The corresponding average value and  $1\sigma$  scatter at 6 redshift bins (with  $\Delta z = 1$ ) are shown as the squares and errorbars. A linear fit in the form of  $[O/H] = Z_0 + a \log(M_{\star} [M_{\odot}]) + b(1+z)$  is derived from the simulated galaxies. In the left panel, we show this fit evaluated at the average  $\log M_{\star}$  of simulated galaxies (with weights described in Sec. 4.2) as the lone dashed line and at the median stellar mass of observed galaxies as the dotted line. For the former, the uncertainty in the normalization  $Z_0$  is  $\sigma_{Z_0} \approx 0.19$  dex. For the latter, we take the median stellar mass of galaxies observed by JWST  $\log(M_{\star, \text{median}} [M_{\odot}]) = 8.3$  from Sarkar et al. (2025), which is shown by the dashed horizontal line on the right panel. The same median stellar mass is substituted to the  $[O/H]$ - $\log M_{\star}$ - $z$  relation derived from the JWST galaxies (Sarkar et al. 2025, see their eq. 12 and fig. 8), as shown by the dashed line on the left panel. Here, we also shift the observational data points and relation upwards by  $\Delta[O/H]_{\text{MZR}} \sim 0.16$  dex to correct for the bias in SFR (see Sec. 4.2 and Appendix A). The relevant uncertainty in  $Z_0$  from observations is  $\sigma_{Z_0} = 0.22$  dex as shown by the gray shaded region, which agrees well with that found in our simulation ( $\sigma_{Z_0} \approx 0.19$  dex).

the  $[O/H]$ - $\log M_{\star}$ - $z$  space as

$$[O/H] = Z_0 + a \log(M_{\star} [M_{\odot}]) + b(1+z), \quad (17)$$

with best-fit values  $Z_0 = -2.40 \pm 0.22$ ,  $a = 0.237 \pm 0.023$ , and  $b = -0.06 \pm 0.01$ . To compare this with our simulation data, we shift the normalization  $Z_0$  upwards by  $\Delta[O/H]_{\text{MZR}} = 0.16$  dex to correct for the SFR bias (see Sec. 4.2 and Appendix A), which gives  $Z_0 = -2.24 \pm 0.22$ . As shown in the left panel of Fig. 11, the simulated galaxies have a similar distribution in the  $[O/H]$ - $z$  space as the observed distribution at  $z \lesssim 7$ , and become more metal-poor at  $z \gtrsim 7$ . Fitting the simulated galaxies with the same formula (Eq. 17) gives  $Z_0 = -2.77 \pm 0.19$ ,  $a = 0.281 \pm 0.019$ , and  $b = -0.036 \pm 0.008$ , which are generally consistent with the corrected best-fit plane in observations within  $\sim 1\sigma$ . The main difference is that there is stronger (weaker) dependence of metallicity on mass (redshift) in the simulated galaxies. This seems counterintuitive considering the selection bias towards more massive galaxies at higher  $z$  (see the right panel of Fig. 11). If these galaxies are metal-richer than lower-mass galaxies, there should be an underestimation of the redshift evolution (with larger  $b$ ) in the  $[O/H]$ - $\log M_{\star}$ - $z$  relation from observations (Sarkar et al. 2025). However, higher- $z$  observations of metal lines are also biased towards higher-SFR galaxies to a degree larger than that of the stellar mass bias. Such galaxies can be more metal-poor despite their larger masses as indicated by the FMR (Fig. 9), thus reversing the trend. This highlights the necessity of taking SFR into account for characterization of galaxy chemical evolution.

We end this subsection with a brief discussion of the halo-galaxy connection. In Fig. 12, we compare the SHMR of simulated galaxies (with  $\text{SFR} > 10^{-0.5} M_{\odot} \text{ yr}^{-1}$ ) at  $z \sim 4-10$  with the results of four semi-empirical models: Tacchella et al. (2018, at  $z = 6.3$ ), Behroozi et al. (2019, at  $z = 4$  and 10), Stefanon et al. (2021, for  $z \sim 6-10$ ), and Zaritsky & Behroozi (2023, in the

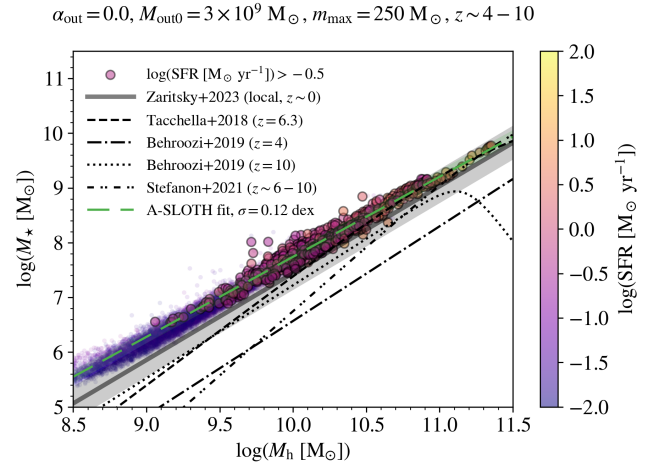


**Fig. 12.** SHMR at  $z \sim 4-10$  for the best-fit model with  $\alpha_{\text{out}} = 0$ ,  $M_{\text{out}0} = 3 \times 10^9 M_{\odot}$ , and  $m_{\text{max}} = 250 M_{\odot}$ . Simulated galaxies with  $\log(\text{SFR} [M_{\odot} \text{ yr}^{-1}]) > -2$  are shown as dots color-coded by SFR. The detectable ones with  $\log(\text{SFR} [M_{\odot} \text{ yr}^{-1}]) > -0.5$  are highlighted by large circles, from which we derive the SHMR as the long dashed line and green shaded region (for  $1\sigma$  scatter). The results of four semi-empirical models are shown for comparison: Zaritsky & Behroozi (2023, thick solid, at  $z \sim 0$ ), Tacchella et al. (2018, dashed, at  $z = 6.3$  as the average redshift of detectable simulated galaxies), Behroozi et al. (2019, dash-dotted for  $z = 4$  and dotted for  $z = 10$ ), and Stefanon et al. (2021, dot-dash-dotted, at  $z \sim 6-10$ ). The shaded region around the solid curve illustrates the scatter  $\sigma_{\text{SHMR}} = 0.31$  dex from Zaritsky & Behroozi (2023).

local Universe,  $z \sim 0$ ). Although these models show large discrepancies among themselves (up to  $\sim 1$  dex in stellar mass for a



given halo mass), they all lie below the SHMR of our simulated galaxies. One explanation is that because massive star-forming galaxies in large-scale over-dense regions are poorly sampled in our small simulation box, the sampled halos are forced to form more stars than they would on cosmic average in order to reproduce the observed CSFH. Despite this possible bias from cosmic variance, the simulated SHMR is consistent with that inferred from local ( $z \sim 0$ ) dwarf galaxies (Zaritsky & Behroozi 2023) within  $1\sigma$  and covers a reasonable range of halo-scale cumulative SFE  $\eta_{\text{halo}} \equiv M_{\star}/[(\Omega_b/\Omega_m)M_h] \propto M_h^{0.46} \sim 0.014 - 0.2$  for  $M_h \sim 10^9 - 10^{10.5} M_{\odot}$ . The scatter in  $M_{\star}$  around the SHMR is  $\sigma \sim 0.12$  dex, comparable to that ( $\sigma \sim 0.14 - 0.18$  dex) found in Tacchella et al. (2018).

## 6. Discussion

The star formation and chemical enrichment histories of high- $z$  galaxies have broad implications for the observational signatures of the early Universe beyond those considered in our work (Sec. 4). However, it is challenging to make robust theoretical predictions due to uncertainties in the modeling of the rich physics involved across a large range of scales. Such uncertainties call for prudent interpretations of our findings. Below, we first briefly comment on the implications of our results on PISNe and binary black hole mergers as high- $z$  transient sources (Sec. 6.1). Then we discuss the uncertainties/caveats in our simulations (Sec. 6.2).

### 6.1. Implications for transient rates

The cosmic rate of PISNe is determined by (1) metal-dependent CSFH, (2) IMF, and (3) (binary) stellar evolution (e.g., Briel et al. 2022; Tanikawa et al. 2023; Gabrielli et al. 2024; Simonato et al. 2025). Although current observational constraints are limited to the local Universe (e.g., Schulze et al. 2024), future observations with upcoming facilities (e.g., Roman Space Telescope and Vera C. Rubin Observatory) will probe the high- $z$  regime (e.g., Liu & Bromm 2020; Venditti et al. 2024). In this work, (3) is fixed, (2) is calibrated to reproduce the observed MZSFR and overall CSFH (of bright galaxies), and (1) is predicted by the simulation. Since IMF models with  $m_{\text{max}} \gtrsim 200 M_{\odot}$  are preferred by the observed MZSFR, we find significant contributions of Pop II stars to PISN events at  $z \lesssim 15$ . The resulting PISN rate (i.e., all-sky number of events per year per redshift per unit solid angle) peaks around  $z \sim 5$  as  $d\dot{N}_{\text{PISN}}/dz \sim 10 \text{ yr}^{-1} \text{ deg}^{-2}$  in our best-fit models (Sec. 5.1) with  $m_{\text{max}} \sim 200 - 250 M_{\odot}$ . On the other hand, for the models with  $m_{\text{max}} = 100 M_{\odot}$  that marginally reproduce the observed CSFH (see the triangles in the top and middle panels of Fig. 8), PISNe are only produced by Pop III stars<sup>23</sup>. The corresponding PISN rate reaches a much lower peak of  $d\dot{N}_{\text{PISN}}/dz \sim 0.1 \text{ yr}^{-1} \text{ deg}^{-2}$  around  $z \sim 10 - 15$  and decrease towards lower  $z$  down to  $\sim 0.01 \text{ yr}^{-1} \text{ deg}^{-2}$  at  $z \sim 5$ , generally consistent with the findings of previous studies considering only Pop III PISNe (e.g., Hummel et al. 2012; Magg et al. 2016; Lazar & Bromm 2022; Venditti et al. 2024; Wiggins et al. 2024).

Our predictions on (1) metal-dependent CSFH also have interesting implications for gravitational wave transients such as binary black hole mergers. Binary population synthesis studies

show that the formation efficiency of binary black hole mergers from isolated binary stellar evolution increases significantly (by  $\sim 1 - 4$  orders of magnitude) when the stellar metallicity decreases from solar to below  $\sim 0.1 Z_{\odot}$  (e.g., Klencki et al. 2018; Giacobbo & Mapelli 2018; Spera et al. 2019; Broekgaarden et al. 2022; Iorio et al. 2023). As a result, the cosmic merger rate density of binary black holes is highly sensitive to the SFRD of metal-poor stars (Boco et al. 2019, 2021; Chruślińska & Nelemans 2019; Chruślińska et al. 2021; Briel et al. 2022; Chruślińska 2024; Sgalletta et al. 2024). As discussed by Sgalletta et al. (2024), most (semi-empirical) studies derive the metal-dependent SFRD from the observed total SFRD and galaxy scaling relations under various assumptions, which suffers from large uncertainties regarding the contribution of low-mass ( $M_{\star} \lesssim 10^8 M_{\odot}$ ) galaxies that typically host metal-poor stars but are difficult to detect at high  $z$ . With the well-calibrated semi-analytical galaxy evolution model of A-SLOTH, our simulations naturally predict the metal-dependent SFRD, self-consistently capturing the contribution of the smallest galaxies in the standard  $\Lambda$ CDM universe (with  $M_{\star} \sim 1000 M_{\odot}$  and  $M_h \sim 10^6 M_{\odot}$ ) thanks to the high resolution. It is found in our best-fit model that the SFRD of metal-poor stars with  $[\text{O}/\text{H}] < -1$  is  $\sim 0.005 - 0.01 M_{\odot} \text{ yr}^{-1} \text{ cMpc}^{-3}$  at  $z \sim 4.5 - 8$ , which slowly decreases towards lower  $z$  and remains within the range ( $0.001 - 0.02 M_{\odot} \text{ yr}^{-1} \text{ cMpc}^{-3}$ ) found in semi-empirical models (e.g., Chruślińska & Nelemans 2019; Chruślińska et al. 2021). Moreover, the metal-poor SFRD dominates the total SFRD of simulated galaxies at  $z \gtrsim 8$  that are mostly very faint with  $\text{SFR} \lesssim 0.1 M_{\odot} \text{ yr}^{-1}$  (see Fig. 8). The predicted metal-poor SFRD also exceeds the SFRD of UV-bright ( $M_{\text{UV}} \lesssim -17$ ) galaxies inferred from observations (Table 2) by up to one order of magnitude at  $z \sim 8 - 13.5$ . This highlights the important role of faint, low-mass, metal-poor galaxies in producing high- $z$  binary black hole mergers, which will be observed by 3rd-generation gravitational wave detectors to bring us additional constraints on early galaxy evolution (Abac et al. 2025). We plan to explore the rates and detectability of binary black hole mergers and PISNe in detail in a follow-up study.

### 6.2. Caveats

Although our best-fit model reproduces observations very well (Sec. 5.2), the particular IMF and galactic outflow properties required in this model are sensitive to the assumptions made in the galaxy evolution prescription (Sec. 2) and the numerical setup of simulations (Sec. 3). Below, we summarize the key underlying caveats/uncertainties in our modeling (in descending order of the scales involved) and evaluate their possible effects on our results.

1. As a tradeoff for high resolution, our simulation volume is rather small ( $\sim 2000 \text{ cMpc}^3$ ) and cannot capture large-scale ( $\gtrsim 10 \text{ cMpc}$ ) perturbations, leading to poor sampling of the relevant over-dense regions hosting massive/high-SFR galaxies. On the other hand, high- $z$  observations (of metal lines) are biased towards luminous objects. The observational data from JWST spectroscopy considered in our analysis mostly involve galaxies with  $M_{\text{UV}} \lesssim -17$  (corresponding to  $\text{SFR} \gtrsim 10^{-0.5} M_{\odot} \text{ yr}^{-1}$ ) at  $z \sim 4 - 10$ . As an attempt to achieve fair comparison, we only focus on such detectable galaxies and consider their cumulative (rather than statistical) properties and scaling relations. However, the actual number of galaxies with  $\text{SFR} > 10^{-0.5} M_{\odot} \text{ yr}^{-1}$  in our simulation volume is only around  $\sim 3 - 40$  at  $z \sim 4 - 10$ , which

<sup>23</sup> Irrespective of origin (Pop II or Pop III), the possible nucleosynthetic PISN signature could be preserved in the high- $z$  IGM, which in turn could be probed through future absorption spectroscopy with bright gamma-ray burst afterglows as background sources (Wang et al. 2012).

is lower than the number of observed galaxies by at least a factor of a few. Therefore, our results may suffer from uncertainties of small-sample statistics<sup>24</sup>. Beyond statistical uncertainties, there are also systematic differences between the simulated and observed galaxies under the same detection limit/SFR threshold. The latter generally have a higher SFR (at a given stellar mass) by  $\sim 0.6$  dex (Appendix A), and are also more massive at  $z \gtrsim 7$  (Fig. 11). Although we manage to make a correction to MZR through FMR to ensure their consistency (Sec. 4.2), it is non-trivial to evaluate the effects of selection biases on galaxy scaling relations.

2. Accurate measurements of SFR, stellar mass, and metallicity are challenging in observations of high- $z$  galaxies. The observational results considered here are mostly based on indicators/calibrations established in the low- $z$  Universe, which may cause large uncertainties and even systematic biases when applied to high- $z$  galaxies. For instance, it is shown in Wang et al. (2025a) that state-of-the-art inference methods fail to capture SFR fluctuations on tens of Myr timescales, so the stellar mass is typically underestimated by  $\sim 0.15$  dex in bursty systems. Moreover, large discrepancies (up to  $\sim 0.4$  dex) exist in the metallicity measurements from different calibrations (e.g., Chemerynska et al. 2024, see their fig. 5), which, mixed up with selection biases, can shift the metallicity scaling relations around (e.g., Korhonen Cuestas et al. 2025). In fact, the MZR at  $z \sim 3 - 10$  obtained by Chakraborty et al. (2024) using direct- $T_e$ -based metallicities is  $\sim 0.2$  dex below the MZR adopted in our analysis from earlier studies using line-ratio metallicity indicators (Nakajima et al. 2023; Curti et al. 2024; Sarkar et al. 2025). If we attribute this outcome to a systematic overestimation of metallicities by the canonical line-ratio method, less metal yields will be required to reproduce the observed MZSFR, corresponding to  $m_{\text{max}} \sim 100 - 200 M_\odot$  according to our stellar population model (Sec. 2.4). On the other hand, the direct- $T_e$  method also suffers from uncertainties in ISM photo-ionization models (e.g., Cameron et al. 2023; Hayes et al. 2025) and can underestimate the metallicity if a low electron density (e.g.,  $n_e \sim 300 \text{ cm}^{-3}$ ) suitable for local galaxies is assumed while higher electron densities ( $n_e = 10^3 - 10^6 \text{ cm}^{-3}$ ) are typically found in high- $z$  galaxies (e.g., Mingozi et al. 2022, Martinez et al. in prep.).
3. We adopt a simple model for metal enrichment in which metals are uniformly mixed into the gas reservoir currently retained by the halo, and outflows carry away metals proportionally from this reservoir (Sec. 2.3). In reality, the distribution of metals in different components of the ISM/CGM/IGM (e.g., cold gas, hot gas, accreted gas, and outflows) can be more complex than this ‘well-mixed’ picture. For instance, it is found by (e.g., Nishigaki et al. 2025) that a multi-phase metallicity model that treats metallicities in  $\text{H}_2$  and HI regions separately is needed to spontaneously reproduce metal scaling relations in star-forming regions, HI regions, and the CGM at  $z \lesssim 5$ . In particular, they find that the fraction of metals mixed into the star-forming regions decreases towards higher  $z$  and smaller halo mass. In our work, we focus on a higher- $z$  regime, and only consider the metal-

licity of star-forming (HII) regions that is traced by nebular lines in observations and young ( $\lesssim 10$  Myr) massive ( $\gtrsim 5 M_\odot$ ) stars in our simulations. We use a stochastic model based on cosmological simulations (Tarumi et al. 2020) to capture the difference between this metallicity and the ‘well-mixed’ average gas-phase metallicity. Therefore, any uncertainties in the simulation results underlying this model will propagate into our results. Besides, our approach may fail to fully capture the redshift and halo mass dependence of the metal distribution fractions in star-forming and HI regions if its effects are not degenerate to those of galactic outflows explored in our simulations (which in principle only control the distribution of metals between IGM/CGM and ISM).

4. Our prescription for star formation and stellar feedback may be oversimplified with respect to the complex baryon cycles in reality (Boardman et al. 2025). For instance, the SFE is fixed throughout our simulations, while analytical models and cloud-scale simulations of star formation typically find higher SFE for a higher cloud mass and/or gas surface density (e.g., Federrath & Klessen 2012; Kim et al. 2018; He et al. 2019; Lancaster et al. 2021; Menon et al. 2024; Polak et al. 2024), which is also confirmed in observations (Rawat et al. 2025). Taking this into account leads to higher SFE in higher- $z$  galaxies, which helps to explain the ‘excess’ of UV-luminous galaxies observed by JWST (e.g., Inayoshi et al. 2022; Dekel et al. 2023; Somerville et al. 2025; Yung et al. 2025). The model for SN-driven galactic outflows can also be validated/refined based on the outflow properties inferred from observations (e.g., Xu et al. 2022; Birkin et al. 2025; Saldana-Lopez et al. 2025; Xu et al. 2025b,a), which we defer to future work. In general, our results are model-dependent and should be interpreted with caution (for alternative semi-analytical galaxy evolution models, see sec. 1.2 of Hartwig et al. 2022). It has also been found in cosmological hydrodynamic simulations that the detailed features of MZSFR, i.e., the normalizations, slopes, and scatters of MZR and FMR as well as their redshift evolution, are highly sensitive to the sub-grid models for star formation and stellar feedback (e.g., Garcia et al. 2024, 2025). Current samples of observed galaxies at  $z \gtrsim 4$  are still too small to characterize such detailed features, so do the galaxy populations in our work with a limited simulation volume.
5. We assume that the IMF is an invariant function at  $z > 4.5$ , thus focusing on the galaxy-population-averaged IMF. In reality, this IMF can still vary with redshift due to the variation of star formation condition and the environmental dependence of IMF that has been commonly seen in simulations (e.g., Chon et al. 2021; Mathew & Federrath 2021; Mathew et al. 2023, 2025; Guszejnov et al. 2022; Hennebelle et al. 2022; Hix et al. 2023; Chon et al. 2024; Liu et al. 2024a; Tanvir & Krumholz 2024) and observations (e.g., Gunawardhana et al. 2011; Marks et al. 2012; Jeřábková et al. 2018; Dib 2023; Rusakov et al. 2023). In fact, we find tentative evidence for evolution of galactic outflow parameters with redshift at  $z \lesssim 6$  based on the observed CSFH (see Fig. 8 and Appendix B), which favors decreasing outflow efficiency at lower redshifts in relatively massive halos ( $M_h \gtrsim 10^9 M_\odot$ ). This evolution may also be interpreted as the variation of IMF or stellar evolution tracks (see below), reducing the number and/or SN energy output of massive stars at lower- $z$ , more massive, and metal-rich galaxies.
6. Our results are also sensitive to uncertainties in stellar evolution models regarding initial chemical composition, nuclear reaction rates, convection, mixing, winds, rotation, SN ex-

<sup>24</sup> In practice, the evolution tracks of simulated galaxies are ‘observed’ at many snapshots to produce a large galaxy sample that is used to compare with observations. This approach can capture the internal stochastic processes in galaxy evolution. A large number of evolution tracks is still needed to fully capture the diversity of halo assembly histories and environmental factors (e.g., external metal enrichment and ionization feedback).

plosion physics, and binary interactions, which are still under intense investigation. Such uncertainties not only affect the radiative feedback of living massive stars but also regulate their metal yields and SN energy outputs (e.g., Cescutti & Chiappini 2010; Nomoto et al. 2013; Kobayashi et al. 2020; Marchant & Moriya 2020; Farmer et al. 2021, 2023; Tanikawa et al. 2021; Briel et al. 2022; Jeena et al. 2023; Martinet et al. 2023; Sabhahit et al. 2023; Gabrielli et al. 2024; Lecroq et al. 2024; Roberti et al. 2024; Tsiatsiou et al. 2024; West et al. 2024; Yates et al. 2024; Byrne et al. 2025; Higgins et al. 2025; Liu et al. 2025a; Pepe et al. 2025; Schneider et al. 2025; Shepherd et al. 2025; Simonato et al. 2025; Xin et al. 2025, Boco et al. in prep., Tornamenti et al. in prep.). Our finding that  $m_{\max} \gtrsim 200 M_{\odot}$  (for a Kroupa-like IMF with a high-mass-end power-law slope of  $\alpha_{\text{IMF}} = 2.3$ ) is favored by the observed MZSFR is based on the specific SN models and non-rotating single star evolution tracks discussed in Sec. 2.4. The key requirement to reproduce observations is an IMF-averaged metal yield (per unit stellar mass)  $M_Z \sim 0.03 - 0.04$  under an IMF-averaged SN energy output (per unit stellar mass)  $\mathcal{E}_{\text{SN}} \sim 1.2 - 1.6 \times 10^{49} \text{ erg } M_{\odot}^{-1}$  (see Fig. 3). Alternative stellar evolution models and/or IMF forms can also provide similar conditions. For instance, if the upper mass limit is fixed to a lower value  $m_{\max} = 120$  (150)  $M_{\odot}$  while the power-law slope  $\alpha_{\text{IMF}}$  at the high-mass end of the IMF ( $m_{\star} \in [0.5 M_{\odot}, m_{\max}]$ ) is allowed to vary,  $M_Z \sim 0.03 - 0.04$  can be achieved by  $\alpha_{\text{IMF}} \sim 1.5$  (2) with a moderately larger SN energy output  $\mathcal{E}_{\text{SN}} \sim 2 - 3 \times 10^{49} \text{ erg } M_{\odot}^{-1}$ . More detailed observational data on multiple elements beyond the bulk metallicity traced by O can hopefully break such degeneracy (e.g., Goswami et al. 2022; Arellano-Córdova et al. 2022; Charbonnel et al. 2023; D’Antona et al. 2023; Boardman et al. 2024; Nagele & Umeda 2023; Vink 2023; Cameron et al. 2024; Nandal et al. 2024b,a; Rizzuti et al. 2024; Watanabe et al. 2024; Gieles et al. 2025; Ji et al. 2025; Nandal et al. 2025; Schaerer et al. 2025; Nakane et al. 2025).

## 7. Summary

We explore the impact of IMF and SN-driven galactic outflows on the chemical evolution of high-redshift galaxies using the semi-analytical galaxy evolution code A-SLOTH (Hartwig et al. 2022, 2024; Magg et al. 2022a) with updated prescriptions for star formation and stellar feedback coupled to stellar evolution models covering the full metallicity range ( $Z \sim 10^{-11} - 0.03$ ), a broad stellar mass range ( $m_{\star} \sim 2 - 600 M_{\odot}$ ), and the metal yields from stellar winds, CCSNe, (pulsational) PISNe, and Type Ia SNe (Nomoto et al. 1997; Goswami et al. 2021, 2022; Costa et al. 2025). We perform 165 runs of A-SLOTH over the merger trees constructed from a high-resolution cosmological simulation (Ishiyama et al. 2016) to search for the IMF and galactic outflow parameters that can best reproduce the cosmic star formation history (CSFH, Bouwens et al. 2016; Donnan et al. 2023a,b; Harikane et al. 2023) and the stellar mass-metallicity-star formation rate relation (MZSFR, Nakajima et al. 2023; Curti et al. 2024; Sarkar et al. 2025) inferred from observations at  $z \sim 4 - 10$ .

We find that an IMF-averaged metal yield per unit stellar mass  $M_Z \sim 0.03 - 0.04$  under an IMF-averaged SN energy per unit stellar mass  $\mathcal{E}_{\text{SN}} \sim 1.2 - 1.6 \times 10^{49} \text{ erg } M_{\odot}^{-1}$  is required to reproduce the normalization of the observed MZSFR within  $1\sigma$ . Assuming that the IMF follows a Kroupa-like shape with a varying upper mass limit  $m_{\max}$ , this requirement can be fulfilled when  $m_{\max} \gtrsim 200 M_{\odot}$  that provides sufficient metal yields from

PISNe (see Fig. 3). Although this conclusion is subject to uncertainties in the adopted stellar evolution models and treatments of star formation and metal enrichment in different gas phases (Sec. 6.2), we confirm the findings of previous studies that very massive ( $\gtrsim 200 M_{\odot}$ ) stars play an important role in galaxy chemical evolution (e.g., Goswami et al. 2021, 2022; Charbonnel et al. 2023; Nagele & Umeda 2023; Vink 2023; Cameron et al. 2024; Nandal et al. 2024b,a; Watanabe et al. 2024; Gieles et al. 2025; Nandal et al. 2025; Schaerer et al. 2025). Besides, the need for PISNe to provide enough metals imply high PISNe rates: The all-sky event rate per redshift per unit solid angle peaks at  $d\dot{N}_{\text{PISN}}/dz \sim 10 \text{ yr}^{-1} \text{ deg}^{-2}$  around  $z \sim 5$ .

The CSFH inferred from observations involving UV-bright ( $M_{\text{UV}} \lesssim -17$ ) galaxies at  $z \gtrsim 6$  favors a galactic outflow model where the mass loss rate through outflows is proportional to the SN energy injection rate divided by the halo binding energy. This model is also preferred by the slope of MZSFR in observations. Our results support the conclusion in previous studies (e.g., Boardman et al. 2025; Nishigaki et al. 2025) that galactic metal enrichment is mainly governed by the gravitational potential (captured by the binding energy in our case). Under this model, we predict a large population of UV-faint ( $M_{\text{UV}} \gtrsim -17$ ) galaxies, which comprise  $\gtrsim 90\%$  of the total SFRD at  $z \gtrsim 12$  and remain an important component ( $\sim 30 - 50\%$ ) in the SFRD at  $z \sim 5 - 7$ . This prediction is in line with the observational evidence for significant contributions to reionization by unseen faint galaxies (e.g., Asthana et al. 2025; Kakiichi et al. 2025). Moreover, a significant fraction of such faint galaxies host metal-poor ( $\lesssim 0.1 Z_{\odot}$ ) stars that are promising progenitors of binary black hole mergers (e.g., Giacobbo & Mapelli 2018; Spera et al. 2019; Iorio et al. 2023). Such metal-poor stars dominate the total SFRD at  $z \gtrsim 8$  and even exceeds the SFRD of UV-bright ( $M_{\text{UV}} < -17$ ) galaxies inferred from observations (Table 2) by up to one order of magnitude within  $z \lesssim 13.5$ . This highlights the important role of faint, low-mass, metal-poor galaxies in making high- $z$  binary black hole mergers.

In conclusion, the star formation and chemical enrichment histories of high-redshift galaxies can provide valuable constraints on the abundance and feedback of massive stars, with profound implications for transient sources in both electromagnetic waves (e.g., PISNe) and gravitational waves (e.g., binary black hole mergers). Such implications will be investigated in detail in a follow-up study. Besides, stronger constraints can be obtained from detailed chemical abundances of unresolved galaxies/star clusters/clouds and metal-poor stars in our Galaxy (e.g., Salvadori et al. 2007; Frebel & Norris 2015; Ji et al. 2015; de Bennassuti et al. 2017; Fraser et al. 2017; Ishigaki et al. 2018; Kobayashi et al. 2020; Goswami et al. 2021, 2022; Rossi et al. 2021, 2023, 2024b,a; Koutsouridou et al. 2023; Vanni et al. 2023; Boardman et al. 2024; Rizzuti et al. 2024; Ji et al. 2025; Nakane et al. 2025). Benefiting from the flexibility and efficiency of A-SLOTH, our work establishes the foundation for future explorations of these topics.

**Acknowledgements.** We use the public open-source semi-analytic code A-SLOTH (<https://gitlab.com/thartwig/asloth>) for our models (Hartwig et al. 2022). The version used in this paper (including the new model for star formation and stellar feedback) is public at <https://gitlab.com/Treibeis/a-sloth-cob> (Liu et al. 2024b). We use the public open-source population synthesis code SEVN (<https://gitlab.com/sevncodes/sevn>) to generate compact remnant catalogs (Spera et al. 2019; Mapelli et al. 2020; Iorio et al. 2023) that are used to derive metal yields. The authors thank Gustavo Bruzual, Stephane Charlot, and Marie Lecroq for helpful discussions on stellar radiation. BL thanks Alex M. Garcia for inspiring discussions on the redshift evolution of metal scaling relations in simulations. The authors acknowledge the Texas Advanced Computing Center (TACC) for providing HPC resources under allocation AST22003. The authors acknowledge support by the state of

Baden-Württemberg through bwHPC and the German Research Foundation (DFG) through grants INST 35/1597-1 FUGG and INST 35/1503-1 FUGG. BL, MM, and RSK acknowledge the funding of the Deutsche Forschungsgemeinschaft (DFG, German Research Foundation) under Germany's Excellence Strategy EXC 2181/1 - 390900948 (the Heidelberg STRUCTURES Excellence Cluster). MM acknowledges financial support from the European Research Council for the ERC Consolidator grant DEMOBLACK, under contract no. 770017. RSK acknowledges financial support from the ERC via Synergy Grant 'ECOGAL' (project ID 855130), and from the German Ministry for Economic Affairs and Climate Action in project 'MAINN' (funding ID 50002206). RSK also thanks the 2024/25 Class of Radcliffe Fellows for highly interesting and stimulating discussions. GC acknowledges partial financial support from the European Union—Next Generation EU, Mission 4, Component 2, CUP: C93C24004920006, project 'FIRES'. BL thanks the organizers of The Inaugural Cosmic Frontier Center Conference at UT Austin, Texas, for providing a valuable platform to exchange ideas that helped improve this paper.

## References

- Abac, A., Abramo, R., Albanesi, S., et al. 2025, arXiv e-prints, arXiv:2503.12263
- Adams, N. J., Conselice, C. J., Austin, D., et al. 2024, *ApJ*, 965, 169
- Allende Prieto, C., Lambert, D. L., & Asplund, M. 2001, *ApJ*, 556, L63
- Andrews, B. H. & Martini, P. 2013, *ApJ*, 765, 140
- Aravindan, A., Liu, W., Canalizo, G., et al. 2023, *ApJ*, 950, 33
- Arca-Sedda, M. & Capuzzo-Dolcetta, R. 2014, *MNRAS*, 444, 3738
- Arellano-Córdova, K. Z., Berg, D. A., Chisholm, J., et al. 2022, *ApJ*, 940, L23
- Arjona-Gálvez, E., Cardona-Barrero, S., Grand, R. J. J., et al. 2025, arXiv e-prints, arXiv:2502.20398
- Asplund, M., Grevesse, N., Sauval, A. J., Allende Prieto, C., & Kiselman, D. 2004, *A&A*, 417, 751
- Asplund, M., Grevesse, N., Sauval, A. J., & Scott, P. 2009, *ARA&A*, 47, 481
- Asthana, S., Kulkarni, G., Haehnelt, M. G., et al. 2025, *MNRAS*, 539, L18
- Atek, H., Labbé, I., Furtak, L. J., et al. 2024, *Nature*, 626, 975
- Behroozi, P., Wechsler, R. H., Hearin, A. P., & Conroy, C. 2019, *MNRAS*, 488, 3143
- Bhatawdekar, R., Conselice, C. J., Margalef-Bentabol, B., & Duncan, K. 2019, *MNRAS*, 486, 3805
- Birkin, J. E., Spilker, J. S., Herrera-Camus, R., et al. 2025, arXiv e-prints, arXiv:2504.17877
- Boardman, N., Wild, V., & Asari, N. V. 2024, *MNRAS*, 534, L1
- Boardman, N. F., Wild, V., Vale Asari, N., & D'Eugenio, F. 2025, arXiv e-prints, arXiv:2505.07018
- Boco, L., Lapi, A., Chruslinska, M., et al. 2021, *ApJ*, 907, 110
- Boco, L., Lapi, A., Goswami, S., et al. 2019, *ApJ*, 881, 157
- Bosi, M., Lapi, A., Boco, L., et al. 2025, arXiv e-prints, arXiv:2503.22543
- Bouwens, R. J., Aravena, M., Decarli, R., et al. 2016, *ApJ*, 833, 72
- Bouwens, R. J., Oesch, P. A., Stefanon, M., et al. 2021, *AJ*, 162, 47
- Bouwens, R. J., Stefanon, M., Brammer, G., et al. 2023, *MNRAS*, 523, 1036
- Bressan, A., Marigo, P., Girardi, L., et al. 2012, *MNRAS*, 427, 127
- Briel, M. M., Eldridge, J. J., Stanway, E. R., Stevance, H. F., & Chrimes, A. A. 2022, *MNRAS*, 514, 1315
- Broekgaarden, F. S., Berger, E., Stevenson, S., et al. 2022, *MNRAS*, 516, 5737
- Byrne, C. M., Eldridge, J. J., & Stanway, E. R. 2025, *MNRAS*, 537, 2433
- Cain, C., Lopez, G., D'Aloisio, A., et al. 2025, *ApJ*, 980, 83
- Cameron, A. J., Katz, H., & Rey, M. P. 2023, *MNRAS*, 522, L89
- Cameron, A. J., Katz, H., Witten, C., et al. 2024, *MNRAS*, 534, 523
- Cescutti, G. & Chiappini, C. 2010, *A&A*, 515, A102
- Chabrier, G. 2003, *PASP*, 115, 763
- Chakraborty, A. & Choudhury, T. R. 2025, arXiv e-prints, arXiv:2503.07590
- Chakraborty, P., Sarkar, A., Smith, R., et al. 2024, arXiv e-prints, arXiv:2412.15435
- Charbonnel, C., Schaerer, D., Prantzos, N., et al. 2023, *A&A*, 673, L7
- Chemerynska, I., Atek, H., Dayal, P., et al. 2024, *ApJ*, 976, L15
- Chen, L.-H., Magg, M., Hartwig, T., et al. 2022, *MNRAS*, 513, 934
- Chen, X., Liu, Z., & Han, Z. 2024, *Progress in Particle and Nuclear Physics*, 134, 104083
- Chiaki, G., Tominaga, N., & Nozawa, T. 2017, *MNRAS*, 472, L115
- Chieffi, A. & Limongi, M. 2004, *ApJ*, 608, 405
- Chon, S., Hosokawa, T., Omukai, K., & Schneider, R. 2024, *MNRAS*, 530, 2453
- Chon, S., Omukai, K., & Schneider, R. 2021, *MNRAS*, 508, 4175
- Chruslinska, M. 2024, *Annalen der Physik*, 536, 2200170
- Chruslinska, M. & Nelemans, G. 2019, *MNRAS*, 488, 5300
- Chruslinska, M., Nelemans, G., Boco, L., & Lapi, A. 2021, *MNRAS*, 508, 4994
- Clarke, L., Shapley, A. E., Sanders, R. L., et al. 2024, *ApJ*, 977, 133
- Correa, C. A., Wyithe, J. S. B., Schaye, J., & Duffy, A. R. 2015, *MNRAS*, 452, 1217
- Costa, G., Girardi, L., Bressan, A., et al. 2019, *MNRAS*, 485, 4641
- Costa, G., Shepherd, K. G., Bressan, A., et al. 2025, *A&A*, 694, A193
- Cueto, E. R., Hutter, A., Dayal, P., et al. 2024, *A&A*, 686, A138
- Cullen, F., Carnall, A. C., Scholte, D., et al. 2025, arXiv e-prints, arXiv:2501.11099
- Curti, M., Maiolino, R., Curtis-Lake, E., et al. 2024, *A&A*, 684, A75
- D'Antona, F., Vesperini, E., Calura, F., et al. 2023, *A&A*, 680, L19
- de Bannassuti, M., Salvadori, S., Schneider, R., Valiante, R., & Omukai, K. 2017, *MNRAS*, 465, 926
- Dekel, A., Sarkar, K. C., Birnboim, Y., Mandelker, N., & Li, Z. 2023, *MNRAS*, 523, 3201
- Deng, Y., Li, H., Liu, B., et al. 2024, *A&A*, 691, A231
- Dhandha, J., Gessey-Jones, T., Bevins, H. T. J., et al. 2025, arXiv e-prints, arXiv:2503.21687
- Dib, S. 2023, *ApJ*, 959, 88
- Donnan, C. T., Dunlop, J. S., McLure, R. J., McLeod, D. J., & Cullen, F. 2025, arXiv e-prints, arXiv:2501.03217
- Donnan, C. T., McLeod, D. J., Dunlop, J. S., et al. 2023a, *MNRAS*, 518, 6011
- Donnan, C. T., McLeod, D. J., McLure, R. J., et al. 2023b, *MNRAS*, 520, 4554
- Donnan, C. T., McLure, R. J., Dunlop, J. S., et al. 2024, *MNRAS*, 533, 3222
- Dopcke, G., Glover, S. C. O., Clark, P. C., & Klessen, R. S. 2013, *ApJ*, 766, 103
- D'Silva, J. C. J., Driver, S. P., Lagos, C. D. P., et al. 2025, arXiv e-prints, arXiv:2503.03431
- Ekström, S. 2025, arXiv e-prints, arXiv:2502.06614
- Eldridge, J. J. & Stanway, E. R. 2022, *ARA&A*, 60, 455
- Farmer, R., Laplace, E., de Mink, S. E., & Justham, S. 2021, *ApJ*, 923, 214
- Farmer, R., Laplace, E., Ma, J.-z., de Mink, S. E., & Justham, S. 2023, *ApJ*, 948, 111
- Federrath, C. & Klessen, R. S. 2012, *ApJ*, 761, 156
- Ferrara, A. 2024, *A&A*, 689, A310
- Ferreira, L., Conselice, C. J., Sazonova, E., et al. 2023, *ApJ*, 955, 94
- Finkelstein, S. L., Bagley, M. B., Ferguson, H. C., et al. 2023, *ApJ*, 946, L13
- Finkelstein, S. L., Leung, G. C. K., Bagley, M. B., et al. 2024, *ApJ*, 969, L2
- Finkelstein, S. L., Ryan, Jr., R. E., Papovich, C., et al. 2015, *ApJ*, 810, 71
- Fraser, M., Casey, A. R., Gilmore, G., Heger, A., & Chan, C. 2017, *MNRAS*, 468, 418
- Frebel, A. & Norris, J. E. 2015, *ARA&A*, 53, 631
- Fryer, C. L., Belczynski, K., Wiktorowicz, G., et al. 2012, *ApJ*, 749, 91
- Gabrielli, F., Lapi, A., Boco, L., et al. 2024, *MNRAS*, 534, 151
- Garcia, A. M., Torrey, P., Ellison, S., et al. 2024, *MNRAS*, 531, 1398
- Garcia, A. M., Torrey, P., Ellison, S. L., et al. 2025, *MNRAS*, 536, 119
- Giacobbo, N. & Mapelli, M. 2018, *MNRAS*, 480, 2011
- Gieles, M., Padoan, P., Charbonnel, C., Vink, J. S., & Ramírez-Galeano, L. 2025, arXiv e-prints, arXiv:2501.12138
- Gnedin, N. Y. 2025, arXiv e-prints, arXiv:2504.10571
- Goswami, S., Silva, L., Bressan, A., et al. 2022, *A&A*, 663, A1
- Goswami, S., Slemer, A., Marigo, P., et al. 2021, *A&A*, 650, A203
- Gunawardhana, M. L. P., Hopkins, A. M., Sharp, R. G., et al. 2011, *MNRAS*, 415, 1647
- Guszejnov, D., Grudić, M. Y., Offner, S. S. R., et al. 2022, *MNRAS*, 515, 4929
- Harikane, Y., Ouchi, M., Oguri, M., et al. 2023, *ApJS*, 265, 5
- Hartwig, T., Lipatova, V., Glover, S. C. O., & Klessen, R. S. 2024, *MNRAS*, 535, 516
- Hartwig, T., Magg, M., Chen, L.-H., et al. 2022, *ApJ*, 936, 45
- Hartwig, T. & Yoshida, N. 2019, *ApJ*, 870, L3
- Hayes, M. J., Saldana-Lopez, A., Citro, A., et al. 2025, *ApJ*, 982, 14
- Hazenfratz, R., Barai, P., Lanfranchi, G. A., & Caproni, A. 2025, *ApJ*, 979, 238
- He, C.-C., Ricotti, M., & Geen, S. 2019, *MNRAS*, 489, 1880
- He, Z., Wang, E., Ho, L. C., et al. 2025, arXiv e-prints, arXiv:2505.06868
- Heintz, K. E., Brammer, G. B., Giménez-Arteaga, C., et al. 2023, *Nature Astronomy*, 7, 1517
- Hennebelle, P. & Grudić, M. Y. 2024, *ARA&A*, 62, 63
- Hennebelle, P., Lebreuilly, U., Colman, T., et al. 2022, *A&A*, 668, A147
- Higgins, E. R., Vink, J. S., Hirschi, R., Laird, A. M., & Sabhahit, G. 2025, arXiv e-prints, arXiv:2504.18621
- Higgins, E. R., Vink, J. S., Hirschi, R., Laird, A. M., & Sabhahit, G. N. 2023, *MNRAS*, 526, 534
- Hix, R., He, C.-C., & Ricotti, M. 2023, *MNRAS*, 522, 6203
- Hsiao, T. Y.-Y., Sun, F., Lin, X., et al. 2025, arXiv e-prints, arXiv:2505.03873
- Hummel, J. A., Pawlik, A. H., Milosavljević, M., & Bromm, V. 2012, *ApJ*, 755, 72
- Inayoshi, K., Harikane, Y., Inoue, A. K., Li, W., & Ho, L. C. 2022, *ApJ*, 938, L10
- Iorio, G., Mapelli, M., Costa, G., et al. 2023, *MNRAS*, 524, 426
- Ishigaki, M. N., Tominaga, N., Kobayashi, C., & Nomoto, K. 2018, *ApJ*, 857, 46
- Ishiyama, T., Sudo, K., Yokoi, S., et al. 2016, *ApJ*, 826, 9
- Jeena, S. K., Banerjee, P., Chiaki, G., & Heger, A. 2023, *MNRAS*, 526, 4467
- Jeong, T. B., Jeon, M., Song, H., & Bromm, V. 2025, *ApJ*, 980, 10
- Jerábková, T., Zonoozi, A. H., Kroupa, P., et al. 2018, *A&A*, 620, A39
- Ji, A. P., Frebel, A., & Bromm, V. 2015, *MNRAS*, 454, 659
- Ji, X., Belokurov, V., Maiolino, R., et al. 2025, arXiv e-prints, arXiv:2505.12505
- Jia, C., Wang, E., Lyu, C., et al. 2025, arXiv e-prints, arXiv:2504.18820



- Jiang, F., Dekel, A., Kneller, O., et al. 2019, *MNRAS*, 488, 4801
- Kakiichi, K., Jin, X., Wang, F., et al. 2025, arXiv e-prints, arXiv:2503.07074
- Kartaltepe, J. S., Rose, C., Vanderhoof, B. N., et al. 2023, *ApJ*, 946, L15
- Kim, J.-G., Kim, W.-T., & Ostriker, E. C. 2018, *ApJ*, 859, 68
- Kiyuna, M., Hosokawa, T., & Chon, S. 2023, *MNRAS*, 523, 1496
- Kiyuna, M., Hosokawa, T., & Chon, S. 2024, *MNRAS*, 534, 3916
- Klencki, J., Moe, M., Gladysz, W., et al. 2018, *A&A*, 619, A77
- Klessen, R. S. & Glover, S. C. O. 2023, *ARA&A*, 61, 65
- Klessen, R. S., Glover, S. C. O., & Clark, P. C. 2012, *MNRAS*, 421, 3217
- Kobayashi, C., Karakas, A. I., & Lugaro, M. 2020, *ApJ*, 900, 179
- Kobayashi, C., Umeda, H., Nomoto, K., Tominaga, N., & Ohkubo, T. 2006, *ApJ*, 653, 1145
- Korhonen Cuestas, N. A., Strom, A. L., Miller, T. B., et al. 2025, *ApJ*, 984, 188
- Koudmani, S., Rennehan, D., Somerville, R. S., et al. 2024, arXiv e-prints, arXiv:2409.02172
- Koudmani, S., Sijacki, D., & Smith, M. C. 2022, *MNRAS*, 516, 2112
- Koutsouridou, I., Salvadori, S., & Skúladóttir, Á. 2023, arXiv e-prints, arXiv:2312.05309
- Kroupa, P. 2001, *MNRAS*, 322, 231
- Kroupa, P., Gjergo, E., Jerabkova, T., & Yan, Z. 2024, arXiv e-prints, arXiv:2410.07311
- Kroupa, P. & Jerabkova, T. 2021, arXiv e-prints, arXiv:2112.10788
- Labbé, I., van Dokkum, P., Nelson, E., et al. 2023, *Nature*, 616, 266
- Lancaster, L., Ostriker, E. C., Kim, J.-G., & Kim, C.-G. 2021, *ApJ*, 914, 90
- Langeroodi, D. & Hjorth, J. 2023, arXiv e-prints, arXiv:2307.06336
- Langeroodi, D., Hjorth, J., Chen, W., et al. 2023, *ApJ*, 957, 39
- Larkin, M. M., Gerasimov, R., & Burgasser, A. J. 2023, *AJ*, 165, 2
- Larson, R. B. 1998, *MNRAS*, 301, 569
- Lazar, A. & Bromm, V. 2022, *MNRAS*, 511, 2505
- Lecroq, M., Charlot, S., Bressan, A., et al. 2024, *MNRAS*, 527, 9480
- Lee, J. H., Park, C., Hwang, H. S., & Kwon, M. 2024, *ApJ*, 966, 113
- Li, Z., Kakiichi, K., Christensen, L., et al. 2025, arXiv e-prints, arXiv:2504.18616
- Limongi, M. & Chieffi, A. 2003, *ApJ*, 592, 404
- Liu, B. & Bromm, V. 2020, *MNRAS*, 497, 2839
- Liu, B. & Bromm, V. 2022, *ApJ*, 937, L30
- Liu, B., Gurian, J., Inayoshi, K., et al. 2024a, *MNRAS*, 534, 290
- Liu, B., Hartwig, T., Sartorio, N. S., et al. 2024b, *MNRAS*, 534, 1634
- Liu, B., Kessler, D., Gessey-Jones, T., et al. 2025a, arXiv e-prints, arXiv:2504.00535
- Liu, B., Sibony, Y., Meynet, G., & Bromm, V. 2021, *MNRAS*, 506, 5247
- Liu, B., Sibony, Y., Meynet, G., & Bromm, V. 2025b, *ApJ*, 980, L30
- Ma, J.-Z., Farmer, R., de Mink, S. E., & Laplace, E. 2025, arXiv e-prints, arXiv:2505.02918
- Madau, P. & Dickinson, M. 2014, *ARA&A*, 52, 415
- Madau, P., Giallongo, E., Grazian, A., & Haardt, F. 2024, *ApJ*, 971, 75
- Magg, M., Hartwig, T., Chen, L.-H., & Tarumi, Y. 2022a, *The Journal of Open Source Software*, 7, 4417
- Magg, M., Hartwig, T., Glover, S. C. O., Klessen, R. S., & Whalen, D. J. 2016, *MNRAS*, 462, 3591
- Magg, M., Schauer, A. T. P., Klessen, R. S., et al. 2022b, *ApJ*, 929, 119
- Maoz, D., Mannucci, F., & Brandt, T. D. 2012, *MNRAS*, 426, 3282
- Mapelli, M. 2021, in *Handbook of Gravitational Wave Astronomy*, ed. C. Bambi, S. Katsanevas, & K. D. Kokkotas, 16
- Mapelli, M., Spera, M., Montanari, E., et al. 2020, *ApJ*, 888, 76
- Marchant, P. & Bodensteiner, J. 2024, *ARA&A*, 62, 21
- Marchant, P. & Moriya, T. J. 2020, *A&A*, 640, L18
- Marks, M., Kroupa, P., Dabringhausen, J., & Pawłowski, M. S. 2012, *MNRAS*, 422, 2246
- Martinet, S., Meynet, G., Ekström, S., Georgy, C., & Hirschi, R. 2023, *A&A*, 679, A137
- Mathew, S. S. & Federrath, C. 2021, *MNRAS*, 507, 2448
- Mathew, S. S., Federrath, C., & Seta, A. 2023, *MNRAS*, 518, 5190
- Mathew, S. S., Federrath, C., & Seta, A. 2025, *MNRAS*, 536, 1932
- McClymont, W., Tacchella, S., Smith, A., et al. 2025, arXiv e-prints, arXiv:2503.04894
- McLeod, D. J., McLure, R. J., & Dunlop, J. S. 2016, *MNRAS*, 459, 3812
- Menon, S. H., Lancaster, L., Burkhart, B., et al. 2024, *ApJ*, 967, L28
- Mingozi, M., James, B. L., Arellano-Córdova, K. Z., et al. 2022, *ApJ*, 939, 110
- Moe, M. & Di Stefano, R. 2017, *ApJS*, 230, 15
- Mowla, L., Iyer, K., Asada, Y., et al. 2024, *Nature*, 636, 332
- Mowla, L., van der Wel, A., van Dokkum, P., & Miller, T. B. 2019, *ApJ*, 872, L13
- Muñoz, J. B., Mirocha, J., Chisholm, J., Furlanetto, S. R., & Mason, C. 2024, *MNRAS*, 535, L37
- Nagele, C. & Umeda, H. 2023, *ApJ*, 949, L16
- Naidu, R. P., Oesch, P. A., Brammer, G., et al. 2025, arXiv e-prints, arXiv:2505.11263
- Nakajima, K., Ouchi, M., Isobe, Y., et al. 2023, *ApJS*, 269, 33
- Nakane, M., Ouchi, M., Nakajima, K., et al. 2025, arXiv e-prints, arXiv:2503.11457
- Nandal, D., Farrell, E., Buldgen, G., Meynet, G., & Ekström, S. 2024a, *A&A*, 685, A159
- Nandal, D., Regan, J. A., Woods, T. E., et al. 2024b, *A&A*, 683, A156
- Nandal, D., Whalen, D. J., Latif, M. A., & Heger, A. 2025, arXiv e-prints, arXiv:2502.04435
- Nguyen, C. T., Costa, G., Girardi, L., et al. 2022, *A&A*, 665, A126
- Nishigaki, M., Behroozi, P., Ouchi, M., et al. 2025, arXiv e-prints, arXiv:2503.10999
- Nomoto, K., Iwamoto, K., Nakasato, N., et al. 1997, *Nucl. Phys. A*, 621, 467
- Nomoto, K., Kobayashi, C., & Tominaga, N. 2013, *ARA&A*, 51, 457
- Oesch, P. A., Bouwens, R. J., Illingworth, G. D., Labbé, I., & Stefanon, M. 2018, *ApJ*, 855, 105
- Pantoni, L., Lapi, A., Massardi, M., Goswami, S., & Danese, L. 2019, *ApJ*, 880, 129
- Pepe, E., Palla, M., Matteucci, F., & Spitoni, E. 2025, *A&A*, 694, A19
- Pérez-González, P. G., Costantin, L., Langeroodi, D., et al. 2023, *ApJ*, 951, L1
- Pérez-González, P. G., Östlin, G., Costantin, L., et al. 2025, arXiv e-prints, arXiv:2503.15594
- Planck Collaboration, Ade, P. A. R., Aghanim, N., et al. 2016, *A&A*, 594, A13
- Polak, B., Mac Low, M.-M., Klessen, R. S., et al. 2024, *A&A*, 690, A94
- Rawat, V., Samal, M. R., Zavagno, A., et al. 2025, arXiv e-prints, arXiv:2505.10173
- Rémy-Ruyer, A., Madden, S. C., Galliano, F., et al. 2014, *A&A*, 563, A31
- Riaz, S., Hartwig, T., & Latif, M. A. 2022, *ApJ*, 937, L6
- Rinaldi, P., Caputi, K. I., van Mierlo, S. E., et al. 2022, *ApJ*, 930, 128
- Rinaldi, P., Navarro-Carrera, R., Caputi, K. I., et al. 2025, *ApJ*, 981, 161
- Ritter, J. S., Safranek-Shrader, C., Milosavljević, M., & Bromm, V. 2016, *MNRAS*, 463, 3354
- Ritter, J. S., Sluder, A., Safranek-Shrader, C., Milosavljević, M., & Bromm, V. 2015, *MNRAS*, 451, 1190
- Rizzuti, F., Matteucci, F., Molaro, P., Cescutti, G., & Maiolino, R. 2024, arXiv e-prints, arXiv:2412.05363
- Roberti, L., Limongi, M., & Chieffi, A. 2024, *ApJS*, 270, 28
- Rohr, E., Feldmann, R., Bullock, J. S., et al. 2022, *MNRAS*, 510, 3967
- Rossi, M., Romano, D., Mucciarelli, A., et al. 2024a, *A&A*, 691, A284
- Rossi, M., Salvadori, S., & Skúladóttir, Á. 2021, *MNRAS*, 503, 6026
- Rossi, M., Salvadori, S., Skúladóttir, Á., & Vanni, I. 2023, *MNRAS*, 522, L1
- Rossi, M., Salvadori, S., Skúladóttir, Á., Vanni, I., & Koutsouridou, I. 2024b, arXiv e-prints, arXiv:2406.12960
- Rowland, L. E., Stefanon, M., Bouwens, R., et al. 2025, arXiv e-prints, arXiv:2501.10559
- Rusakov, V., Steinhardt, C. L., & Sneppen, A. 2023, *ApJS*, 268, 10
- Sabbahit, G. N., Vink, J. S., Sander, A. A. C., & Higgins, E. R. 2023, *MNRAS*, 524, 1529
- Saldana-Lopez, A., Chisholm, J., Gazagnes, S., et al. 2025, arXiv e-prints, arXiv:2501.17145
- Salmon, B., Papovich, C., Finkelstein, S. L., et al. 2015, *ApJ*, 799, 183
- Salpeter, E. E. 1955, *ApJ*, 121, 161
- Salvadori, S., Schneider, R., & Ferrara, A. 2007, *MNRAS*, 381, 647
- Sana, H., de Mink, S. E., de Koter, A., et al. 2012, *Science*, 337, 444
- Sana, H., Le Bouquin, J. B., Lacour, S., et al. 2014, *ApJS*, 215, 15
- Sarkar, A., Chakraborty, P., Vogelsberger, M., et al. 2025, *ApJ*, 978, 136
- Schaerer, D. 2002, *A&A*, 382, 28
- Schaerer, D., Guibert, J., Marques-Chaves, R., & Martins, F. 2025, *A&A*, 693, A271
- Schauer, A. T. P., Liu, B., & Bromm, V. 2019, *ApJ*, 877, L5
- Schneider, F. R. N., Lau, M. Y. M., & Roepke, F. K. 2025, arXiv e-prints, arXiv:2502.00111
- Schneider, R., Omukai, K., Bianchi, S., & Valiante, R. 2012, *MNRAS*, 419, 1566
- Schulze, S., Fransson, C., Kozyreva, A., et al. 2024, *A&A*, 683, A223
- Sgalletta, C., Mapelli, M., Boco, L., et al. 2024, arXiv e-prints, arXiv:2410.21401
- Sharma, R. S., Brooks, A. M., Tremmel, M., Bellovary, J., & Quinn, T. R. 2023, *ApJ*, 957, 16
- Shen, X., Vogelsberger, M., Boylan-Kolchin, M., Tacchella, S., & Kannan, R. 2023, *MNRAS*, 525, 3254
- Shen, X., Vogelsberger, M., Boylan-Kolchin, M., Tacchella, S., & Naidu, R. P. 2024, *MNRAS*, 533, 3923
- Shepherd, K. G., Costa, G., Ugolini, C., et al. 2025, arXiv e-prints, arXiv:2505.10206
- Simmonds, C., Tacchella, S., Hainline, K., et al. 2024, *MNRAS*, 535, 2998
- Simonato, F., Torniamenti, S., Mapelli, M., et al. 2025, arXiv e-prints, arXiv:2505.07959
- Sims, P. H., Bevens, H. T. J., Fialkov, A., et al. 2025, arXiv e-prints, arXiv:2504.09725
- Somerville, R. S., Behroozi, P., Pandya, V., et al. 2018, *MNRAS*, 473, 2714
- Somerville, R. S., Yung, L. Y. A., Lancaster, L., et al. 2025, arXiv e-prints, arXiv:2505.05442
- Spera, M., Mapelli, M., Giacobbo, N., et al. 2019, *MNRAS*, 485, 889

- Stahler, S. W. & Palla, F. 2008, *The formation of stars* (New York: John Wiley & Sons)
- Stefanon, M., Bouwens, R. J., Labbé, I., et al. 2021, *ApJ*, 922, 29
- Sun, W., Ho, L. C., Zhuang, M.-Y., et al. 2024, *ApJ*, 960, 104
- Tacchella, S., Bose, S., Conroy, C., Eisenstein, D. J., & Johnson, B. D. 2018, *ApJ*, 868, 92
- Tanikawa, A., Kinugawa, T., Yoshida, T., Hijikawa, K., & Umeda, H. 2021, *MNRAS*, 505, 2170
- Tanikawa, A., Moriya, T. J., Tominaga, N., & Yoshida, N. 2023, *MNRAS*, 519, L32
- Tanvir, T. S. & Krumholz, M. R. 2024, *MNRAS*, 527, 7306
- Tarumi, Y., Hartwig, T., & Magg, M. 2020, *ApJ*, 897, 58
- Tauris, T. M. & van den Heuvel, E. P. J. 2023, *Physics of Binary Star Evolution. From Stars to X-ray Binaries and Gravitational Wave Sources*
- Tohill, C., Bamford, S. P., Conselice, C. J., et al. 2024, *ApJ*, 962, 164
- Trinca, A., Schneider, R., Valiante, R., et al. 2024, *MNRAS*, 529, 3563
- Tsiatsiou, S., Sibony, Y., Nandal, D., et al. 2024, *A&A*, 687, A307
- Vanni, I., Salvadori, S., Skúladóttir, Á., Rossi, M., & Koutsouridou, I. 2023, *MNRAS*, 526, 2620
- Venditti, A., Bromm, V., Finkelstein, S. L., Graziani, L., & Schneider, R. 2024, *MNRAS*, 527, 5102
- Ventura, E. M., Qin, Y., Balu, S., & Wyithe, J. S. B. 2024, *MNRAS*, 529, 628
- Vink, J. S. 2023, *A&A*, 679, L9
- Vogelsberger, M., Genel, S., Sijacki, D., et al. 2013, *MNRAS*, 436, 3031
- Wang, B., Leja, J., Atek, H., et al. 2025a, *arXiv e-prints*, arXiv:2504.15255
- Wang, F. Y., Bromm, V., Greif, T. H., et al. 2012, *ApJ*, 760, 27
- Wang, W., Cantalupo, S., Pensabene, A., et al. 2025b, *Nature Astronomy* [arXiv:2409.17956]
- Watanabe, K., Ouchi, M., Nakajima, K., et al. 2024, *ApJ*, 962, 50
- West, C., Heger, A., Cote, B., Serxner, L., & Sun, H. 2024, *arXiv e-prints*, arXiv:2410.16594
- Wiggins, A. I., Bovill, M. S., Strolger, L.-G., Stiavelli, M., & Bowling, C. 2024, *arXiv e-prints*, arXiv:2402.17076
- Xin, W., Yip, C.-M., Nomoto, K., Zhang, X., & Bi, S. 2025, *arXiv e-prints*, arXiv:2504.13766
- Xu, H., Wise, J. H., Norman, M. L., Ahn, K., & O'Shea, B. W. 2016, *ApJ*, 833, 84
- Xu, X., Heckman, T., Henry, A., et al. 2022, *ApJ*, 933, 222
- Xu, X., Henry, A., Heckman, T., et al. 2025a, *ApJ*, 984, 94
- Xu, Y., Ouchi, M., Nakajima, K., et al. 2025b, *ApJ*, 984, 182
- Yan, Z., Jerabkova, T., & Kroupa, P. 2023, *A&A*, 670, A151
- Yang, L., Kartaltepe, J. S., Franco, M., et al. 2025, *arXiv e-prints*, arXiv:2504.07185
- Yates, R. M., Hendriks, D., Vijayan, A. P., et al. 2024, *MNRAS*, 527, 6292
- Yung, L. Y. A., Somerville, R. S., & Iyer, K. G. 2025, *arXiv e-prints*, arXiv:2504.18618
- Zaritsky, D. & Behroozi, P. 2023, *MNRAS*, 519, 871

## Appendix A: Star formation main sequence

As explained in Sec. 2.2, the star formation prescription in `ASLOTH` is updated with reduced galaxy sizes to better reproduce the scatter around the star formation main sequence (SFMS) in observations. In this section, we compare the results of our new model and those of the original/old model of Hartwig et al. (2022) in the context of observational data at  $z \sim 4 - 10$  (Salmon et al. 2015; Rinaldi et al. 2022, 2025; Heintz et al. 2023; Nakajima et al. 2023; Clarke et al. 2024; Curti et al. 2024; Sarkar et al. 2025). In fact, the observational results for high- $z$  SFMS show significant differences in both normalization and slope, which imply that the SFMS is highly sensitive to selection effects and uncertainties in SFR and stellar mass measurements. Therefore, we do not include SFMS in our likelihood analysis.

For the old model with  $R_\star = R_{\text{vir}}/c_{\text{DM}}$ , we run a simulation with  $\alpha_{\text{out}} = 1$ ,  $M_{\text{out}0} = 10^9 M_\odot$ , and  $m_{\text{max}} = 250 M_\odot$  chosen to reproduce the observed SFRD at  $z \lesssim 7$  with optimal IMF-averaged metal yield, as shown in Fig. A.1. The resulting relation between SFR and stellar mass is shown in Fig. A.2 for two redshift bins:  $z \sim 4 - 6$  (top) and  $z \sim 6 - 8$  (bottom). The simulated SFMS is defined as a linear fit in the  $\log \text{SFR} - \log M_\star$  space for simulated galaxies with  $\text{SFR} > 10^{-0.5} M_\odot \text{ yr}^{-1}$ . Interestingly, for both redshift bins, the simulated SFMS agrees with the main sequence (MS) fit of Rinaldi et al. (2022), which is however below the fits from Salmon et al. (2015) and Heintz et al. (2023) by  $\sim 0.6$  dex. The latter two are consistent with the SFMS found in the JWST galaxies at  $z \sim 4 - 10$  (Nakajima et al. 2023; Curti et al. 2024; Sarkar et al. 2025). The SFMS from Clarke et al. (2024) appears to be an in-between case. The scatter around the SFMS is  $\sigma \sim 0.16 - 0.19$  dex in the simulation, which is significantly lower than that  $\sigma \sim 0.5$  dex for the JWST galaxies. A similar intrinsic scatter of  $\sigma \sim 0.42 - 0.49$  dex is also found by Clarke et al. (2024) from observations at  $z \sim 4 - 7$ . Clearly, the stochasticity of star formation (at the timescale of 10 Myr) is significantly underestimated by the old model of Hartwig et al. (2022). Besides, there are no galaxies from the simulation that is close to the starburst track with  $\text{SFR}/M_\star \sim 10^{-7} \text{ yr}^{-1}$  found by Rinaldi et al. (2022), while many JWST galaxies appear to be in the starburst phase.

In Fig. A.3, we show the SFMS at  $z \sim 4 - 6$  (left) and  $z \sim 6 - 8$  (right) from simulations using the new star formation prescription with smaller galaxy sizes  $R_\star = 2.5R_{50}$  (Eq. 4) for the best-fit models (see Fig. 4) chosen for  $\alpha_{\text{out}} = 1.0$  (top), 0.5 (middle), and 0 (bottom). Similar to the case of the old prescription, the simulated SFMS is generally in agreement with that from Rinaldi et al. (2022) except for the  $\alpha_{\text{out}} = 0$  case at  $z \sim 4 - 6$ , where the simulated SFMS has a smaller slope. So, the median SFR of the simulated galaxies is generally lower than that of the JWST galaxies by  $\sim 0.6$  dex, which is a persistent feature of our small simulation volume with poor statistics of luminous objects. In the  $\alpha_{\text{out}} = 0$  case, star formation in galaxies with  $M_\star \gtrsim 10^{9.2} M_\odot$  is significantly quenched by outflows, while the quenching is less rapid in the other two cases with weaker outflows. This is consistent with the finding in Sec. 5.2 that the SFRD at  $z \sim 5$  is underestimated by a factor of  $\sim 2$  in the  $\alpha_{\text{out}} = 0$  best-fit model. With the new star formation prescription, the scatter around SFMS increases by a factor of  $\sim 2$  to  $\sigma \sim 0.29 - 0.33$  dex, comparable but still slightly smaller than that in observations  $\sigma \sim 0.4 - 0.5$  dex (Clarke et al. 2024; Sarkar et al. 2025, Tacchella et al. in prep.). Starburst galaxies with  $\text{SFR}/M_\star \gtrsim 10^{-7} \text{ yr}^{-1}$  also show up in these simulations, alongside with galaxies on quenching tracks with dropping SFR and increasing  $Z$ . Note that a similar trend of

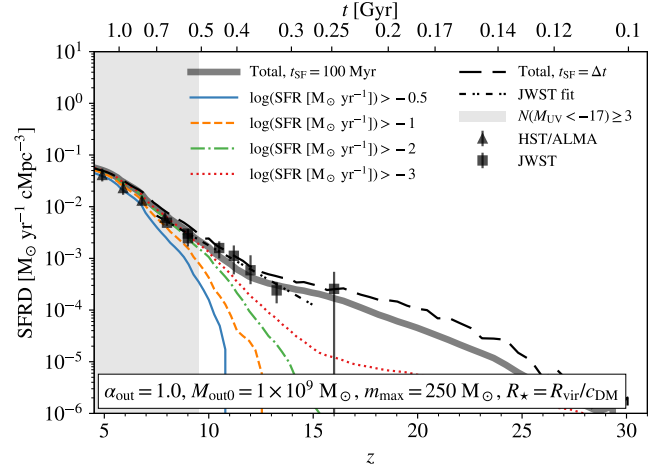


**Fig. A.1.** SFRD from an exemplar run using the old star formation prescription of Hartwig et al. (2022) with  $R_\star = R_{\text{vir}}/c_{\text{DM}}$  for  $\alpha_{\text{out}} = 1$ ,  $M_{\text{out}0} = 10^9 M_\odot$ , and  $m_{\text{max}} = 250 M_\odot$ . The thick solid curve shows the total SFRD measured on a timescale of  $t_{\text{SF}} = 100$  Myr, while the solid, dashed, dash-dotted, and dotted curves show the contributions from galaxies with  $\log(\text{SFR} [M_\odot \text{ yr}^{-1}]) > -0.5, -1, -2$ , and  $-3$ , respectively. The curve for  $\log(\text{SFR} [M_\odot \text{ yr}^{-1}]) > -0.5$  should be compared with the observational results from HST/ALMA and JWST (for luminous galaxies with  $M_{\text{UV}} < -17$ ) embodied by the triangles and squares, respectively (see Table 2). The JWST results satisfy a linear relation between  $\log \text{SFR}$  and  $z$  (Eq. 13) at  $z \sim 7.5 - 15$  (dot-dash-dotted). The long dashed curve shows the total SFRD measured in simulation timesteps. The shaded region denotes the regime where at least 3 galaxies in the simulation box are above the JWST detection limit ( $M_{\text{UV}} < -17$ ).

increasing SFR dispersion with decreasing  $R_\star$  is found in local observations as well (e.g., He et al. 2025).

In conclusion, the enhanced galaxy compactness in the new star formation prescription is necessary to better capture the bursty nature of star formation seen in observations of high- $z$  (dwarf) galaxies. Moreover, such compactness and the resulting bursty star formation also boost metal enrichment, which is needed to reproduce the observed MZSFR (Sec. 4.2). Under the old scheme with larger  $R_\star$ , the simulated galaxies are always too metal-poor, unless the outflow efficiency is significantly reduced ( $M_{\text{out}0} < 10^9 M_\odot$ ), which then overpredicts the SFRD and CSMD. This trend is consistent with the negative correlation between (the offsets of) galaxy size (from the GMSR) and metallicity (from the MZSFR) found in observations (e.g., Langeroodi & Hjorth 2023; Jia et al. 2025).

## Appendix B: CSFH in the best-fit models for

### $\alpha_{\text{out}} = 0.5$ and 1

In Fig. B.1, we show the CSFH in the best-fit models for  $\alpha_{\text{out}} = 1.0$  (top) and 0.5 (bottom) in terms of SFRD (left) and CSMD (right). Here, the agreement between simulation results and observational data (detailed in Sec. 4.1) is worse than the case of the best-fit model for  $\alpha_{\text{out}} = 0$  (Fig. 8). It turns out that star formation in detectable galaxies with  $\text{SFR} > 10^{-0.5} M_\odot \text{ yr}^{-1}$  ( $M_{\text{UV}} \lesssim -17$ ) in these models is generally faster (slower) than that inferred from observations at  $z \lesssim 8$  ( $\gtrsim 10$ ). A similar trend can be seen in the CSMD of galaxies with  $M_\star > 10^8 M_\odot$ . The reason is that for  $\alpha_{\text{out}} > 0$ , the outflow efficiency is suppressed in massive halos with  $M_h \gtrsim M_{\text{out}0}$  by Eq. 6, leading to a rapid rise of SFRD towards lower redshift where such halos become more

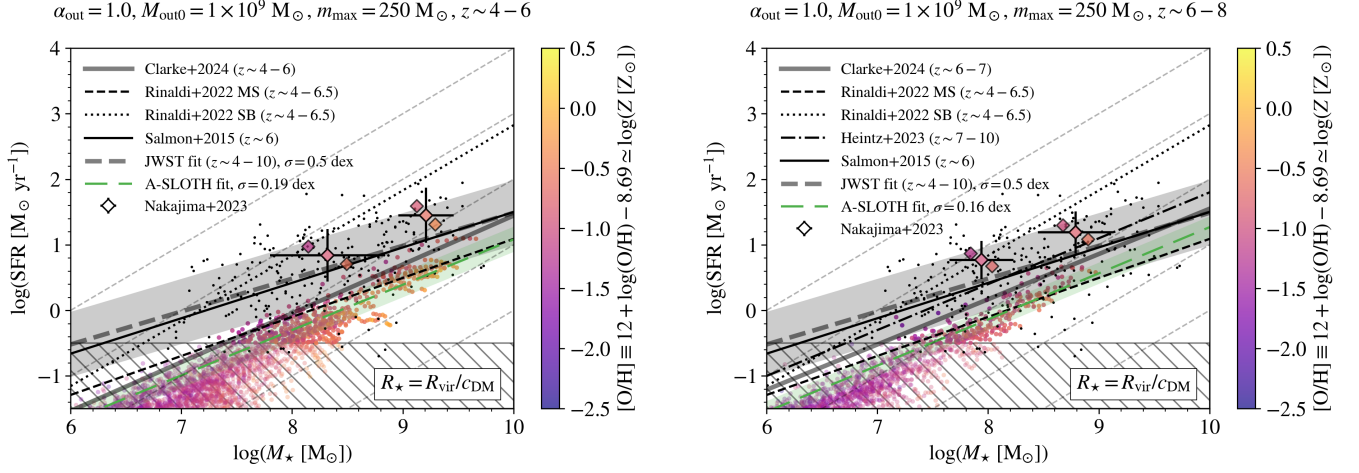


**Fig. A.2.** SFMS at  $z \sim 4-6$  (left) and  $z \sim 6-8$  (right) from an exemplar run using the old star formation prescription of Hartwig et al. (2022) with  $R_* = R_{\text{vir}}/c_{\text{DM}}$  for  $\alpha_{\text{out}} = 1$ ,  $M_{\text{out}0} = 10^9 M_{\odot}$ , and  $m_{\text{max}} = 250 M_{\odot}$ . Individual simulated galaxies are shown as dots color-coded by metallicity, while the JWST galaxies compiled by Sarkar et al. (2025, see their fig. 3) including those from Nakajima et al. (2023) and Curti et al. (2024) are shown as the smaller black dots. We fit a linear relation (in log-log space) to the simulated galaxies with  $\log(\text{SFR} [M_{\odot} \text{ yr}^{-1}]) > -0.5$  outside the hatched region as the long dashed line. The relevant scatter is shown by the green shaded region. Similarly, the thick dashed line and gray shaded region show the fit and scatter for the JWST galaxies. We also show the average values of SFR,  $M_*$ , and metallicity of the JWST galaxies of Nakajima et al. (2023, see their table 2) with the diamonds. Each data point involves three diamonds color-coded by the mean and  $1\sigma$  upper and lower limits of metallicity. The relevant spreads in SFR and  $M_*$  are shown by errorbars. The thick solid, dashed, solid, and dash-dotted lines show the observed SFMS from Clarke et al. (2024), Rinaldi et al. (2022), Salmon et al. (2015), and Heintz et al. (2023). The dotted line shows the fit for starburst (SB) galaxies from Rinaldi et al. (2022). The thin dashed lines mark 5 specific SFR values in the range  $\text{SFR}/M_* \in [10^{-10}, 10^{-6}] \text{ yr}^{-1}$  with 1 dex spacing.

important. On the other hand, the outflow efficiency is enhanced in smaller halos. Therefore, when  $\alpha_{\text{out}}$  increases, the contribution of faint galaxies with  $\text{SFR} \lesssim 10^{-0.5} M_{\odot} \text{ yr}^{-1}$  to the total SFRD is smaller, which becomes sub-dominant ( $\lesssim 50\%$ ) and negligible at  $z \lesssim 8$  for  $\alpha_{\text{out}} = 0.5$  and 1. In contrast, faint galaxies still account for  $\sim 30-50\%$  of the total SFRD at  $z \sim 5-7$  in the best-fit model for  $\alpha_{\text{out}} = 0$  (Fig. 8). Interestingly, in the  $\alpha_{\text{out}} = 0.5$  best-fit model, the simulated SFRD at  $z \sim 5$  matches very well with the observed value, while it is underestimated by a factor of  $\sim 2$  in the  $\alpha_{\text{out}} = 0$  best-fit model that shows good agreement with observations at higher  $z$  up to  $z \sim 13$ . This hints for non-negligible evolution of outflow parameters with redshift at  $z \lesssim 6$ .

### Appendix C: Type Ia supernovae

We implement a phenomenological model for Type Ia SNe based on the method of Deng et al. (2024). This model is described by four parameters: the number of Type Ia SNe per unit stellar mass formed  $N_{\text{Ia}}$ , the upper bound  $t_{\text{Ia,up}}$ , lower bound  $t_{\text{Ia,low}}$ , and slope  $\alpha_{\text{DTD}}$  of the delay time distribution (DTD):  $p_{\text{DTD}}(t) \propto t^{-\alpha_{\text{DTD}}}$ ,  $\int_{t_{\text{Ia,low}}}^{t_{\text{Ia,up}}} p_{\text{DTD}}(t) dt = 1$ . Here, we adopt  $N_{\text{Ia}} = 1.3 \times 10^{-3} M_{\odot}^{-1}$ ,  $t_{\text{Ia,up}} = 14 \text{ Gyr}$ ,  $t_{\text{Ia,low}} = 40 \text{ Myr}$  (corresponding to the lifetime of a  $8 M_{\odot}$  star), and  $\alpha_{\text{DTD}} = 1.12$  following Maoz et al. (2012); Vogelsberger et al. (2013). With these choices of parameters, the solar abundance of Fe can be reproduced in MW-like galaxies at  $z \sim 0$ .

To reduce computational cost and memory usage, a hybrid approach is adopted to keep track of (1) individual progenitors of Type Ia SNe and (2) progenitor populations. At each star formation timestep  $i$ , we first estimate the number of SN Ia progenitors expected to form as  $N_{\text{Ia,P,est}}^i = N_{\text{Ia}} \delta M_*$  given the mass  $\delta M_*$  of stars formed in this step. If (1)  $N_{\text{Ia,P,est}}^i \leq 10$ , we sample

the number  $N_{\text{Ia,P}}$  of SN Ia progenitors formed in this step from a Poisson distribution ( $p_{N_{\text{Ia,P}}} = \lambda^{N_{\text{Ia,P}}} e^{-\lambda} / N_{\text{Ia,P}}!$ ) with parameter  $\lambda = N_{\text{Ia,P,est}}^i$ . Then, each progenitor is assigned a delay time  $t_{\text{Ia}}$  randomly drawn from the DTD. The clock of each progenitor is checked by A-SLOTH in each adaptive sub-timestep, and the SN Ia event is triggered when  $t_{\text{Ia}}$  has past since its formation.

If (2)  $N_{\text{Ia,P,est}}^i > 10$ , we instead create a population of SN Ia progenitors. Thereafter, at each star formation timestep  $l$  with  $t_{l+1} > t_{\text{Ia,low}}$ , we estimate the number of Type Ia SNe expected to go off from this population as  $N_{\text{Ia,est}}^i = N_{\text{Ia,P,est}}^i \int_{\max(t_{\text{Ia,low}}, t_l - t_i)}^{t_{l+1} - t_i} p_{\text{DTD}}(t) dt$ . The actually number of SN Ia events is again drawn from a Poisson distribution with  $\lambda = N_{\text{Ia,est}}^i$ . Such sampling of SN Ia events continues until the total number of Type Ia SNe sampled exceeds  $N_{\text{Ia,P,est}}^i$ .

The first method for  $N_{\text{Ia,P,est}}^i \leq 10$  ensures that we do not create too many SN Ia progenitor populations for galaxies with low SFR, while the second method for  $N_{\text{Ia,P,est}}^i > 10$  ensures that we do not track too many individual SN Ia progenitors in A-SLOTH. Each SN Ia event adds  $e_{\text{SN}} = 10^{51} \text{ erg}$  to the energy budget of SNe  $E_{\text{SN}}^i$ . Following Deng et al. (2024), the ‘W7’ model from Nomoto et al. (1997) is adopted for the SN Ia metal yields.



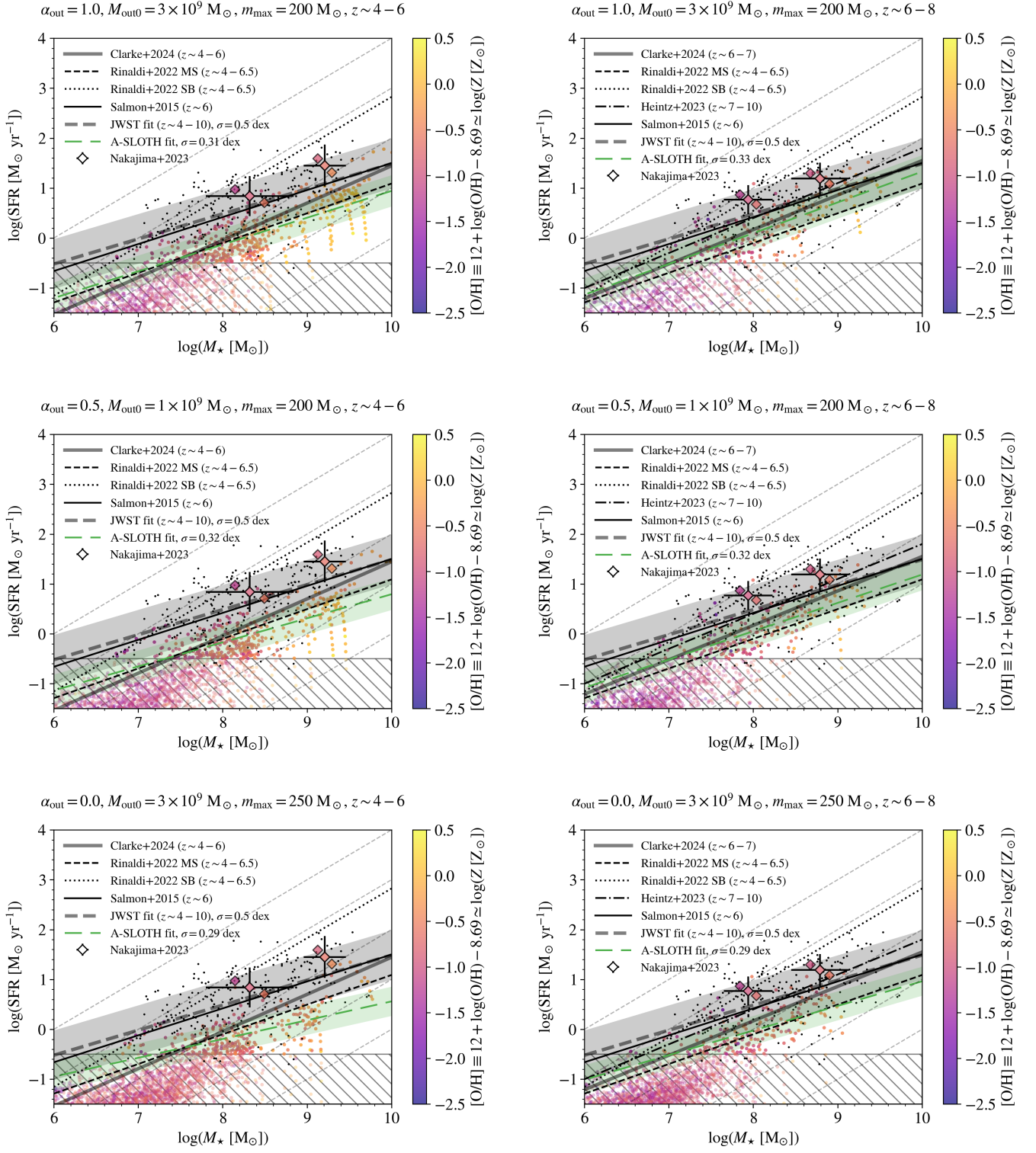


**Fig. A.3.** Same as Fig. A.2 but for the SFMS from simulations using the new star formation prescription. As representative examples, we consider the three best-fit models (see Sec. 5.2) chosen for  $\alpha_{\text{out}} = 1.0$  (top), 0.5 (middle), and 0 (bottom) at  $z \sim 4-6$  (left) and  $z \sim 6-8$  (right).

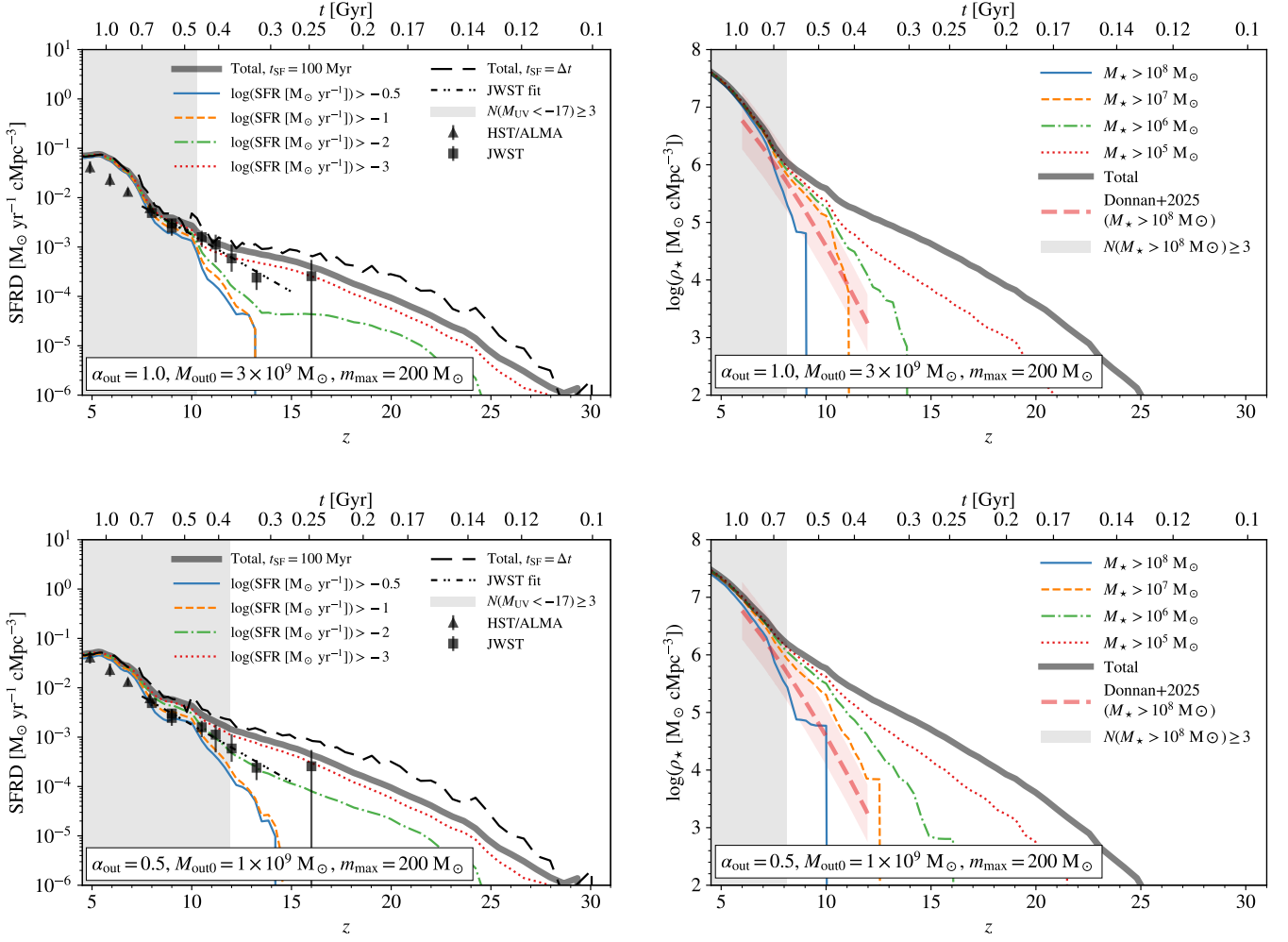


**Fig. B.1.** Same as Fig. 8 but for the best-fit models for  $\alpha_{\text{out}} = 1.0$  (top) and  $0.5$  (bottom).